

# **Methodology for Positron Emission Tomography Imaging of Amyloid- $\beta$ Plaques: Cross-Sectional and Longitudinal Validation**

Submitted in partial fulfillment of the requirements for

the degree of

Doctor of Philosophy

in

Biomedical Engineering

Davneet S Minhas

B.S., Biomedical Engineering, Johns Hopkins University

Carnegie Mellon University  
Pittsburgh, PA

# Acknowledgements

First and foremost I would like to thank my thesis mentor, Professor Julie Price. Her kindness, enthusiasm, encouragement, and support through times of progress and stagnancy made this possible. She has been a great teacher and model as a researcher.

I would like to thank my thesis committee, Professors George Stetten, John Galeotti, and Chien Ho for their guidance and support. I am grateful to have had their enthusiasm and input guide my efforts. I also want to especially thank Professor Yu-li Wang for his support. Without his generosity this would not have been possible.

I am indebted to the University of Pittsburgh PET Center staff for their friendship and support over the years. Rhaven Coleman, Carl Becker, Jeffrey James, and Cristy Matan were always willing to help in any way possible.

I want to thank Professor Charles Laymon for his ideas and discussions, which helped shape this work. I am grateful to Professors Chet Mathis, William Klunk, Milos Ikonomic, and Brian Lopresti for their invaluable guidance and support during key milestones. I want to also thank Professors William Klunk and Milos Ikonomic for providing access to much of the data used throughout this work.

Lastly, I am most grateful to Beautia Dew for her constant presence and support. I cannot thank her enough.

Financial support for this work was provided by the NIH (R01AG018402, R01AG020226, P01AG025204, R01AG033042, P50AG005133, R37AG025516, K02AG027998, R01MH070729), Dana Foundation, Alzheimer's Association (TLL-01-3381), US Department of Energy (DE-FD02-03 ER63590), and GE Healthcare.

# Abstract

The aim of this work was to identify optimal methodological techniques for quantifying  $^{11}\text{C}$ -Pittsburgh Compound B (PiB) PET imaging measures of Amyloid- $\beta$  protein deposition, a neuropathological hallmark of Alzheimer's disease (AD), in both cross-sectional and longitudinal studies. Simulated phantoms based on existing MR and PiB PET images were generated to characterize and validate the implementation of three partial volume correction (PVC) techniques that account for the limited spatial resolution of PET: the Meltzer, the Müller-Gärtner, and the Region-Based Voxel-Wise methods. The impact of these partial volume correction methods on correlations between region-matched antemortem PiB PET standardized uptake value ratios (SUVR) and postmortem measures of amyloid load was then examined in a unique cohort of 12 subjects. Results indicate that the impact of PVC is not only dependent on the technique utilized, but also highly specific to region placement and subject anatomy. While the Region-Based Voxel-Wise method outperformed other PVC methods, no PVC method improved correlations between antemortem PiB PET SUVR and postmortem measures of amyloid load, likely due to the noise propagation properties of the techniques.

Several PET image analysis methods were also evaluated to assess relative performance in measuring change of amyloid deposition over time: the Simplified Reference Tissue, the Logan graphical, and the SUVR methods. This evaluation was performed in a unique cohort of 48 healthy elderly control, mild cognitive impairment, and AD subjects imaged with PiB PET at baseline and follow-up. The potential impact of non-specific reference region selection, changes in relative PiB delivery between target and reference tissues, and the partial volume effect were examined. The SUVR measure over 40-60 minutes post-injection was found to be optimal in tracking longitudinal changes across diagnostic groups. Results also indicate that the partial volume effects from non-specific binding in white matter can influence measured changes of amyloid load.

In conclusion, PVC techniques did not significantly improve correlations between PiB PET and postmortem measures of amyloid load. However, the Region-Based Voxel-Wise PVC method should be considered for use in longitudinal PiB PET studies.

# Table of Contents

<b>Acknowledgements</b>	ii
<b>Abstract</b>	iii
<b>List of Tables</b>	vii
<b>List of Figures</b>	viii
<b>List of Abbreviations</b>	xv
<b>Chapter 1 Background and Overview</b>	<b>1</b>
1.1 Background	1
1.1.1 Position Emission Tomography Imaging	1
1.1.2 The Partial Volume Effect	4
1.1.3 Partial Volume Correction Approaches	7
1.1.3.1 Meltzer Method	7
1.1.3.2 Müller-Gärtner Method	8
1.1.3.3 Geometric Transform Matrix Method	8
1.1.3.4 Modified-Müller-Gärtner Method	10
1.1.3.5 The Region-Based Voxel-Wise Method	10
1.1.4 PET Quantification Methods: Radioligand-Protein Binding	11
1.1.4.1 Pharmacokinetic Nomenclature	11
1.1.4.2 Compartmental Modeling	14
1.1.4.3 Simplified Reference Tissue Model	19
1.1.4.4 Logan Graphical Analysis	22
1.1.4.5 Standardized Uptake Value Ratio	24
1.1.5 Neurological Characteristics of Alzheimer's Disease	26
1.1.6 Amyloid Beta Plaque Imaging	27
1.2 Overview of Dissertation Work	31
<b>Chapter 2 Implementation and Characterization of PVC</b>	<b>34</b>
<b>Techniques</b>	
2.1 Existing Software Used in This Work	34
2.1.1 FreeSurfer	34
2.1.2 The FMRIB Software Library	37



2.1.3	Statistical Parametric Mapping	37
2.2	Implementation of Partial Volume Correction Techniques	38
2.2.1	Meltzer Method Implementation	38
2.2.2	Modified-Müller-Gärtner (MMG) Implementation	38
2.2.3	Region-Based Voxel-Wise (RBV) Implementation	39
2.3	Validation and Characterization Using Simulated Phantoms	40
2.3.1	Introduction	40
2.3.2	Materials and Methods	41
2.3.2.1	Subjects	41
2.3.2.2	MR and PiB PET Imaging	41
2.3.2.3	Simulated Phantom Image Generation	42
2.3.2.4	Phantom-Based Evaluation	46
2.3.3	Results	46
2.3.4	Discussion	55
<b>Chapter 3</b>	<b>PiB PET and Post-mortem Measures of Amyloid Load</b>	<b>58</b>
3.1	Introduction	58
3.1.1	The Partial Volume Effect in Amyloid Imaging	58
3.1.2	PiB PET and Postmortem Correlations	60
3.2	Materials and Methods	60
3.2.1	Subjects	60
3.2.2	MR and PiB PET Imaging	63
3.2.3	Brain Autopsy and Dissection	63
3.2.4	6-CN-PiB Histology	64
3.2.5	Region of Interest Matching	65
3.2.6	Partial Volume Correction Application and Sampling	67
3.2.7	Statistical Analysis and Correlations	72
3.3	Results	75
3.3.1	PiB PET Outcome Measures	75
3.3.2	Partial Volume Correction Noise Propagation	79
3.3.3	PiB PET-Postmortem Correlations	83
3.4	Discussion	91

3.4.1	Effect of Partial Volume Correction on PiB SUVR	91
3.4.2	PiB SUVR-Postmortem Correlations and Plateauing	93
3.4.3	Optimal Method for Partial Volume Correction	96
3.4.4	Conclusion	97
<b>Chapter 4 Performance of Simplified Methods in Measuring PiB PET Change</b>		<b>98</b>
4.1	Introduction	98
4.1.1	Comparison of Analytic Methods for PiB PET	98
4.1.2	Quantification of PiB PET in Longitudinal Studies	101
4.2	Materials and Methods	103
4.2.1	Subjects	103
4.2.2	MR and PiB PET Imaging	104
4.2.3	PiB PET Motion Correction and Registration	104
4.2.4	Region of Interest Generation	105
4.2.5	Time-Activity Curve Smoothing	107
4.2.6	PiB PET Quantification	107
4.2.7	Statistical Analysis	110
4.2.8	Population Trajectory Modeling	111
4.3	Results	112
4.3.1	Assessment of Longitudinal Change	113
4.3.2	Relative Tracer Delivery	117
4.3.3	White Matter and Reference Region Influences	117
4.3.4	Population Trajectory Modeling	120
4.4	Discussion	122
4.4.1	Optimal Method for Tracking PiB Change	122
4.4.2	Consideration of Reference Region and White Matter	126
4.4.3	Study Limitations	130
4.4.4	Conclusion	130
<b>Chapter 5 Summary and Conclusions</b>		<b>132</b>
<b>References</b>		<b>135</b>

# List of Tables

<b>Table 1</b> Positron-emitting radionuclides typically used for radiotracers.	4
<b>Table 2</b> Effective resolutions for six modern PET scanners.	5
<b>Table 3</b> Superior parietal SUV values and standard deviations according to phantom and PVC method.	49
<b>Table 4</b> Average recovery coefficients according to phantom and PVC method across all cortical and subcortical grey matter regions.	49
<b>Table 5</b> Demographics of subjects with postmortem and antemortem measures of amyloid load.	62
<b>Table 6</b> Pearson Correlations to 6-CN-PiB (% Area) across all subjects ( $n=12$ ) for all SUVR and PVC methods.	84
<b>Table 7</b> Pearson correlation coefficients between precuneus PiB SUVR for all partial volume correction methods and 6-CN-PiB % area, according to lowest-6-CN-PiB % area subgroups of varying sizes.	95
<b>Table 8</b> Spearman rank-order correlation coefficients between precuneus PiB SUVR for all partial volume correction methods and 6-CN-PiB % area, according to lowest-6-CN-PiB % area subgroups of varying sizes.	95
<b>Table 9</b> Demographics of subjects with baseline and follow-up PiB PET scans.	112
<b>Table 10</b> Outcome measures and change per annum according to analytic method and group (based on smoothed time-activity curves).	115
<b>Table 11</b> SRTM2 GBL $R_1$ values and change per year.	118
<b>Table 12</b> AIC <sub>C</sub> values for model fits between change/annum and average outcome.	120

# List of Figures

**Figure 1 One-dimensional illustration of the partial volume effect.** Note that activity is underestimated in regions neighboring relatively low-activity areas, and activity is overestimated in regions neighboring relatively high-activity areas.  
.....6

**Figure 2 Example of a time-activity curve.** The time-activity curve was measured from a full dynamic PET scan following bolus injection of a radiotracer. Radiotracer rapidly enters the target tissue, hitting a peak concentration in less than five minutes, before clearing the tissue at a relatively slow rate.  
.....16

**Figure 3 Diagram of a one-tissue compartment model,** in which  $C_P$  is the concentration of radioligand in plasma,  $C_T$  is the total concentration of radioligand in tissue,  $K_1$  is the rate in influx into the brain,  $k_2$  is the rate of efflux out of the brain, and BBB is the blood-brain barrier. The diagram is modeled after Normandin et al (2012) [1].  
.....17

**Figure 4 Diagram of a two-tissue compartment model,** in which  $C_P$  is the concentration of radioligand in plasma,  $C_F$  is the concentration of free radioligand in tissue,  $C_{NS}$  is the concentration of nonspecifically bound radioligand in tissue, and  $C_S$  is the concentration of specifically bound radioligand in tissue.  $K_1$  is the rate in influx into the brain,  $k_2$  is the rate of efflux out of the brain,  $k_3$  is the rate of specific binding, and  $k_4$  is the rate of dissociation of specific binding. BBB is the blood-brain barrier. The diagram is modeled after Normandin et al (2012) [1].  
.....17

**Figure 5 Diagram of the Simplified Reference Tissue Model,** in which  $C_P$  is the concentration of radioligand in plasma,  $C_T$  is the concentration of radioligand in tissue, and  $C_{REF}$  is the concentration of radiotracer in the reference region.  $K_1$  is the rate in influx into the target tissue,  $k_{2a}$  is the overall rate from specifically bound to plasma,  $K'_1$  is the rate in influx into the reference tissue, and  $k'_2$  is the rate of efflux out of the reference tissue. The diagram is modeled after Normandin et al (2012) [1].  
.....20

**Figure 6 Example of a Logan plot.** Data from two different subjects with differing slopes are shown. A steeper slope signifies a higher level of binding and higher DVR value.  
.....23

**Figure 7 Illustration of Target and Reference (Ref) time-activity data.** At ~50 minutes post-injection, radiotracer in both the target and reference tissue start to

clear at approximately the same rate, yielding a constant ratio. SUVR is typically calculated during this phase, which is referred to as transient equilibrium.

.....25

**Figure 8 Axial slices of MR and PiB PET images for a PiB-positive (PiB(+)) Alzheimer's disease subject and a PiB-negative (PiB(-)) cognitively normal control subject.** Cortical atrophy and ventricular expansion are apparent in the Alzheimer's disease subject MR image (A), relative to the normal control subject MR image (B). High PiB retention is apparent in frontal, temporal, and precuneus cortical regions in the Alzheimer's disease subject PiB SUVR image (C). Higher signal is seen in white matter areas than cortical grey matter regions in the normal control subject PiB image (D) due to non-specific binding of PiB to white matter and little to no specific binding in cortical grey matter. GM, WM, and CSF voxels are pointed out in the Alzheimer's disease subject MR image (A).

.....30

**Figure 9 Axial slice of an MR image with FreeSurfer parcellation regions overlaid.** Each color signifies a different FreeSurfer parcellation region. Cortical GM regions are parcellated according to sulci and gyri boundaries. Neighboring WM spaces are subsequently parcellated according to the cortical GM parcellation definitions.

.....36

**Figure 10 MR and SUV PiB PET images for the low-PiB-binding and the high-PiB-binding subjects.** The high-PiB-binding SUV PET image (C) is coregistered to its respective MR (A), and the low-PiB-binding SUV PET image (D) is coregistered to its respective MR (B). FreeSurfer parcellations resulting from the MR images were used in producing GTM partial volume corrected data. FreeSurfer parcellations and GTM-corrected data were subsequently used to generate five phantom images for the validation of PVC method implementations.

.....44

**Figure 11 Axial slices of phantom images after smoothing for validating the implementation of Meltzer, MMG, and RBV partial volume correction methods.** Phantom A (A) represents the ideal case for Meltzer PVC with a constant SUV value over all brain tissue voxels. Phantom B (B) represents an ideal case for MMG PVC with two different constant values assigned to GM and WM voxels according to the high-PiB-binding subject (constant GM SUV > constant WM SUV). Phantom C (C) also represents an ideal case for MMG PVC with two different constant values assigned to GM and WM voxels according to the low-PiB-binding subject (constant GM SUV < constant WM SUV). Phantom D (D) represents an ideal case for RBV PVC with different values assigned to each GM region according to the high-PiB-binding subject (variable GM SUV > constant WM SUV). Phantom E (E) represents another ideal case for RBV PVC with different values assigned to each GM region according to the low-PiB-binding subjects (variable GM SUV < constant WM SUV).

.....45

**Figure 12 Phantom A uncorrected and partial volume-corrected regional SUV 50-70 minute values.** Phantom A was assigned a constant SUV value throughout all brain tissue. Uncorrected SUV values underestimate true activity with RC values ranging from 0.66 in the superior parietal region to 0.98 in the putamen. All partial volume correction methods fully recover activity in all cortical and subcortical GM regions.

.....50

**Figure 13 Phantom B uncorrected and partial volume-corrected regional SUV 50-70 minute values.** Phantom B was assigned a constant SUV value for all GM voxels and a constant SUV value for all WM voxels such that GM SUV > WM SUV. Uncorrected SUV values underestimate true activity with RC values ranging from 0.52 in the superior parietal region to 0.83 in the putamen. Meltzer-corrected SUV values also underestimate true activity, though to a lesser extent, with RC values ranging from 0.79 in the superior parietal region to 0.92 in the thalamus. The MMG- and RBV-correction methods fully recover activity in all cortical and subcortical GM regions.

.....51

**Figure 14 Phantom C uncorrected and partial volume-corrected regional SUV 50-70 minute values.** Phantom C was assigned a constant SUV value for all GM voxels and a constant SUV value for all WM voxels such that GM SUV < WM SUV. Uncorrected SUV values underestimate true activity in all regions except the putamen, in which activity is overestimated. Meltzer-corrected SUV values overestimate true activity across all regions with RC values ranging from 1.09 in the thalamus to 1.25 in the middle frontal. The MMG- and RBV-correction methods fully recover activity in all cortical and subcortical GM regions.

.....52

**Figure 15 Phantom D uncorrected and partial volume-corrected regional SUV 50-70 minute values.** Phantom D was assigned variable SUV values across GM regions such that GM SUV > WM SUV. Uncorrected and Meltzer-corrected SUV values underestimate true activity in all regions. MMG-corrected RC values ranged between 0.97 in the precuneus and 1.02 in the anterior cingulate. The RBV-correction method fully recovers activity in all cortical and subcortical GM regions.

.....53

**Figure 16 Phantom E uncorrected and partial volume-corrected regional SUV 50-70 minute values.** Phantom E was assigned variable SUV values across GM regions such that GM SUV < WM SUV. Meltzer-corrected SUV values overestimate true activity in all regions with RC values ranging from 1.04 in the thalamus to 1.34 in the putamen. MMG-corrected RC values ranged between 0.94 in the anterior cingulate and 1.07 in the putamen. The RBV-correction method is the only PVC method to fully recover activity in all cortical and subcortical GM regions.

.....54

**Figure 17 Snapshot of ROI matching between post-mortem tissue and antemortem MR image for subject PiB-09.** From left-to-right, (A) is the post-mortem autopsy tissue with excised regions overlaid, (B) is the antemortem MR image with ROIs hand-drawn to match those in the autopsy photo, and (C) is the PiB SUVR image with hand-drawn ROIs overlaid.

.....66

**Figure 18 MR image for subject PiB-02 with corresponding FreeSurfer segmentations and parcellations.** The antemortem MR image (A) was segmented into (B), a whole brain tissue binary mask that was used for the Meltzer-correction and (C), GM (red) and WM (green) binary masks for use in MMG-correction. (D) Hand-drawn autopsy-matched ROIs (squares) were inserted into the FreeSurfer cortical parcellation for use in RBV PC correction.

.....69

**Figure 19 Uncorrected and partial volume-corrected SUVR60 PiB PET images for subject PiB-02.** The Meltzer-corrected SUVR image (B) was masked with a whole brain-tissue binary map to remove relatively high activity voxels outside of the brain. The MMG-corrected SUVR image (C) was masked with a binary grey matter map to remove relatively high-activity voxels from CSF and WM spaces. Neither the uncorrected (A) nor the RBV-corrected (D) SUVR images was masked. As part of the RBV-correction method, voxels outside of parcellated regions are set to zero.

.....70

**Figure 20 Synopsis of workflow for autopsy-guided antemortem PiB PET partial volume correction and sampling.** Work that is part of this thesis is circled in yellow. Both manual and automated techniques were used to generate regions of interest for matching autopsy slab dissected regions and generating anatomical regions for partial volume correction. Three partial volume correction methods were applied to antemortem PET data.

.....71

**Figure 21 A ventricular CSF region of interest overlaid on subject PiB-01 MR and SUVR PiB PET images.** The square region of interest was drawn on the MR image (A) and transferred to the coregistered SUVR60 PiB PET image (B). Noise magnification factors were calculated for 11 of the 12 subjects based on ventricular CSF ROIs in order to assess the noise propagation of each of the partial volume correction methods applied.

.....74

**Figure 22 Mean precuneus SUVR60 values across subjects and partial volume correction methods.** On average, the Meltzer PVC method increased precuneus SUVR values by 14.9%. The MMG and RBV methods increased SUVR values on average by 51.5% and 52.2%, respectively.

.....76

**Figure 23 Mean precuneus SUVR70 values across subjects and partial volume correction methods.** On average, the Meltzer PVC method increased precuneus SUVR values by 14.8%. The MMG and RBV methods increased SUVR values on average by 54.5% and 54.1%, respectively.

.....77

**Figure 24 Correlation between SUVR60 and SUVR70 in the precuneus across subjects.** The slope for the linear relationship is 1.064 with a highly significant Pearson's correlation coefficient of 0.998 ( $p < 0.001$ ).

.....78

**Figure 25 Noise magnification factors for precuneus SUVR60 outcome measures across PVC techniques.** The largest NMFs were generated by the MMG method in 7 cases and by the Meltzer method in 5 cases.

.....80

**Figure 26 Noise magnification factors for precuneus SUVR70 outcome measures across PVC techniques.** The largest NMFs were generated by the MMG method in 8 cases and by the Meltzer method in 4 cases.

.....81

**Figure 27 Noise magnification factors for ventricular CSF SUVR60 measures across PVC techniques.** Subject PiB-04 was excluded from CSF NMF assessment as the ventricles in the subject were too small to fit a CSF region of interest. Across all subjects the magnitude of the CSF NMF was greater for MMG-corrected data than Meltzer-corrected data. In the single case of subject PiB-09, MMG-correction resulted in a negative CSF NMF of -3.09. CSF NMFs for RBV-corrected data are not shown as the PVC method results in zero voxels outside of the brain parcellation.

.....82

**Figure 28 Correlations between 6-CN-PiB % area and SUVR60 in the precuneus across subjects and partial volume correction methods.** Plots for uncorrected SUVR (A), Meltzer-corrected SUVR (B), MMG-corrected SUVR(C), and RBV-corrected SUVR (D) are shown. Subject PiB identifiers (**Table 7**) are overlaid onto each plot. Pearson's correlation is greatest for uncorrected SUVR (0.920) followed by RBV-corrected (0.885), MMG-corrected (0.868), and Meltzer-corrected (0.852). All correlations are statistically significant at  $p < 0.05$  despite the SUVR value seeming to plateau relative to 6-CN-PiB % Area at ~10%.

.....85

**Figure 29 Correlations between 6-CN-PiB % Area and SUVR70 in the precuneus across subjects and partial volume correction methods.** Plots for uncorrected SUVR (A), Meltzer-corrected SUVR (B), MMG-corrected SUVR(C), and RBV-corrected SUVR (D) are shown. Subject PiB identifiers are overlaid onto each plot. As in the case of SUVR60, Pearson's correlation is greatest for uncorrected SUVR (0.923) followed by RBV-corrected (0.890), MMG-corrected (0.872), and



Meltzer-corrected (0.859). As in the case of SUVR60, SUVR70 data seems to plateau relative to 6-CN-PiB % Area at ~10%.

.....86

**Figure 30 Correlations between 6-CN-PiB % Area and SUVR60 in the frontal cortex across subjects and partial volume correction methods.** Plots for uncorrected SUVR (A), Meltzer-corrected SUVR (B), MMG-corrected SUVR(C), and RBV-corrected SUVR (D) are shown. Subject PiB identifiers (**Table 7**) are overlaid onto each plot. Similar to precuneus data, Pearson's correlation for the frontal cortex is greatest for uncorrected SUVR (0.737) followed by RBV-corrected (0.723), MMG-corrected (0.721), and Meltzer-corrected (0.661). However, all correlations are significant at  $p < 0.05$ . SUVR60 frontal cortex data seems to plateau at a 6-CN-PiB % Area of ~5%.

.....87

**Figure 31 Correlation between 6-CN-PiB % Area and SUVR70 in the frontal cortex across subjects and partial volume correction methods.** Plots for uncorrected SUVR (A), Meltzer-corrected SUVR (B), MMG-corrected SUVR(C), and RBV-corrected SUVR (D) are shown. As in the case of SUVR60, Pearson's correlation for SUVR70 in the frontal cortex is greatest for uncorrected SUVR (0.741) followed by RBV-corrected (0.729), MMG-corrected (0.724), and Meltzer-corrected (0.668).

.....88

**Figure 32 Correlations between 6-CN-PiB % Area and SUVR60 in the occipital cortex across subjects and partial volume correction methods.** Plots for uncorrected SUVR (A), Meltzer-corrected SUVR (B), MMG-corrected SUVR(C), and RBV-corrected SUVR (D) are shown. Subject PiB identifiers are not overlaid onto the plots. A maximum 6-CN-PiB % Area of 5.57% is seen in PiB-23, relatively little compared to the precuneus and frontal cortex. PiB-16 has a 6-CN-PiB % Area of 5.02%, and PiB-05 has a % Area of 4.92. The maximum correlation to 6-CN-PiB % Area is seen in RBV-corrected data (0.866), followed by uncorrected SUVR60 (0.846), Meltzer-corrected (0.825), and MMG-corrected (0.817).

.....89

**Figure 33 Correlations between 6-CN-PiB % Area and SUVR70 in the occipital cortex across subjects.** Plots for uncorrected SUVR (A), Meltzer-corrected SUVR (B), MMG-corrected SUVR(C), and RBV-corrected SUVR (D) are shown. Subject PiB identifiers are not overlaid onto the plot. As in the case of SUVR60 occipital cortex outcomes, the maximum correlation to 6-CN-PiB % Area is seen in RBV-corrected SUVRs (0.855), followed by uncorrected SUVR60 (0.835), Meltzer-corrected (0.811), and MMG-corrected (0.795).

.....90

**Figure 34 Regions of interest hand-drawn in ROIttool overlaid on a MR image and SUVR PiB PET image for a cognitively normal control subject.** Regions of interest were drawn on the (A) MR image and then transferred to the (B) PET image after registration of the PET to MR image.

.....	106
<b>Figure 35 Cerebellar reference region time-activity curve sampled from an Alzheimer's disease patient before smoothing and after smoothing.</b> Note slight increases in radioactivity during the washout phase at 45 minutes and 55 minutes are removed after smoothing.	109
<b>Figure 36 Box-and-whisker plots of global region group change per annum according to SUVR60, SUVR70, SUVR90, Logan DVR, and SRTM2 DVR.</b> Data for PiB-positive groups at baseline (A) include, from left to right, NC(+), MCI(+), and AD. Data for PiB-negative at baseline (B) include, from left to right, NC(-), MCI(-), and NC(-/+). Results are based on smoothed time-activity curves.	116
<b>Figure 37 Relationship between annual change in SWM and change in GBL SUVR70 for NC(-).</b> A significant correlation is observed with a Pearson correlation coefficient of 0.69 at $p = 0.002$ , suggesting change in SWM over time influences change in GBL SUVR70 for NC(-) subjects. Results are based on smoothed time-activity curves.	119
<b>Figure 38 Model fits for study population data across outcome measures.</b> SRTM2 DVR, SUVR60, and SUVR70 outcome measures were all best described by the 2-parameter single-exponential model. Logan DVR outcome measures were best fit by the Gaussian model, and SUVR90 data was best fit by a linear function.	121
<b>Figure 39 Box-and-whisker plots of change per year of AD subjects across all outcome measures based on raw time-activity curves and smoothed time-activity curves.</b> Data based on raw time-activity curves are presented in (A) and data based on smoothed time-activity curves are presented in (B). The interquartile ranges (IQR) of SUVR60, SUVR70, SUVR90, Logan DVR, and SRTM2 DVR before time-activity curve smoothing are 0.121, 0.127, 0.203, 0.095, and 0.154, respectively. After smoothing they are 0.087, 0.064, 0.080, 0.086, and 0.097, respectively, representing decreases in variability of 28% for SUVR60, 49% for SUVR70, 61% for SUVR90, 9% for Logan DVR, and 37% for SRTM2 DVR.	129

# List of Abbreviations

ACG	Anterior Cingulate
AD	Alzheimer's disease
ADRC	Alzheimer's Disease Research Center (University of Pittsburgh)
AIC <sub>C</sub>	Corrected Akaike Information Criteria
AVS	Anterior Ventral Striatum
A $\beta$	Amyloid-beta
BBB	Blood-Brain Barrier
BP	Binding Potential
BP <sub>ND</sub>	Non-displaceable Binding Potential
BP <sub>ND</sub>	Non-displaceable Binding Potential
CER	Cerebellar Grey Matter
C <sub>FP</sub>	Concentration of free radioligand in plasma
C <sub>FT</sub>	Concentration of free radioligand in brain tissue
C <sub>ND</sub>	Concentration of non-displaceable radioligand in brain tissue
C <sub>NS</sub>	Concentration of non-specifically bound radioligand in brain tissue
CoV	Coefficient of Variation
C <sub>P</sub>	Concentration of radioligand in plasma
C <sub>S</sub>	Concentration of specifically bound radioligand in brain tissue
CSF	Cerebrospinal Fluid
CT	Computed Tomography
C <sub>T</sub>	Concentration of total radioligand in brain tissue
DLB	Dementia with Lewy Bodies
DVR	Distribution Volume Ratio
FDG	<sup>18</sup> F-Fluorodeoxyglucose
FOV	Field of View
FRC	Frontal Cortex
FSL	The FMRIB Software Library
FTD	Frontotemporal Dementia
FWHM	Full Width at Half Maximum
GBL	Global Region
GM	Grey Matter
GTM	Geometric Transform Matrix
HIP	Hippocampus
IQR	Interquartile Range
K <sub>1</sub>	Rate constant for influx from plasma to target tissue
K <sub>1</sub> '	Rate constant for influx from plasma to reference tissue
k <sub>2</sub>	Rate constant for efflux from plasma to target tissue
k <sub>2</sub> '	Rate constant for efflux from reference tissue to plasma
k <sub>2a</sub>	Overall rate constant from specifically bound to plasma
k <sub>3</sub>	Rate constant for specific binding from non-displaceable
k <sub>4</sub>	Rate constant for dissociation of specific binding
LOR	Line of Response
LTC	Temporal Lobe
MCI	Mild Cognitive Impairment

MCI(-)	PiB-negative Mild Cognitive Impairment
MCI(+)	PiB-positive Mild Cognitive Impairment
MG	Müller-Gärtner (partial volume correction technique)
MMG	Modified Müller-Gärtner (partial volume correction technique)
MMSE	Mini Mental State Exam
MPRAGE	Magnetized Prepared Rapid Gradient Echo
MR	Magnetic Resonance
NC	Cognitively Normal Control
NC(-)	PiB-negative Normal Control
NC(-/+)	PiB-negative to PiB-positive Converting Normal Control
NC(+)	PiB-positive Normal Control
NFT	Neurofibrillary Tangle
NMF	Noise Magnification Factor
OCC	Occipital Cortex
PAR	Parietal Lobe
PET	Positron Emission Tomography
PiB	<sup>11</sup> C-Pittsburgh Compound B
PiB(-)	PiB-negative (negligible amyloid- $\beta$ deposits detected by PET)
PiB(+)	PiB-positive (amyloid- $\beta$ deposits detected by PET)
PRC	Precuneus
PSF	Point Spread Function
PUT	Putamen
PVC	Partial Volume Correction
PVE	Partial Volume Effect
$R_1$	Ratio of $K_1$ to $K_1'$
RBV	Region-Based Voxel-Wise (partial volume correction technique)
RC	Recovery Coefficient
ROI	Region of Interest
SPGR	Spoiled Gradient Recalled
SPM8	Statistical Parametric Mapping version 8 Software
SRTM	Simplified Reference Tissue Model
SSQ	Residual Sum of Squares
SUV	Standardized Uptake Value
SUV60	Standardized Uptake Value calculated 40-60 minutes post-injection
SUV70	Standardized Uptake Value calculated 50-70 minutes post-injection
SUV90	Standardized Uptake Value calculated 60-90 minutes post-injection
SUVR	Standardized Uptake Value Ratio
SUVR60	Standardized Uptake Value Ratio 40-60 minutes post-injection
SUVR70	Standardized Uptake Value Ratio 50-70 minutes post-injection
SUVR90	Standardized Uptake Value Ratio 60-90 minutes post-injection
SWM	Subcortical White Matter
$V_{ND}$	Non-displaceable Distribution Volume
$V_S$	Specifically Bound Distribution Volume
$V_T$	Total Distribution Volume
WM	White Matter

# Chapter 1

## Background and Overview

This chapter introduces position emission tomography (PET) imaging and the partial volume effect that arises from the limited spatial resolution of PET. Methods of quantifying PET data are then introduced. Alzheimer's disease and PET imaging of amyloid beta plaques in vivo is subsequently discussed before an overview of the current work is presented.

### 1.1 Background

#### 1.1.1 Positron Emission Tomography

PET is a nuclear medicine imaging technique that enables imaging of functional processes within the living subject. In PET imaging, positron-emitting radionuclides are incorporated into chemical compounds or radiotracers. Radiotracers are then injected intravenously prior to the start of scanning. Through positron emissions or radioactive decay, these radiotracers are used to trace the path of biochemical reactions or study the distribution of a substance within the body. When a positron combines with an electron in vivo, an annihilation event is triggered. The annihilation event simultaneously produces two high-energy photons or gamma rays (511 keV), which are emitted approximately 180° apart (collinear). A PET scanner coincident event is measured when two opposing detectors detect two photons within a small time window (order of nanoseconds). This constitutes a "count", while also defining a line of response (LOR). LORs are

then reconstructed to generate a 3D PET image. PET imaging is highly sensitive and allows for detection of radiotracer in vivo in the nanomolar to picomolar range.

Examples of positron-emitting radionuclides used in PET imaging, and their respective half-lives, are presented in **Table 1**. The radioactivity remaining in a radionuclide sample,  $A(t)$  (mCi or MBq), after time  $t$  (min) can be calculated using the equation

$$A(t) = A_0 e^{-\lambda t}, \quad (1)$$

in which  $A_0$  is the initial activity of the radiotracer and  $\lambda$  ( $\text{min}^{-1}$ ) is the decay constant,

$$\lambda = \frac{\ln 2}{\text{half-life}}. \quad (2)$$

In PET studies, the activity concentration is based on the measurement of annihilation events, but the desired analysis outcome should be proportional to the physiological process-of-interest. As time passes during a PET scan, the injected dose decays according to the half-life of the radionuclide. As a result, radioactivity concentration measured by the PET scanner is subject to the statistical nature of radioactive decay. Decay correction is therefore performed on measured radioactivity concentrations in PET scans based on **Equation 1**.

PET imaging is subject to a number of sources of noise, including scatter coincidences and accidental or random coincidences. Scatter coincidences occur when at least one of the detected photons has undergone a Compton scattering event prior to detection. Compton scattering occurs when a photon interacts with weakly bound or free electrons, losing energy and changing direction. With one or more of the photons changing direction, the LOR observed by the PET scanner is

misplaced from the original LOR produced by the annihilation event. Accidental coincidences occur when two simultaneous annihilation events produce two photons that are detected by opposing detectors within the coincidence time window. Scatter coincidences map misplaced counts in the final image, and accidental coincidences map false counts.

The total counts for a pair of coincidence detectors in a PET scan can be described as the sum of true coincidences, scatter coincidences, and accidental coincidences [2]. The signal-to-noise ratio in PET imaging is therefore directly proportional to the number of true coincidences. A greater number of true coincidences detected results in a higher signal-to-noise ratio, and fewer true coincidences results in a poorer signal-to-noise ratio. As such, the signal-to-noise ratio of a PET scan is also dependent on time passed after injection and the half-life of the radionuclide administered. As time passes in a PET scan, less radioactivity is measured due to radioactive decay, and the signal-to-noise ratio is reduced.

Relative to magnetic resonance (MR) imaging and X-ray computed tomography (CT), PET has a poor spatial resolution (**Table 2**) due to a number of factors that include detector size, positron range, and noncolinearity [3]. At the center of the scanner field of view (FOV), the intrinsic PET scanner resolution is approximately  $d/2$ , where  $d$  is the diameter of the detector. This intrinsic resolution deteriorates towards the edge of the transaxial FOV, but is remarkably constant over the central third of the region. The range of the positron refers to the distance it travels before interacting with an electron and annihilating, and is dependent on its kinetic energy. As a result, the site of positron emission can differ from the site of

annihilation. Noncolinearity refers to the deviation of two annihilation photons from the exact 180° emission. Electrons and positrons are not completely at rest when they annihilate and some small residual momentum of the positron can create a maximum deviation of about 0.3°. The observed LOR therefore may not intersect the point of annihilation.

**Table 1** Positron-emitting radionuclides typically used for radiotracers.

Radionuclide	Half life (min)
<sup>18</sup> F	109
<sup>11</sup> C	20
<sup>13</sup> N	10
<sup>15</sup> O	2

### 1.1.2 The Partial Volume Effect

The spatial resolution of a PET image is typically characterized by a point spread function (PSF), which corresponds to the blurring of an image of a point source and is modeled as a Gaussian function with a defined full width at half maximum (FWHM). The measured radioactivity concentrations in the PET image should be directly proportional to the concentration of the radiotracer in vivo. This holds true for structures with sizes that are 2xFWHM of the scanner or greater [4]. However, in brain PET imaging, structures of interest can fall below this threshold and exhibit reductions in their recovery coefficient (RC), which is the apparent isotope concentration in the image divided by the true isotope concentration. This is due to radioactivity blurring out, or spilling out of the region. Quantification in PET imaging is further confounded by the radioactivity in neighboring regions. The



blurring effect of the spatial resolution also causes activity from surrounding regions to spill in. This spill-in/spill-out of activity, or cross-contamination, between structures due to the finite resolution of the PET scanner is known as the partial volume effect (PVE) [4, 5], and is illustrated in **Figure 1**.

**Table 2** Effective resolutions for six modern PET scanners.

Manufacturer	Philips		Siemens			GE Healthcare
Model	Vereos Digital PET/CT	GEMINI TF PET/CT	ECAT HRRT	Biograph mCT	ECAT HR+*	Discovery PET/CT 710
Spatial Resolution (mm)	4.1	4.7	2.3	4.4	6.0	4.5

\* University of Pittsburgh PET Center scanner, in-house measures

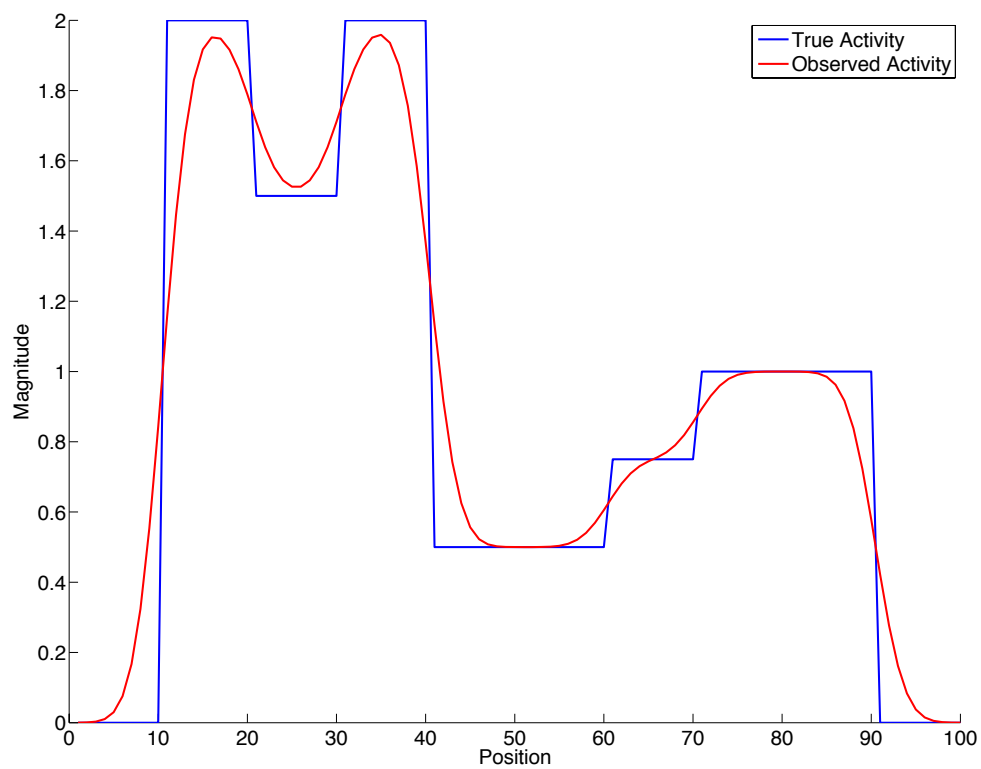


**Figure 1 One-dimensional illustration of the partial volume effect.** Note that activity is underestimated in regions neighboring relatively low-activity areas, and activity is overestimated in regions neighboring relatively high-activity areas.

### 1.1.3 Partial Volume Correction Approaches

A number of partial volume correction (PVC) methods have been proposed to address the cross-contamination effect caused by the limited spatial resolution in the image domain. The goal of PVC is to restore true activity or increase the RC by reversing the effect of the PSF. A number of these methods are summarized, along with their strengths and weaknesses, below.

#### 1.1.3.1 Meltzer Method

The Meltzer voxel-based method [6, 7] describes the observed PET image  $I_O(x)$  as the convolution of the sum of true tracer distribution in the brain,  $I_T(x)$ , and cerebrospinal fluid (CSF),  $I_C(x)$  with the scanner point spread function,  $h(x)$ :

$$I_O(x) = (I_T(x)s_T(x) + I_C(x)s_C(x)) \otimes h(x), \quad (3)$$

where  $x$  is the three-dimensional position vector, and  $s_T(x)$  and  $s_C(x)$  are voxel maps of tissue and non-tissue, respectively, segmented from higher-resolution structural MR images. CSF radiotracer concentration is assumed to be zero, so that true tracer distribution in the brain can be solved for with

$$I_T(x) = \frac{I_O(x)}{s_T(x) \otimes h(x)}. \quad (4)$$

The Meltzer method is a two-compartment method. It only accounts for spill-out from the brain into CSF space, and therefore specifically addresses PVEs related to cortical atrophy and ventricular expansion. It does not account for heterogeneity within tissue. Cross-contamination between grey matter (GM) and white matter (WM) and regions within grey matter is also not accounted for.

### 1.1.3.2 Müller-Gärtner Method

The Müller-Gärtner Method (MG) [8] accounts for GM-to-WM cross-contamination by extending Meltzer's framework to three compartments. True radiotracer distribution in the brain is split into the sum of true distribution in grey matter,  $I_G(x)$ , and white matter,  $I_W(x)$ , such that  $I_T(x) = I_G(x) + I_W(x)$ . By assuming white matter is homogenous with a constant radiotracer concentration,  $c_W$ ,  $I_G(x)$  can be solved for using

$$I_G(x) = \frac{I_O(x) - c_W(s_W(x) \otimes h(x))}{s_G(x) \otimes h(x)} \quad (5)$$

where  $s_G(x)$  and  $s_W(x)$  are voxel maps of GM and WM based on structural MR images.  $c_W$  is typically estimated from a white matter region, such as subcortical WM, thought to be free of PVEs.

While the MG method addresses cross-contamination between GM and WM, it does not account for heterogeneity within WM nor spill-over between GM regions. The MG method also relies on an accurate assessment of true white matter concentration.

### 1.1.3.3 The Geometric Transform Matrix Method

The geometric transform matrix (GTM) method [9] can account for spill over between grey matter regions unlike the Meltzer and MG methods. The brain is parcellated into non-overlapping anatomical regions of assumed homogenous activity based on an MR image, such that

$$I_O(x) = \sum_{i=1}^N c_i(s_i(x) \otimes h(x)), \quad (6)$$

where  $N$  is the number of regions that the brain has been parcellated into,  $s_i(x)$  is the  $i^{th}$  parcellation's voxel map, and  $c_i$  is the  $i^{th}$  parcellation's true activity. Explicitly writing out the convolution operator yields

$$I_o(x) = \sum_{i=1}^N c_i \int_{D_i} h(x, x') dx', \quad (7)$$

in which  $x'$  is a three-dimensional position vector and  $D_i$  is the  $i^{th}$  parcellation's domain defined by non-zero voxels in  $s_i(x)$ . It follows that any given parcellation's mean observed value  $C_j$  is the sum of all parcellations' contributions to its domain  $D_j$  divided by the number of voxels the parcellation contains,  $n_{pix}$ :

$$C_j = \frac{1}{n_{pix}} \sum_{i=1}^N c_i \int_{D_j} \int_{D_i} h(x, x') dx' dx. \quad (8)$$

Note that the amount of spill-out is assessed when  $i=j$ , and the amount of spill-in from a neighboring region is assessed when  $i \neq j$ . Rewriting **Equation 8** as

$$C_j = \sum_{i=1}^N c_i w_{ij}, \quad (9)$$

$$w_{ij} = \frac{1}{n_{pix}} \int_{D_j} \int_{D_i} h(x, x') dx' dx, \quad (10)$$

the mean observed parcellation values can be written as a system of linear equations,

$$\begin{bmatrix} C_1 \\ C_2 \\ \vdots \\ C_N \end{bmatrix} = \begin{bmatrix} w_{11} & w_{12} & \cdots & w_{1N} \\ w_{21} & w_{22} & \cdots & w_{2N} \\ \vdots & \vdots & \ddots & \vdots \\ w_{N1} & w_{N2} & \cdots & w_{NN} \end{bmatrix} \begin{bmatrix} c_1 \\ c_2 \\ \vdots \\ c_N \end{bmatrix}. \quad (11)$$

The geometric transform matrix of weighting factors,  $w_{ij}$ , can then be inverted to solve for all true activities in each parcellation simultaneously.

Unlike the Meltzer and MG methods, the GTM method only produces regional estimates of true activity and does not correct for PVEs on a voxel basis. Further,

the accuracy of the GTM method is dependent on the assumption of homogeneity being valid for each defined domain or region, and parcellation of the the brain into anatomical regions of assumed homogeneity based on the MR image can be a non-trivial time-consuming step.

#### 1.1.3.4 Modified Müller-Gärtner Method

Rousset et al (1998) [10] proposed an alternative approach to finding an estimate of white matter concentration,  $c_W$ , for the MG method by initially using the GTM method on a set of regions including a gross white matter region. This is known as the Modified Müller-Gärtner (MMG) method. While the initial use of the GTM removes the need for a manually generated true white matter concentration estimate, it retains the same drawbacks as the MG method. Specifically, it still does not address spillover of activity between grey matter regions.

#### 1.1.3.5 The Region-Based Voxel-Wise Method

The Region-Based Voxel-Wise (RBV) method [11] extends the GTM method to correct on a voxel basis by performing a final voxel-wise correction similar to Yang et al (1996) [12]. A synthetic PET image,  $I_S(x)$ , is created from the parcellation maps,  $s_i(x)$ , and true concentrations,  $c_i$ , derived from an initial GTM step, such that

$$I_S(x) = \sum_{i=1}^N c_i s_i(x). \quad (12)$$

A voxel-wise correction is then performed on the observed PET image using a simple ratio:

$$I_T(x) = I_O(x) \left[ \frac{I_S(x)}{I_S(x) \otimes h(x)} \right]. \quad (13)$$

RBV demonstrates good cortical activity recovery on a regional basis, but like GTM its accuracy is highly dependent on the assumption that activity within defined regions is homogeneous.

#### **1.1.4 PET Quantification Methods: Radioligand-Protein Binding**

PET imaging is an optimal method in quantifying a number of physiological processes, including cerebral blood flow, glucose metabolism, enzyme activity and enzyme abundance, and ligand-protein binding interactions. The following section describes analytic methods specific to quantification of radioligand-protein binding in PET imaging.

##### **1.1.4.1 Pharmacokinetic Nomenclature**

Innis et al (2007) [13] established consensus nomenclature for radioligand imaging and quantification. This section summarizes the nomenclature from Innis et al (2007) that is relevant to the following work.

For brain PET studies that quantify specific radioligand-protein binding interactions, a radioactive ligand, or radioligand, is first injected into the body intravenously. A fraction of the injected radioligand then crosses the blood-brain barrier (BBB) via diffusion. The BBB is a semi-permeable barrier formed by endothelial cells and tight junctions that separates circulating blood from the brain, such that only small gaseous molecules and small lipophilic drugs can diffuse across [14-16]. Most radioligands cross the BBB via passive diffusion.

Once in the brain, injected radioligand binds specifically to target receptors or molecules, binds nonspecifically, or remains free in tissue water. The total concentration of radioligand in brain tissue ( $C_T$ ) can therefore be expressed as

$$C_T = C_S + C_{NS} + C_{FT}, \quad (14)$$

in which  $C_S$  is the concentration of specifically bound radioligand,  $C_{NS}$  is the concentration of nonspecifically bound radioligand, and  $C_{FT}$  is the concentration of free radioligand. Further, the combination of free and nonspecific ligand is referred to as non-displaceable uptake, such that

$$C_{ND} = C_{NS} + C_{FT}, \quad (15)$$

in which  $C_{ND}$  is the non-displaceable concentration of radioligand. Radioligand concentrations are expressed in units of radioactivity (becquerels or curies) divided by volume, such as Bq/mL or Ci/cm<sup>3</sup>.

The radioligand volume of distribution in PET is defined as the equilibrium ratio of tissue radioligand concentration to plasma radioligand concentration ( $C_P$ ). The total distribution volume in tissue is therefore

$$V_T = \frac{C_T}{C_P}, \quad (16)$$

and the non-displaceable distribution volume is given by

$$V_{ND} = \frac{C_{ND}}{C_P}. \quad (17)$$

The free fraction of radioligand in plasma that is diffusible in plasma at equilibrium is referred to as  $f_p$ , the plasma free fraction. The concentration of free radioligand in plasma,  $C_{FP}$ , is therefore

$$C_{FP} = f_p C_P. \quad (18)$$



The comparable non-displaceable free fraction of radioligand in brain tissue is  $f_{ND}$ , which relates free and non-displaceable concentrations:

$$C_{FT} = f_{ND} C_{ND} . \quad (19)$$

The binding potential ( $BP$ ) refers to the ratio of receptor or molecule density in tissue ( $B_{max}$ ) to the radioligand equilibrium dissociation constant ( $K_D$ ), the inverse of radioligand binding affinity [17].

$$BP = \frac{B_{max}}{K_D} . \quad (20)$$

Binding potential reflects the capacity of a tissue for radioligand-binding interactions. Binding potential without a subscript refers to “true” in vitro specific binding. However, in vivo  $B_{max}$  is typically not measureable as a subset of target receptors or molecules may be occupied by endogenous substances selective for the target. Non-displaceable binding potential ( $BP_{ND}$ ) refers to the ratio of specifically bound radioligand to non-displaceable radioligand in tissue. It compares the concentration of radioligand in a receptor- or molecule-rich area to the concentration in a receptor- or molecule-free area [13].

$$BP_{ND} = \frac{V_S}{V_{ND}} . \quad (21)$$

Since specific binding is equal to  $V_T - V_{ND}$ ,  $BP_{ND}$  can be described as

$$BP_{ND} = \frac{V_T - V_{ND}}{V_{ND}} = \frac{V_T}{V_{ND}} - 1 . \quad (22)$$

The ratio of  $V_T$  to  $V_{ND}$  is referred to as the distribution volume ratio (DVR) and is widely used to represent receptor or molecule density. As such,  $DVR = BP_{ND} + 1$ .

#### 1.1.4.2 Compartmental Modeling

PET scans may be reconstructed into dynamic images, 4D images consisting of multiple 3D volumes, if data are acquired over multiple time frames. In a dynamic PET scan, time frames at the start of PET acquisition are typically short (~15 seconds) to capture rapid changes in radioactivity concentration after bolus injection of the radiotracer. Time frames at the end of PET acquisition are relatively longer (5-10 minutes) to minimize the influence of noise.

Regional time-activity curves are generated from dynamic PET scans by sampling each of the PET frames with a region of interest, assuming there is no patient movement between frames, generating a curve of average radioactivity concentration versus time and visualizing the kinetic behavior of the radiotracer. An example time-activity curve is shown in **Figure 2**.

The “gold standard” for describing the pharmacokinetics of a radiotracer based of a PET scan is typically compartmental modeling, which models the passage of radiotracer from plasma into brain tissue and the binding to targets therein. The compartments represent either a location or state of the radiotracer, and the movements of the radiotracer are described by rate constants ( $k$ ). In a one-tissue compartment model, only diffusion of the radioligand across the blood-brain barrier is described. The standard one-tissue compartment is shown in **Figure 3**. The rate of change of tissue radiotracer concentration ( $dC_T/dt$ ) is described by

$$\frac{dC_T(t)}{dt} = K_1 C_P(t) - k_2 C_T(t) \quad (23)$$

in which  $K_1$  is the rate constant for transfer from plasma to tissue with units of mL/cm<sup>3</sup>/min, and  $k_2$  is the rate constant for efflux from brain tissue to plasma

transfer with units of  $\text{min}^{-1}$ . Solving for  $C_T$  in **Equation 23**,  $C_T$  is equivalent to the convolution of radiotracer concentration in plasma with an exponential term:

$$C_T(t) = C_P(t) \otimes K_1 e^{-k_2 t} \quad (24)$$

A two-tissue compartmental model (**Figure 4**) can distinguish specifically bound radiotracer from non-displaceable radiotracer using rate constants  $k_3$  (transfer from non-displaceable to specifically bound;  $\text{min}^{-1}$ ) and  $k_4$  (transfer from specifically bound to non-displaceable;  $\text{min}^{-1}$ ). The rate of change of non-displaceable radiotracer concentration ( $dC_{ND}/dt$ ) and specifically bound radiotracer concentration ( $dC_S/dt$ ) are described by the equations

$$\frac{dC_{ND}(t)}{dt} = K_1 C_P(t) - (k_2 + k_3) C_{ND}(t) + k_4 C_S(t) \quad (25)$$

$$\frac{dC_S(t)}{dt} = k_3 C_{ND}(t) - k_4 C_S(t) \quad (26)$$

The full solution to  $C_{ND}$  and  $C_S$  is available in Gunn. et al 2015 [18].

Both 1-tissue compartment and 2-tissue compartment cases are single-input-single-output systems with the output,  $C_T$ , being a PET time-activity curve and the input  $C_P$  being plasma radioactivity concentration, typically measured by sampling the radial artery via cannulation.

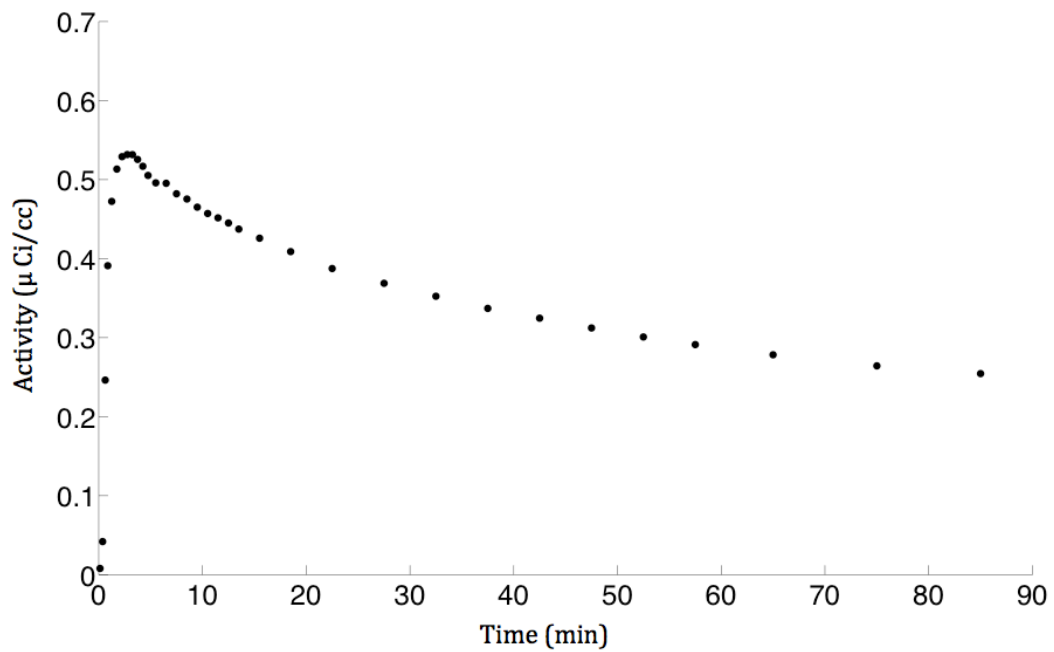


**Figure 2 Example of a time-activity curve.** The time-activity curve was measured from a full dynamic PET scan following bolus injection of a radiotracer. Radiotracer rapidly enters the target tissue, hitting a peak concentration in less than five minutes, before clearing the tissue at a relatively slow rate.

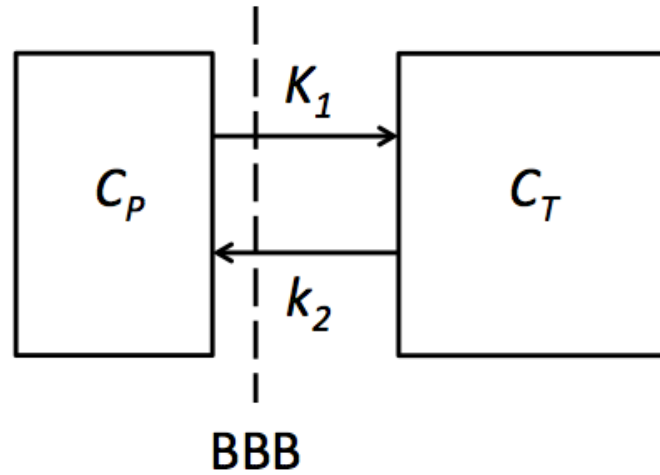


**Figure 3 Diagram of a one-tissue compartment model**, in which  $C_P$  is the concentration of radioligand in plasma,  $C_T$  is the total concentration of radioligand in tissue,  $K_1$  is the rate in influx into the brain,  $k_2$  is the rate of efflux out of the brain, and BBB is the blood-brain barrier. The diagram is modeled after Normandin et al (2012) [1].

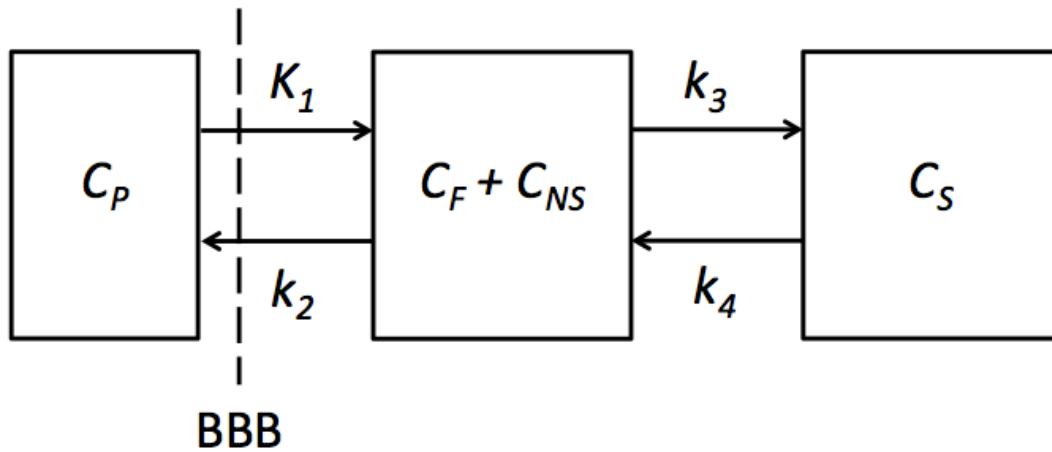


**Figure 4 Diagram of a two-tissue compartment model**, in which  $C_P$  is the concentration of radioligand in plasma,  $C_F$  is the concentration of free radioligand in tissue,  $C_{NS}$  is the concentration of nonspecifically bound radioligand in tissue, and  $C_S$  is the concentration of specifically bound radioligand in tissue.  $K_1$  is the rate in influx into the brain,  $k_2$  is the rate of efflux out of the brain,  $k_3$  is the rate of specific binding, and  $k_4$  is the rate of dissociation of specific binding. BBB is the blood-brain barrier. The diagram is modeled after Normandin et al (2012) [1].

With both input and output time-activity data, rate constant parameters can be estimated for any chosen compartmental model using nonlinear least squares iterative curve fitting strategies, such as the Levenberg-Marquardt algorithm [19, 20]. Equilibrium distribution volumes can then be derived from compartmental rate constants using basic relationships [21, 22]. For a one-tissue compartment model

$$V_T = \frac{K_1}{k_2} \quad (27)$$

For a two-tissue compartment model

$$V_T = \frac{K_1}{k_2} \left( 1 + \frac{k_3}{k_4} \right) \quad (28)$$

$$V_{ND} = \frac{K_1}{k_2} \quad (29)$$

Further, non-displaceable binding potential can be related to  $k_3$  and  $k_4$  using the equation [13]

$$BP_{ND} = \frac{k_3}{k_4} \quad (30)$$

While compartmental modeling with arterial blood sampling is generally considered the “gold standard” for quantitative PET imaging, it is costly and burdensome to patients, requiring long total scan times (~90 minutes) and arterial cannulation for blood draws. There are also many sources of error including noise in both the PET scan and arterial input function and the potential for patient movement during lengthy scans.

#### 1.1.4.3 Simplified Reference Tissue Model

Rather than drawing blood to generate an arterial input function, a brain region with a negligible concentration of target receptor or molecule can be used as a reference tissue. A reference tissue is a region in which there is no specific uptake of the radioligand and nonspecific binding is similar to that in target tissue. Reference tissue methods may introduce biases, especially when reference tissue requirements are not met, but they are less invasive, as they do not require arterial blood drawing.

A widely used reference tissue model is the simplified reference tissue model (SRTM) [23], shown in **Figure 5**. The rate of change of radiotracer concentration in the reference region ( $dC_{REF}/dt$ ) is given by

$$\frac{dC_{REF}(t)}{dt} = K'_1 C_P(t) - k'_2 C_{REF}(t) \quad (31)$$

in which  $K'_1$  is the rate constant for transfer from plasma to reference tissue, with units of mL/cm<sup>3</sup>/min, and  $k'_2$  is the rate constant for transfer from reference tissue to plasma with units of min<sup>-1</sup>. The rate of change of radiotracer concentration in the non-displaceable compartment in the target tissue is equivalent to that for the two-tissue compartment, **Equation 25**. The rate of change of specifically bound radiotracer concentration is given by **Equation 26**. By using the relationship between  $C_{REF}$  and  $C_P$  in **Equation 31**, a relationship can be made between  $C_T$  ( $C_{ND} + C_S$ ) and  $C_{REF}$  using six parameters:  $K_1$ ,  $K'_1$ ,  $k_2$ ,  $k'_2$ ,  $k_3$ , and  $k_4$ . Assuming that the volume of distribution for radiotracer that is not specifically bound in both the reference and target tissues are equivalent, i.e.

$$\frac{K'_1}{k'_2} = \frac{K_1}{k_2} \quad (32)$$

and substituting  $R_1$  for the ratio of  $K_1/K'_1$ , such that

$$k'_2 = \frac{k_2}{R_1}, \quad (33)$$

the relationship between  $C_T$  and  $C_{REF}$  can be described by four parameters:  $R_1$ ,  $k_2$ ,  $k_3$ , and  $BP_{ND} (k_3/k_4)$  [24].

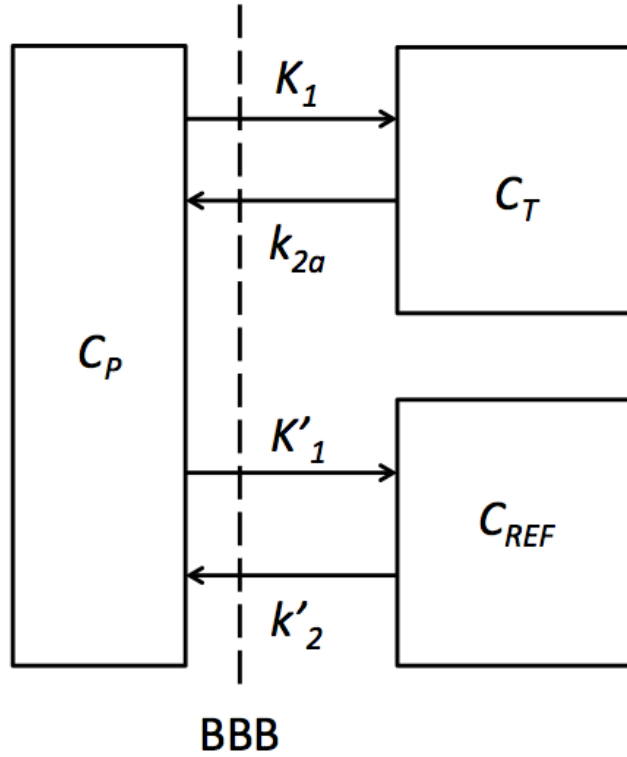


**Figure 5 Diagram of the Simplified Reference Tissue Model**, in which  $C_p$  is the concentration of radioligand in plasma,  $C_T$  is the concentration of radioligand in tissue, and  $C_{REF}$  is the concentration of radiotracer in the reference region.  $K_1$  is the rate in influx into the target tissue,  $k_{2a}$  is the overall rate from specifically bound to plasma,  $K'_1$  is the rate in influx into the reference tissue, and  $k'_2$  is the rate of efflux out of the reference tissue. The diagram is modeled after Normandin et al (2012) [1].



If the kinetics of non-displaceable and specifically bound radioligand cannot be distinguished, as described by a one-tissue compartment model, an overall rate constant for transfer from specifically bound to plasma,  $k_{2a}$ , can be used such that

$$\frac{dC_T(t)}{dt} = K_1 C_P(t) - k_{2a} C_T(t). \quad (34)$$

The total volume of distribution is then given by

$$V_T = \frac{K_1}{k_{2a}} = \left( \frac{K_1}{k_2} \right) (1 + BP_{ND}) \quad (35)$$

The three parameters  $R_1$ ,  $k_2$ , and  $BP_{ND}$  (**Equation 30**) can then be solved for using

$$C_T(t) = R_1 C_{REF}(t) + \left( k_2 - \frac{R_1 k_2}{(1 + BP_{ND})} \right) C_{REF}(t) - e^{-k_2 t / (1 + BP_{ND})} \quad (36)$$

As mentioned earlier the simplified reference tissue model is advantageous in that it does not require arterial blood sampling. A reference region devoid of specific binding can be sampled from the dynamic PET image and used as an input function. However, a full dynamic scan is still necessary to capture rapid changes in radioactivity concentration just after bolus injection of the radiotracer.

Further, two key assumptions of the simplified reference tissue method are (1) the kinetic behavior in both the reference and target tissues can be represented by a one-tissue compartment model, and (2) the reference and target tissues have the same non-displaceable volume of distribution (**Equation 32**). If these assumptions are not true of a radiotracer, the simplified reference tissue method will provide biased estimates of  $BP_{ND}$ . If either the target or the reference tissue is better represented by a two-tissue compartmental model, low  $BP_{ND}$ 's may be severely overestimated by SRTM [25]. If  $V_{ND}$  in the target region is greater than  $V_{ND}$  in the reference region,  $BP_{ND}$  may again be severely overestimated [25].

Wu and Carson (2002) [26] introduced a variation on the simplified reference tissue model in which  $k'_2$  is fixed across all target regions in a PET scan, with the reasoning that even though there are three parameters estimated in the SRTM model, there is only one reference region in the brain, so there should only be one  $k'_2$ . Substituting  $R_1 k'_2$  for  $k_2$  (from **Equation 32**) into **Equation 35** yields a model with parameters  $R_1$ ,  $k'_2$ , and  $BP_{ND}$ . For a given PET scan, all three parameters can be estimated separately for each region of interest. A global  $k'_2$  can then be calculated by averaging all regional  $k'_2$ . The  $k'_2$  parameter can then be fixed to this global value on a subsequent SRTM calculation, this time only fitting two parameters:  $R_1$  and  $BP_{ND}$ . This multi-step SRTM algorithm with fixed  $k'_2$  is referred to as SRTM2, and can potentially reduce noise in the calculation of  $R_1$  and  $BP_{ND}$  [26].

#### 1.1.4.4 Logan Graphical Analysis

Graphical analysis in PET quantitation refers to the reformulation of non-linear kinetic equations into linear form, such that the slope, derived simply through linear regression, represents volume of distribution. The Logan graphical method [27-29] is defined as the linear relationship:

$$\frac{\int_0^T C_T(t)}{C_T(t)} = V_T \frac{\int_0^T C_P(t)}{C_T(t)} + int \quad (37)$$

$V_T$  is given by the slope. Data in the Logan graphical analysis is typically regressed after a time  $t^*$ , when time dependence of the intercept is sufficiently small, i.e. when the relationship between  $\frac{\int_0^T C_T(t)}{C_T(t)}$  and  $\frac{\int_0^T C_P(t)}{C_T(t)}$  is linear.

The Logan graphical analysis can also be used with a reference region as input rather than plasma, such that the slope is the distribution volume ratio [28]:

$$\frac{\int_0^T C_T(t)}{C_T(t)} = DVR \frac{\int_0^T C_{REF}(t)}{C_T(t)} + int \quad (38)$$

An example reference Logan plot is show in **Figure 6**. Advantages of the Logan graphical method include computational simplicity and not requiring specification of the number of compartments. However, the reformulation of nonlinear kinetic equations into linear form may lead to biased results under certain circumstances [18].

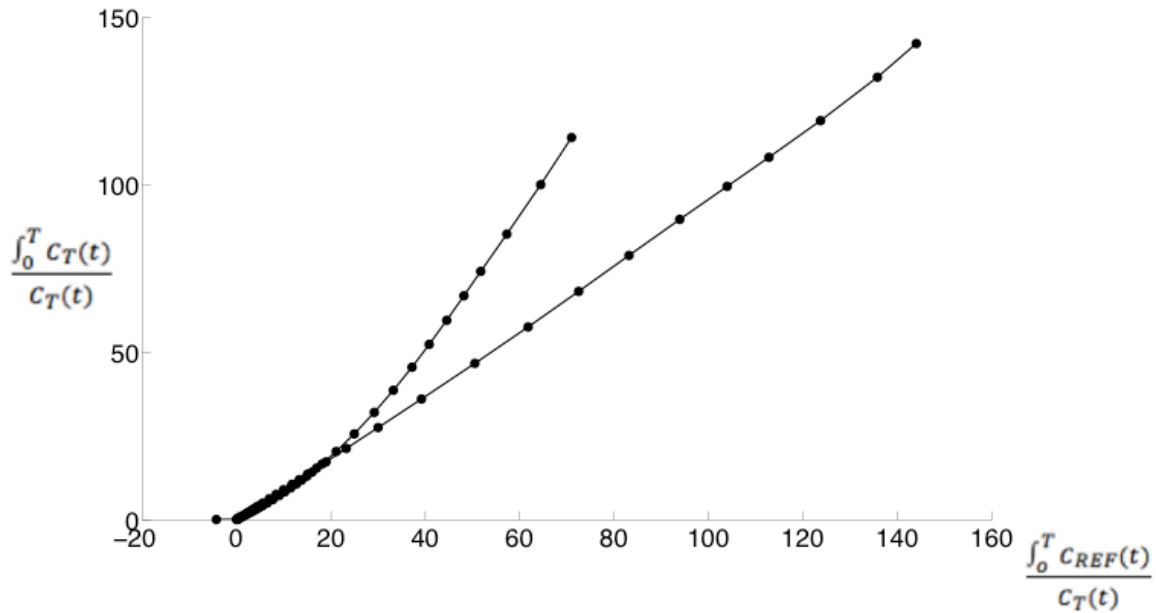


**Figure 6 Example of a Logan plot.** Data from two different subjects with differing slopes are shown. A steeper slope signifies a higher level of binding and higher DVR value.

#### 1.1.4.5 Standardized Uptake Value Ratio

One of the simplest methods for estimating how much radiotracer was delivered to a region of interest is the standardized uptake value (SUV), measured by multiplying the integral of activity over a short time frame by bodyweight and dividing by injected radiotracer activity [30]. SUV is typically calculated over a late-scan, short time frame (10-30 minutes), well after bolus injection of the radiotracer, when tissue uptake of radiotracer is assumed to be proportional to specific binding and independent of blood flow delivery effects.

Target region SUV can be normalized to a reference region SUV to obtain an estimate of DVR. This target-to-reference ratio is referred to as the standardized uptake value ratio (SUVR). The SUVR is typically calculated during a short, late-scan time when radiotracer is clearing from both the target region and the reference region at a similar rate, so that the ratio of the two is almost stable. This state is known as transient equilibrium, and typically corresponds to the washout phase after bolus injection, during which all radiotracer concentrations are decreasing [31, 32]. However, during this washout phase, the reference region concentration may decrease towards its equilibrium value relative to plasma concentration faster than the target region decreases. As such, the SUVR ratio may overestimate DVR calculated from compartmental modeling [31, 33]. Example time-activity data illustrating transient equilibrium is shown in **Figure 7**.

SUVR is typically related to DVR, as DVR is the ratio of target-tissue-to-plasma concentration ratio ( $V_T$ ) and non-displaceable-to-plasma concentration ratio

( $V_{ND}$ ), simplifying to  $C_T/C_{ND}$ . Therefore, when comparing SUVR outcome measures to  $BP_{ND}$ , a measure of SUVR-1 is typically used.

Despite potential bias, SUVR remains a popular method for estimating radiotracer binding given its computational simplicity and short necessary scanning times. The SUVR method does not require an arterial blood draw, and only requires PET scanning during the 20-30 minute transient equilibrium period, making it more cost effective than other methods and less burdensome to patients and research subjects.

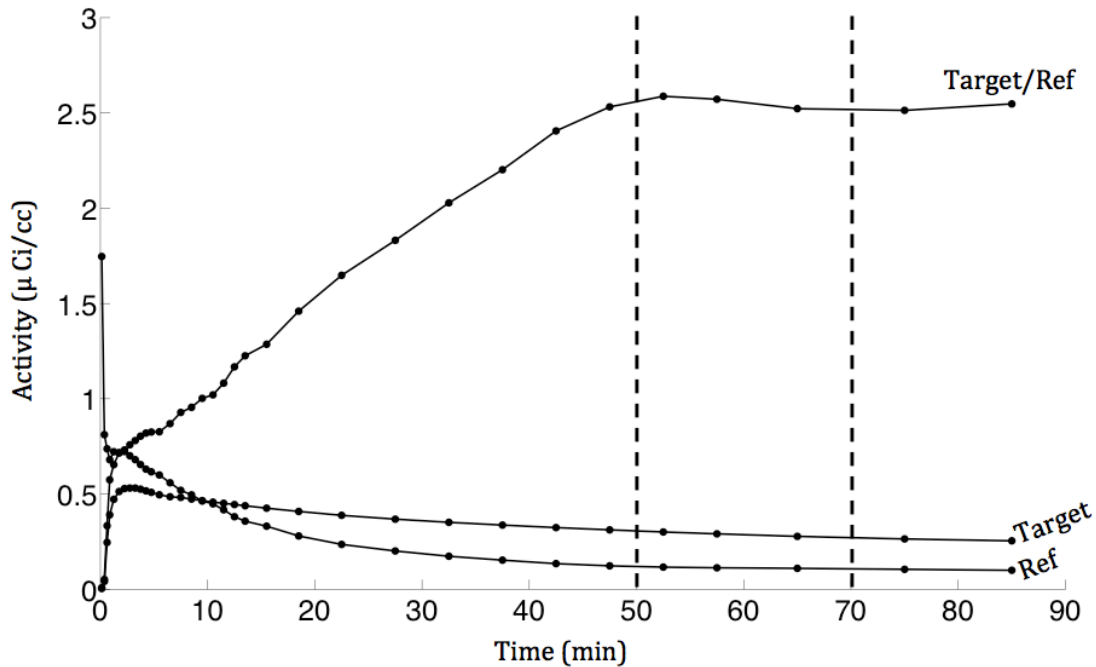


**Figure 7 Illustration of Target and Reference (Ref) time-activity data.** At ~50 minutes post-injection, radiotracer in both the target and reference tissue start to clear at approximately the same rate, yielding a constant ratio. SUVR is typically calculated during this phase, which is referred to as transient equilibrium.

### **1.1.5 Neurological Characteristics of Alzheimer's Disease**

Clinically, Alzheimer's disease (AD) is characterized by memory loss, which is often manifest by repetitive speech, losing personal objects, getting lost in familiar places, and not recognizing friends and family [34]. Neuropathologically, AD is characterized by the loss of cells and synapses and gross atrophy in the temporal lobe, parietal lobe, frontal cortex, and cingulate gyrus, and the presence of amyloid plaques and neurofibrillary tangles [35]. Amyloid plaques are dense, mostly insoluble deposits of 40-42 amino acid amyloid-beta ( $A\beta$ ) peptides [36]. Neurofibrillary tangles (NFT) are mainly a hyperphosphorylated form of the microtubule-associated protein, tau [37]. Plaques occur earliest in the neocortex where they are relatively evenly distributed [38]. Tangles appear first in the transentorhinal and entorhinal cortices and progress in a predictable pattern to the neocortex [39]. Compared to NFT, neuritic plaques are generally more evenly distributed over the cortex, with the exceptions of notably fewer neuritic plaques in limbic periallocortex and allocortex, which have the greatest NFT density [40]. Price and Morris [41] found little amyloid pathology in the hippocampus of amyloid-positive controls and very mild AD patients. The cerebellum is relatively free of neuritic plaques in AD, although less dense diffuse amyloid deposits are commonly observed [42].

Jack et al (2010) [43] put forth a hypothetical model of the major biomarkers of Alzheimer's disease based on various imaging, biofluid, and autopsy studies, that continues to be validated and refined. The current model [44] asserts amyloid deposition occurs well before cognitive symptoms of AD, which is supported by

amyloid deposits having been found in elderly cognitively normal controls in frontal and temporal cortices at autopsy [45]. The hypothetical model asserts A $\beta$  deposition is followed by tau-mediated neuronal injury and dysfunction, then structural atrophy and ventricular expansion, and finally cognitive impairment.

Mild cognitive impairment (MCI) is an intermediate stage of cognitive decline closely related to AD. It is characterized either by isolated memory impairment or impairment in multiple cognitive domains, but is not severe enough to warrant a diagnosis of AD [45-47]. Approximately half of MCI patients progress to AD at a rate of 10-15%, whereas half do not develop AD even after follow-up periods as long as ten years [48-50].

#### **1.1.6 Amyloid Beta Plaque Imaging**

Due to A $\beta$  plaque's role as a hallmark and early indicator of AD, a number of PET radiotracers have been developed that target the protein in order to assess amyloid load in vivo. One of the first successful A $\beta$ -plaque PET imaging studies of a living human subject diagnosed with probably AD was conducted just over ten years ago using  $^{11}\text{C}$ -radiolabeled Pittsburgh Compound B (PiB) [51, 52]. Other A $\beta$  plaque radiotracers developed since then include  $^{18}\text{F}$ -florbetapir [53],  $^{18}\text{F}$ -flutemetamol [54],  $^{18}\text{F}$ -florbetaben [55], and  $^{18}\text{F}$ -AZD4694 [56]. All express a high affinity for A $\beta$  in grey matter, with high nonspecific binding in white matter. Example PiB PET images of a healthy control subject and an Alzheimer's disease patient are presented in **Figure 8**. Development of  $^{18}\text{F}$  amyloid-specific radiotracers has been particularly important to the study of Alzheimer's disease, as the

radionuclide's longer half-life, relative to  $^{11}\text{C}$ , has allowed for widespread manufacture and distribution of amyloid-specific radiotracers.

A number of longitudinal studies are ongoing to better define normal aging and the progressive neurodegeneration that accompanies Alzheimer's disease using these amyloid PET ligands;  $^{18}\text{F}$ -Fluorodeoxyglucose (FDG) to assess glucose metabolism; and measures of cortical atrophy, hippocampal atrophy, and ventricular volume based on structural MR images. Forster et al (2012) [57], in a study of 20 individuals with mild AD, concluded that by the time patients became demented, amyloid deposition was static whereas hypometabolism measured by FDG continued to progress. In a study of 897 individuals, baseline-adjusted amyloid PET showed evidence of reaching a plateau as a clinical measure of cognition worsened, suggesting a sigmoid shape in the time-course trajectory of amyloid deposition [58]. The same group modeled the temporal trajectory of amyloid PET measures over time in 260 individuals spanning the cognitive continuum and reported a sigmoidal relationship between amyloid load and time [59]. The Australian Imaging, Biomarkers, and Lifestyle study also reported a sigmoidal relationship between amyloid load and time based on 200 individuals spanning the cognitive continuum [60].  $\text{A}\beta$  deposition seems to be protracted, likely lasting over twenty years before plateauing. Cognitive decline seems to occur well after substantial  $\text{A}\beta$  deposition, and continues to worsen in late AD even after  $\text{A}\beta$  deposition plateaus. As such,  $\text{A}\beta$  deposition has been measured in elderly subjects across the cognitive spectrum, including cognitively normal controls and mild-cognitive impairment patients.  $\text{A}\beta$  deposition is found in 10-30% of cognitively



normal elderly, and the prognosis for contracting Alzheimer's disease is worse for those with A $\beta$  deposition than those without [61].

<sup>18</sup>F-Florbetapir (Amyvid), <sup>18</sup>F-Flutemetamol (Vizamyl), and <sup>18</sup>F-florbetaben (Neuraceq) have all been FDA approved for human clinical A $\beta$  imaging to rule out probable Alzheimer's disease, and appropriate use criteria for amyloid PET in the clinic continues to be discussed [62-64]. In the clinic these agents will likely prove useful in identifying anti-amyloid therapies that can prevent or delay Alzheimer's disease and identify subjects who will likely benefit from such therapies long before the cognitive symptoms of Alzheimer's disease manifest. However, postmortem assessment of amyloid and tau burden remains the definitive diagnosis of Alzheimer's disease [35]. The agreement between amyloid PET imaging and postmortem measures of neuropathology is an ongoing area of investigation [65, 66].

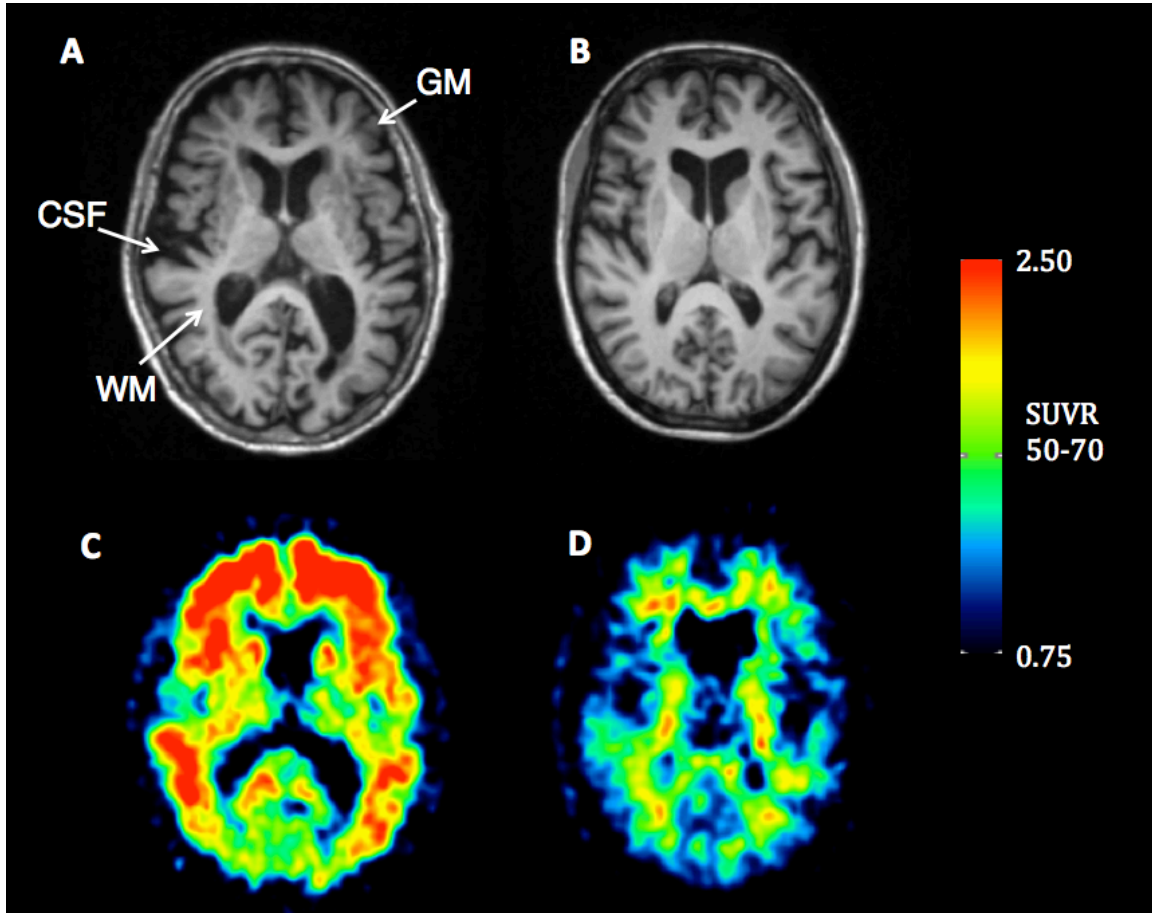


**Figure 8** Axial slices of MR and PiB PET images for a PiB-positive (PiB(+)) Alzheimer's disease subject and a PiB-negative (PiB(-)) cognitively normal control subject. Cortical atrophy and ventricular expansion are apparent in the Alzheimer's disease subject MR image (A), relative to the normal control subject MR image (B). High PiB retention is apparent in frontal, temporal, and precuneus cortical regions in the Alzheimer's disease subject PiB SUVR image (C). Higher signal is seen in white matter areas than cortical grey matter regions in the normal control subject PiB image (D) due to non-specific binding of PiB to white matter and little to no specific binding in cortical grey matter. GM, WM, and CSF voxels are pointed out in the Alzheimer's disease subject MR image (A).

## 1.2 Overview of Dissertation Work

The first part of this thesis work (Chapter 2) describes the implementation of multiple partial volume correction techniques with existing and developed software. The generation of five simulated phantom PiB PET images based on existing PiB PET data is also described. The performance of three partial volume correction methods – the Meltzer, the Müller-Gärtner, and the Region-Based Voxel-Wise techniques – was then characterized and compared based on the simulated phantom images.

The second part of this thesis work (Chapter 3) examines the impact of the three PET partial volume correction methods on the correlation between region-matched antemortem PiB PET SUVR and postmortem measures of amyloid load in a unique cohort of 12 subjects. Characterizing the relationship between antemortem amyloid PET imaging and postmortem measures of amyloid load will improve understanding of the natural history of Alzheimer’s disease, facilitate more accurate diagnoses of dementia, and aid in the validation of prevention and treatment measures for Alzheimer’s disease. The performance of these partial volume correction techniques is further characterized by examining the noise magnification properties for each, and an optimal partial volume correction technique is identified.

Novel aspects of the second part of this thesis work include the application of multiple partial volume correction techniques in a study correlating antemortem PiB PET data to postmortem measures of amyloid load (**Sections 3.2.6, 3.4.2**), and the assessment of noise magnification for multiple partial volume correction techniques both within brain tissue regions and CSF spaces (**Sections 3.2.7, 3.3.2**). Implementation of the Region-Based Voxel-Wise method in this study incorporates

both automatically generated and hand-drawn regions of interest (**Section 3.2.6**), whereas previous studies of the Region-Based Voxel-Wise method only utilized automated regions of interest [11]. This work also includes the largest sample size to date for a region-matched antemortem-to-postmortem correlation study of amyloid load.

The third part of this thesis work (Chapter 4) examines the relative performance of five different reference-tissue PET analysis methods for measuring change in amyloid deposition over time. PiB PET imaging studies are typically performed on an elderly, possibly demented population. To reduce the burden on study subjects and improve study feasibility, simplified reference tissue methods are typically used to quantify amyloid deposition. However, each of these methods has different inherent biases, which may confound natural history studies of Alzheimer's disease or amyloidosis treatment trials. The SRTM2, reference Logan, and three SUVR time-frames are applied to a unique cohort of 48 healthy control, MCI, and AD subjects, all with full-dynamic 90-minute PiB PET scans at baseline and follow-up. The potential impact of reference region selection, changes in relative radiotracer delivery between target and reference tissues, and the partial volume effect are examined, though partial volume correction techniques are not utilized. An optimal reference tissue method is eventually selected based on known biases in the different methods and measured group changes.

Novel aspects of the third part of this thesis work include smoothing of full dynamic PiB PET time-activity data to reduce the effect of noise on outcome measures (**Sections 4.2.5, 4.4.2**) and population trajectory modeling of multiple

outcome measures (**Section 4.2.8**). The influence of changes in non-specific binding in white matter on measured changes of amyloid burden in PiB PET data (**Section 4.3.3, 4.4.2**) had not been adequately examined prior to this work. Finally, this work includes the selection of a best performing reference tissue method for PiB PET based on the ability to distinguish change between groups that are stable and groups that are increasing in amyloid load.

# Chapter 2

## Implementation and Characterization of PVC Techniques

Three different PVC techniques were implemented as part of this thesis work using a combination of existing medical image analysis software packages, Bash shell scripting, and Matlab programming. This section describes the software packages utilized; the routines developed for the implementation of the Meltzer, MMG, and RBV partial volume correction techniques; and the validation and characterization of these PVC techniques through the use of simulated PiB PET phantom images.

### 2.1 Existing Software Used in This Work

#### 2.1.1 FreeSurfer

FreeSurfer software (<https://surfer.nmr.mgh.harvard.edu/fswiki>; Martinos Center for Biomedical Imaging, Harvard, MA, USA) [67, 68] was used as part of this thesis work to perform anatomical segmentation and parcellation on MR images. In this thesis, MR image “segmentation” refers to the partitioning or labeling of voxels according to brain tissue types, such as grey matter, white matter, and CSF. “Parcellation” refers to a finer level of partitioning according to anatomical regions defined by specific sulci and gyri, such as superior parietal grey matter.

Briefly, the fully automated FreeSurfer processing pipeline of a brain MR image includes removal of non-brain tissue using a hybrid watershed/surface deformation procedure [69] followed by segmentation of subcortical white matter

and subcortical grey matter structures [67, 68]. GM-WM and GM-CSF boundaries are defined by identifying locations of greatest shift in intensity [70]. Surface inflation and registration of the GM-CSF border to a spherical atlas is then performed [71, 72] in order to parcellate the cerebral cortex according to gyral and sulcal structures [68]. The entire fully automated FreeSurfer parcellation stream can take up to 24 hours to complete for a single MR image, depending on computer hardware. **Figure 9** shows an example MR image with FreeSurfer-parcellated regions overlaid.

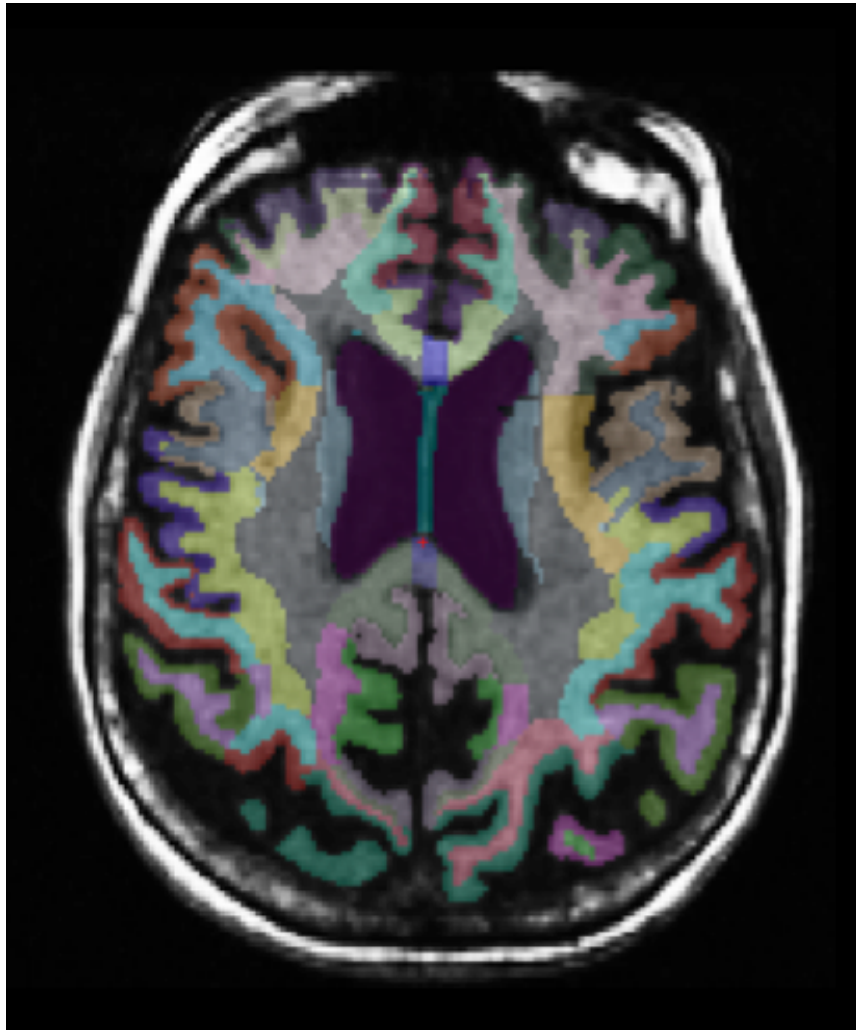


**Figure 9 Axial slice of an MR image with FreeSurfer parcellation regions overlaid.** Each color signifies a different FreeSurfer parcellation region. Cortical GM regions are parcellated according to sulci and gyri boundaries. Neighboring WM spaces are subsequently parcellated according to the cortical GM parcellation definitions.



### 2.1.2 The FMRIB Software Library

The FMRIB Software Library (FSL) v5.0.8 (<http://fsl.fmrib.ox.ac.uk/fsl/fslwiki/>; FMRIB, Oxford University, UK) [73] was used to perform basic mathematical operations on MR and PET images, and to sample images using binary regions of interest. FSL is a library for the analysis of functional MR image data, but only the “fslmaths” and “fslstats” utilities were used in this thesis work. The fslmaths utility allows for voxel-wise arithmetic manipulation of images, such as subtracting or dividing one image from another. The fslstats utility reports certain voxel-wise statistics for images, such as mean, standard deviation, and range. The fslstats utility also allows for input of a binary image mask so that summary statistics are only calculated on voxels within the mask. Images were sampled with regions of interest using this feature.

### 2.1.3 Statistical Parametric Mapping

The Statistical Parametric Mapping version 8 (SPM8) software package (<http://www.fil.ion.ucl.ac.uk/spm/>; Wellcome Trust Centre for Neuroimaging, Institute of Neurology, University College London, UK) is a library of MATLAB (The MathWorks, Inc., Natick, Massachusetts, United States) functions and compiled C routines for the interpretation of functional neuroimaging data. In this work, SPM8 was used for smoothing or convolving images with a Gaussian kernel of a specified full-width at half maximum with the native “Smooth” function. SPM8 was also used to coregister PET and MR images. The “Coregister” function in SPM8 calculates a rigid-body transformation in three dimensions between two images using Powell’s

optimization algorithm [74] to find the local minimum of the normalized mutual information cost function [75].

## **2.2 Implementation of Partial Volume Correction Techniques**

### **2.2.1 Meltzer Method Implementation**

Given a quantitative PET image and a whole-brain tissue binary mask image, a voxel-level Meltzer-corrected PET image was generated in two basic steps. The first step was smoothing the whole-brain tissue binary mask according to the scanner PSF using the “Smooth” function in SPM8 software. The second step was then dividing the quantitative PET image by the smoothed whole-brain tissue mask using the “fslmaths” utility in FSL, which resulted in a Meltzer-corrected quantitative PET image.

### **2.2.2 Modified- Müller-Gärtner (MMG) Implementation**

As described in **Section 1.1.3.4**, a preprocessing step for the MMG PVC method is application of the GTM PVC method to obtain a partial volume-corrected subcortical white matter value. The GTM method was implemented as a MATLAB function, `sample_gtm.m`. This function has three inputs: a string of the name of a PET image, a cell array of strings of binary parcellation region masks, and a cell array of strings of corresponding smoothed parcellation region masks. The function then reads and loads image data using SPM8 functions, samples the PET image using all binary parcellation masks, creates the actual geometric transform matrix as described in **Section 1.1.3.3**, and calculates partial volume-correction regional PET

values. The GTM function also has three outputs: the full geometric transform matrix, uncorrected regional PET values, and partial volume-corrected regional PET values; and generates a text file containing regional uncorrected and partial-volume corrected values.

Upon completion of the initial GTM preprocessing step, a voxel-level MMG-corrected PET image was generated in four steps. The first step was smoothing both the FreeSurfer-derived grey matter binary mask and the FreeSurfer-derived white matter binary mask according to the scanner PSF using the “Smooth” function in SPM8 software. In the second step, the smoothed white matter tissue mask was multiplied by the partial volume-corrected subcortical white matter value, calculated in the initial GTM preprocessing, using the “fslmaths” utility. This generated an image containing the contribution of signal from white matter on a voxel basis. In the third step, this white matter-contribution image was subtracted from the original PET image. Finally, the fourth step involved dividing the white matter-subtracted PET image by the smoothed grey matter map, producing a MMG partial volume-corrected PET image.

### **2.2.3 Region-Based Voxel-Wise (RBV) Implementation**

As in the case of the MMG PVC method, the RBV PVC method begins with application of the GTM method with the PET image, binary parcellation region masks, and smoothed parcellation region masks. Following completion of the GTM step, an RBV partial volume-corrected image was created in four general steps. First, all of the binary parcellation region masks were individually multiplied by

their respective GTM-corrected PET values using the “fslmaths” utility. The second step was summing all GTM-corrected PET value parcellation masks (**Equation 12**), again using the “fslmaths” utility. As the parcellation masks are non-overlapping and span the entire brain, this second step generates a “synthetic” PET image free of partial volume errors [11]. The third step was smoothing the synthetic PET image according to the scanner PSF using the “Smooth” function in SPM8 software. Finally, an RBV-corrected PET image was created by multiplying the original PET image by the voxel-wise ratio of the synthetic PET image and the smoothed synthetic PET image (**Equation 13**).

## **2.3 Validation and Characterization Using Simulated Phantoms**

### **2.3.1 Introduction**

To validate the implementation and characterize the performance of the Meltzer, MMG, and RBV PVC methods, five simulated phantom SUV PET images with known true values were created based on MR and PET images previously acquired from two subjects, one high-PiB-binding subject and one low-PiB-binding subject. High-PiB-binding in this validation study refers to having a greater level of specific PiB binding in cortical GM than non-specific binding in subcortical WM. Low-PiB-binding refers to having a lower level of specific PiB binding in cortical GM than non-specific binding in subcortical WM. Each of the implemented PVC methods were then applied to the anatomically correct phantom PET images to determine if signal loss due to partial volume errors was appropriately recovered.

## **2.3.2 Materials and Methods**

### **2.3.2.1 Subjects**

The two subjects used in phantom PET image generation were recruited prior to this thesis work as part of University of Pittsburgh Alzheimer Disease Research Center (ADRC) research studies. Image data from these two subjects were used in this thesis work with permission from Dr. William Klunk, Co-Director of the ADRC. The high-PiB-binding subject (female; age 79 at time of PiB PET scan) received an extensive neuropsychiatric evaluation at the ADRC, and a diagnosis of Probable AD at a consensus conference attended by clinical staff, neurologists, psychiatrists, and neuropsychiatrists. The low-PiB-binding subject (female; age 80 at time of PiB PET scan) also underwent full evaluation at the ADRC, scored normally on evaluations, and was classified as cognitively normal.

### **2.3.2.2 MR and PiB PET Imaging**

Both the high- and low-PiB-binding subject underwent MR and PiB PET imaging prior to this thesis work. MR images were acquired on a 1.5T GE Signa scanner at the University of Pittsburgh MR Research Center. The scan protocol included a T1-weighted volumetric spoiled gradient recalled (SPGR) sequence in the coronal plane (TE/TR = 5/25, flip angle = 40°, NEX = 1, slice thickness = 1.5mm).

PiB PET images were acquired on a Siemens/CTI ECAT HR+ scanner in 3D imaging mode, yielding 63 parallel transaxial planes over a 15.2 cm axial FOV. The high-PiB-binding subject was administered 15.2 mCi of PiB and scanned for 90 minutes immediately after injection (34 frames: 4 × 15 sec, 8 × 30 sec, 9 × 60 sec, 2 ×

180 sec, 8 × 300 sec, 3 × 600 sec). The low-PiB-binding subject was administered 15.8 mCi of PiB and scanned for 30 minutes, over a 40-70 minute time period post-injection (6 frames: 6 × 300 sec). Data was reconstructed with filtered back-projection reconstruction (Fourier rebinning/2D back-projection) and PET data correction included scanner normalization, dead-time, attenuation, scatter, and radioactive decay. The final reconstructed image resolution, or PSF, was  $6.46 \times 6.09 \times 5.71$  mm FWHM.

#### **2.3.2.3 Simulated Phantom Image Generation**

SUV 50-70 min PET images were generated for both subjects by averaging 50-70 minute post-injection time frames and multiplying the resulting static PET image by the subject-specific ratio of bodyweight and injected dose, as described in **Section 1.1.4.5**. The SUV PET images were then coregistered to their respective MR images using the “Coregister” function in SPM8. Coregistered SUV PET and MR images for both the high-PiB-binding and low-PiB-binding subjects are shown in **Figure 10**.

The two MR images were then parcellated using FreeSurfer software. FreeSurfer segmentation and parcellation maps were visually inspected and manually edited using the FreeSurfer tool “tkmedit” to ensure GM, WM, CSF, and within-tissue anatomical boundaries were properly followed. Eighty-four parcellations were converted to binary masks from the “aparc+aseg” FreeSurfer parcellation map using the “mri\_convert” tool within FreeSurfer and “fslmaths” utility within FSL. These 84 contiguous, non-overlapping binary masks spanned the

entire brain and consisted of all available lateralized cortical and subcortical GM regions, a whole cerebral WM region, a whole cerebellar GM region, a cerebellar WM region, and the brainstem. The binary masks were combined to create full GM and full WM tissue masks, both of which, in turn, were combined to create a whole-brain tissue mask.

The geometric transform matrix (GTM) partial volume-corrected data for the high-PiB-binding and low-PiB-binding subjects were subsequently used to generate five phantom images with varying distributions. **Phantom A** was assigned a constant SUV value throughout all brain tissue voxels using the high-PiB-binding whole-brain tissue mask. Phantom A does not represent a realistic distribution of radioactivity concentration for a PiB PET scan. However, it is an ideal case for the Meltzer PVC method because the Meltzer method does not correct for partial volume effects (PVEs) within brain tissue, only PVEs due to signal lost to CSF space. With homogeneous activity throughout brain tissue, Phantom A should only be affected by PVEs resulting from signal lost to CSF space. **Phantom B**, which represented the ideal case for MMG PVC, was assigned a constant SUV value in WM voxels and a higher constant SUV value in GM voxels according to GTM-corrected values and segmentation masks from the high-PiB-binding subject. **Phantom C** was assigned a constant SUV value in WM voxels and lower constant SUV value in GM voxels according to the low-PiB-binding subject. **Phantom D**, which represented the ideal case for RBV PVC, was assigned a constant SUV value in WM voxels and varying SUV values for all cortical and subcortical GM regions according to GTM-values and parcellation masks from the high-PiB-binding subject. **Phantom E** was

assigned a constant SUV value in WM voxels and varying SUV values for all cortical and subcortical GM regions according to the low-PiB-binding subject. Each of the phantom images was subsequently blurred by the PET scanner PSF ( $6.46 \times 6.09 \times 5.71$  mm) using the “Smooth” function in SPM8. Images for all five phantoms are shown in **Figure 11**.

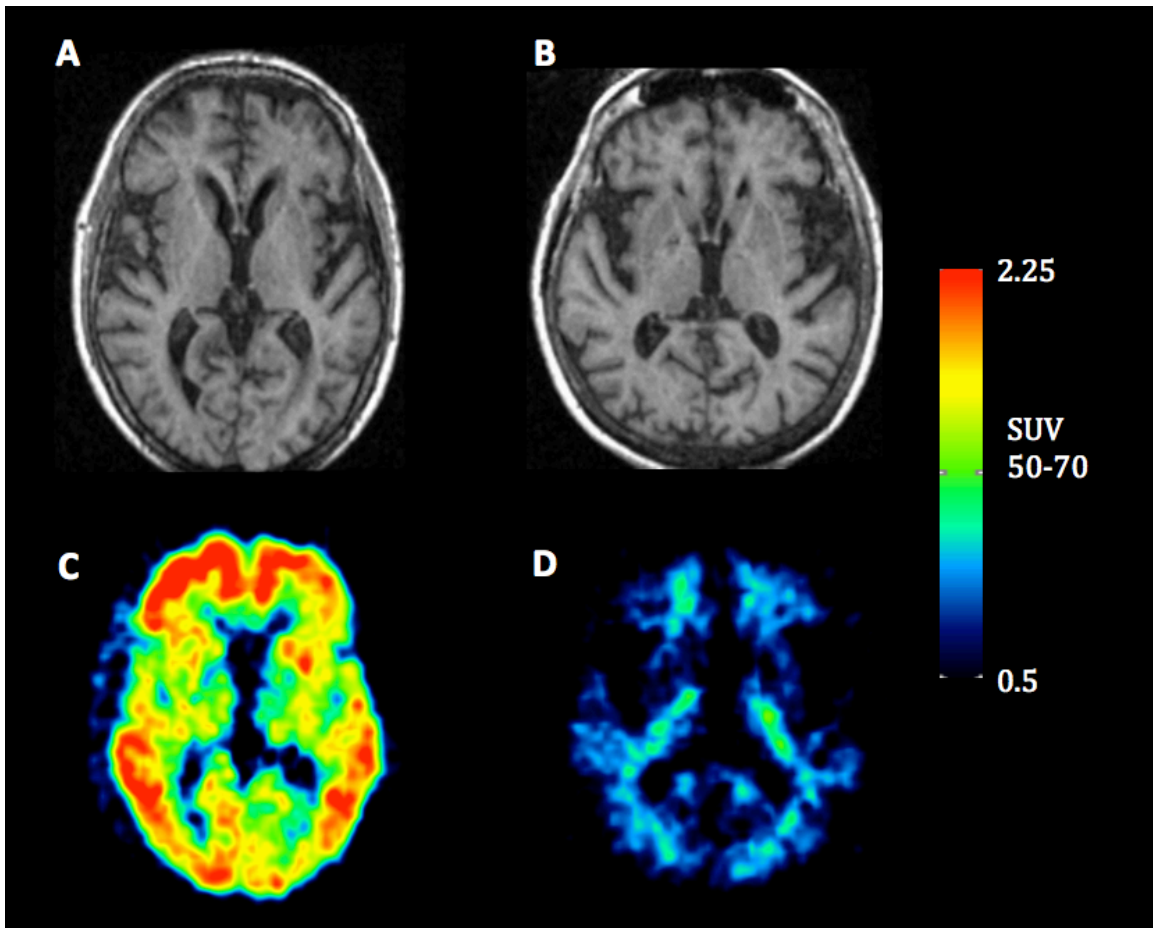


**Figure 10 MR and SUV PiB PET images for the low-PiB-binding and the high-PiB-binding subjects.** The high-PiB-binding SUV PET image (C) is coregistered to its respective MR (A), and the low-PiB-binding SUV PET image (D) is coregistered to its respective MR (B). FreeSurfer parcellations resulting from the MR images were used in producing GTM partial volume corrected data. FreeSurfer parcellations and GTM-corrected data were subsequently used to generate five phantom images for the validation of PVC method implementations.



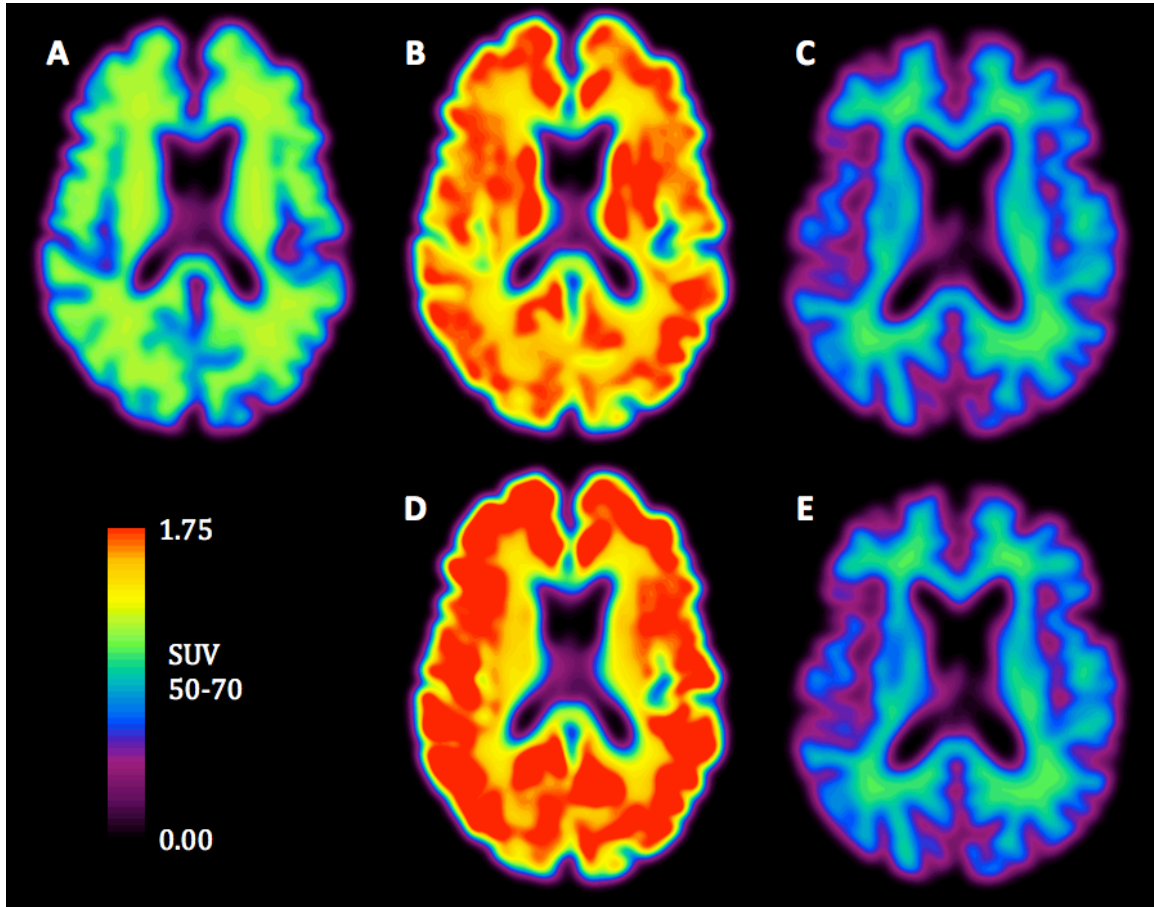


**Figure 11 Axial slices of phantom images after smoothing for validating the implementation of Meltzer, MMG, and RBV partial volume correction methods.** Phantom A (A) represents the ideal case for Meltzer PVC with a constant SUV value over all brain tissue voxels. Phantom B (B) represents an ideal case for MMG PVC with two different constant values assigned to GM and WM voxels according to the high-PiB-binding subject (constant GM SUV > constant WM SUV). Phantom C (C) also represents an ideal case for MMG PVC with two different constant values assigned to GM and WM voxels according to the low-PiB-binding subject (constant GM SUV < constant WM SUV). Phantom D (D) represents an ideal case for RBV PVC with different values assigned to each GM region according to the high-PiB-binding subject (variable GM SUV > constant WM SUV). Phantom E (E) represents another ideal case for RBV PVC with different values assigned to each GM region according to the low-PiB-binding subjects (variable GM SUV < constant WM SUV).

#### 2.3.2.4 Phantom-Based Evaluation

The Meltzer, MMG, and RBV PVC methods were all applied to each phantom image. Lateralized cortical and subcortical region (e.g. left precuneus and right precuneus) SUV values were averaged to generate whole region SUV values. These regions included the anterior cingulate, middle frontal, lateral occipital, middle temporal, posterior cingulate, precuneus, and superior parietal cortical regions, in addition to the caudate, putamen, and thalamus subcortical regions.

The recovery coefficient (RC; defined in **Section 1.1.2**), which in this validation study is the ratio of observed SUV to true SUV, was calculated for all cortical and subcortical GM regions across phantoms and PVC methods. A RC of 1.0 for partial volume-corrected data signifies full recovery of activity lost to partial volume errors and validation of the PVC implementation. A RC of 1.0 was expected for Meltzer-corrected data for Phantom A, MMG-corrected data for Phantoms B and C, and RBV-corrected data for Phantoms D and E. An RC greater than 1.0 for partial volume-corrected data signifies overestimation of radioactivity concentration, and an RC less than 1.0 signifies underestimation of radioactivity concentration.

#### 2.3.3 Results

Average and standard deviation SUV voxel values within the superior parietal region are presented in **Table 3**. Average recovery coefficients over all cortical and subcortical GM regions according to phantom and PVC method are presented in **Table 4**.

**Phantom A.** **Figure 12** shows true, uncorrected, and partial volume corrected SUV values for Phantom A across multiple GM cortical and subcortical regions for the PVC methods tested. The RC values for uncorrected data ranged from 0.66 in the superior parietal region to 0.98 in the putamen, with an average RC across cortical and subcortical GM regions of  $0.76 \pm 0.10$ . All PVC methods achieve an exact recovery coefficient of 1.0 across all regions for Phantom A.

**Phantom B.** **Figure 13** shows SUV values with and without PVC for Phantom B, the high-PiB-binding constant GM activity phantom. RC values for uncorrected data ranged from 0.52 in the superior parietal to 0.83 in the putamen and an average RC of  $0.63 \pm 0.10$ . Application of the Meltzer method also resulted in underestimated SUV values across all regions with RC values ranging from 0.79 to 0.92 with an average RC of  $0.84 \pm 0.04$ . Application of the MMG and RBV methods resulted in exact recovery of activity, with RC values of 1.0 across all regions.

**Phantom C.** Uncorrected and partial volume-corrected cortical and subcortical GM SUV values for Phantom C, the low-PiB-binding constant-GM activity phantom, are shown in **Figure 14**. RC values for uncorrected data were less than 1.0 across all regions except the putamen, which had an RC of 1.14. Application of the Meltzer PVC method resulted in overestimation of true SUV values across all cortical and subcortical regions with an average RC of  $1.20 \pm 0.05$ . As in the case of Phantom B, application of the MMG and RBV methods resulted in exact recovery of activity.

**Phantom D.** In the case of Phantom D, the high-PiB-binding variable-GM activity phantom, uncorrected data underestimated true activity with RC values

ranging from 0.48 in the superior parietal region to 0.90 in the putamen (**Figure 15**). Application of the Meltzer method still results in underestimated data with RC values ranging from 0.73 in the superior parietal to 0.99 in the thalamus. Application of the MMG PVC method results in relatively close-to-exact recovery of activity with RC values ranging from 0.97 in the precuneus to 1.02 in the anterior cingulate with an average of  $1.01 \pm 0.02$  across cortical and subcortical GM regions. However, only application of the RBV method resulted in exact recovery of SUV values across all cortical and subcortical regions in this variable-GM activity phantom.

**Phantom E.** Finally, in the case of Phantom E, the low-PiB-binding variable-GM activity phantom, uncorrected data underestimated true activity across all regions except for the putamen, which was overestimated, as in the case of Phantom C (**Figure 16**). Application of the Meltzer PVC method resulted in overestimation of true SUV values across all regions with an average RC of  $1.21 \pm 0.09$ . As in the case of Phantom D, application of the MMG method to Phantom E resulted in relatively close-to-exact recovery of SUV values with RC values ranging from 0.94 to 1.07. However, again, only application of the RBV method resulted in exact recovery of SUV values across all regions in this variable-GM activity phantom.

**Table 3** Superior parietal SUV values and standard deviations according to phantom and PVC method.

	No PVC	Meltzer	MMG	RBV
Phantom A	$0.81 \pm 0.20$	$1.22 \pm 0.00$	$1.22 \pm 0.00$	$1.22 \pm 0.00$
Phantom B	$1.34 \pm 0.26$	$2.06 \pm 0.15$	$2.59 \pm 0.00$	$2.59 \pm 0.00$
Phantom C	$0.57 \pm 0.17$	$0.85 \pm 0.05$	$0.68 \pm 0.00$	$0.68 \pm 0.00$
Phantom D	$1.59 \pm 0.29$	$2.46 \pm 0.26$	$3.33 \pm 0.07$	$3.35 \pm 0.00$
Phantom E	$0.57 \pm 0.17$	$0.85 \pm 0.05$	$0.68 \pm 0.02$	$0.68 \pm 0.00$

**Table 4** Average recovery coefficients according to phantom and PVC method across all cortical and subcortical grey matter regions.

	No PVC	Meltzer	MMG	RBV
Phantom A	$0.76 \pm 0.10$	$1.00 \pm 0.00^*$	$1.00 \pm 0.00^*$	$1.00 \pm 0.00^*$
Phantom B	$0.63 \pm 0.10$	$0.84 \pm 0.04$	$1.00 \pm 0.00^*$	$1.00 \pm 0.00^*$
Phantom C	$0.92 \pm 0.09$	$1.20 \pm 0.05$	$1.00 \pm 0.00^*$	$1.00 \pm 0.00^*$
Phantom D	$0.64 \pm 0.14$	$0.84 \pm 0.09$	$1.01 \pm 0.02$	$1.00 \pm 0.00^*$
Phantom E	$0.93 \pm 0.15$	$1.21 \pm 0.09$	$1.00 \pm 0.03$	$1.00 \pm 0.00^*$

\* Exact recovery of activity achieved by PVC method

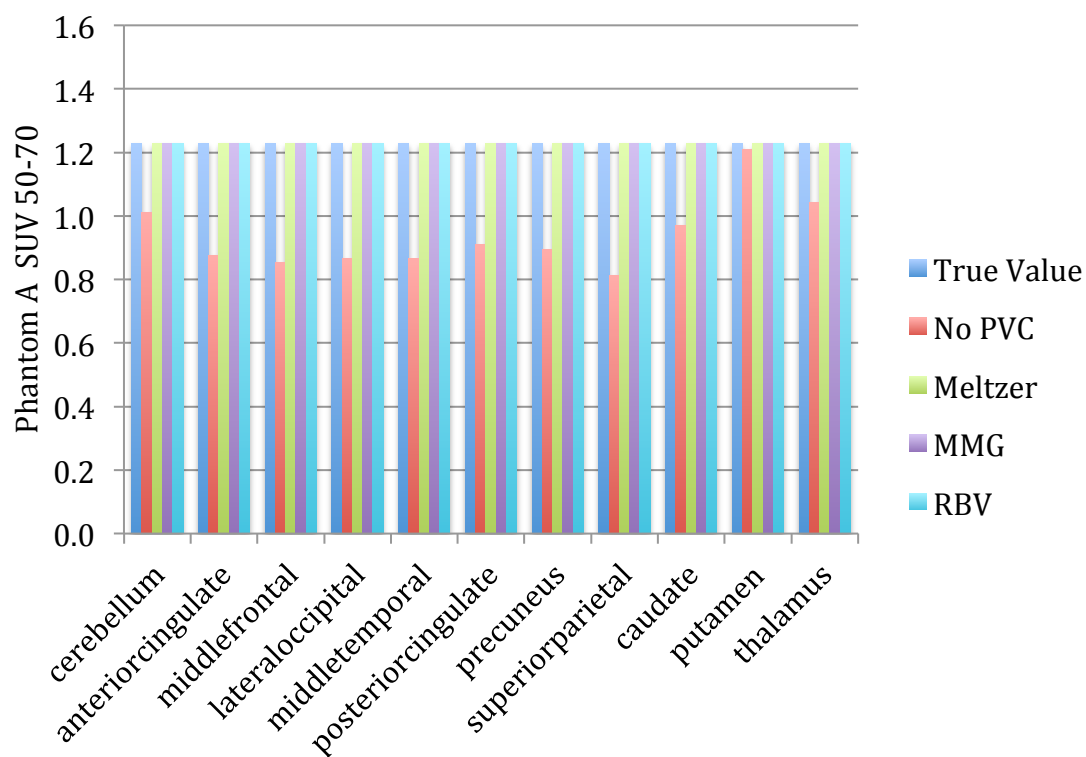


**Figure 12 Phantom A uncorrected and partial volume-corrected regional SUV 50-70 minute values.** Phantom A was assigned a constant SUV value throughout all brain tissue. Uncorrected SUV values underestimate true activity with RC values ranging from 0.66 in the superior parietal region to 0.98 in the putamen. All partial volume correction methods fully recover activity in all cortical and subcortical GM regions.

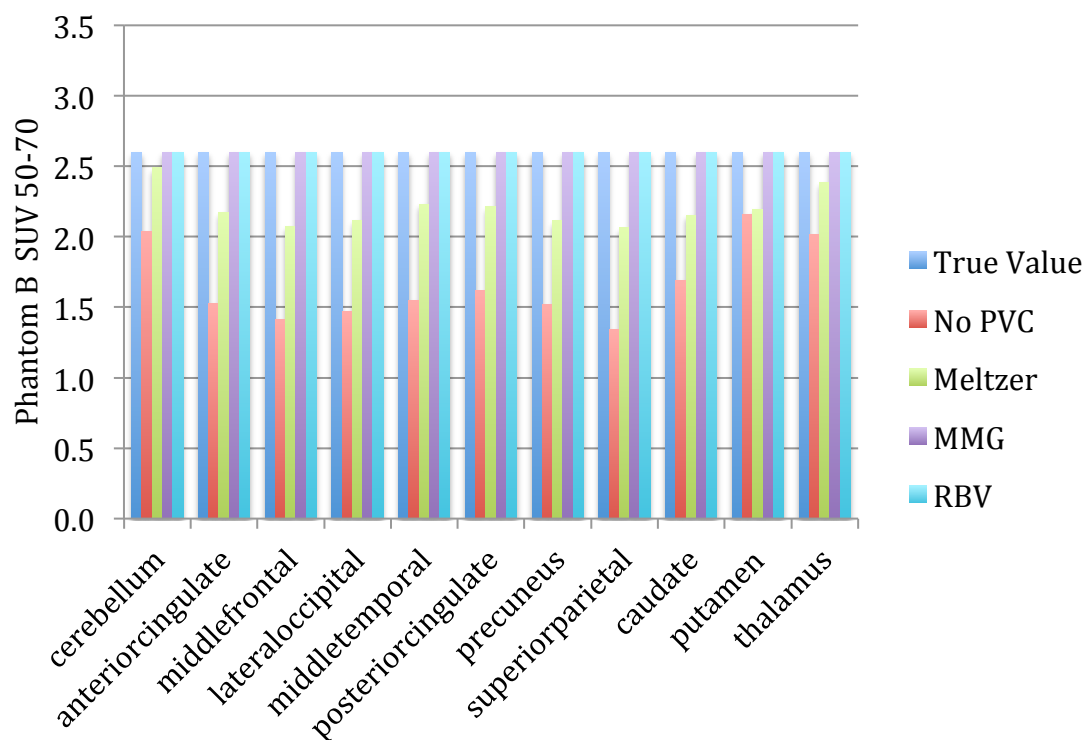


**Figure 13 Phantom B uncorrected and partial volume-corrected regional SUV 50-70 minute values.** Phantom B was assigned a constant SUV value for all GM voxels and a constant SUV value for all WM voxels such that GM SUV > WM SUV. Uncorrected SUV values underestimate true activity with RC values ranging from 0.52 in the superior parietal region to 0.83 in the putamen. Meltzer-corrected SUV values also underestimate true activity, though to a lesser extent, with RC values ranging from 0.79 in the superior parietal region to 0.92 in the thalamus. The MMG- and RBV-correction methods fully recover activity in all cortical and subcortical GM regions.

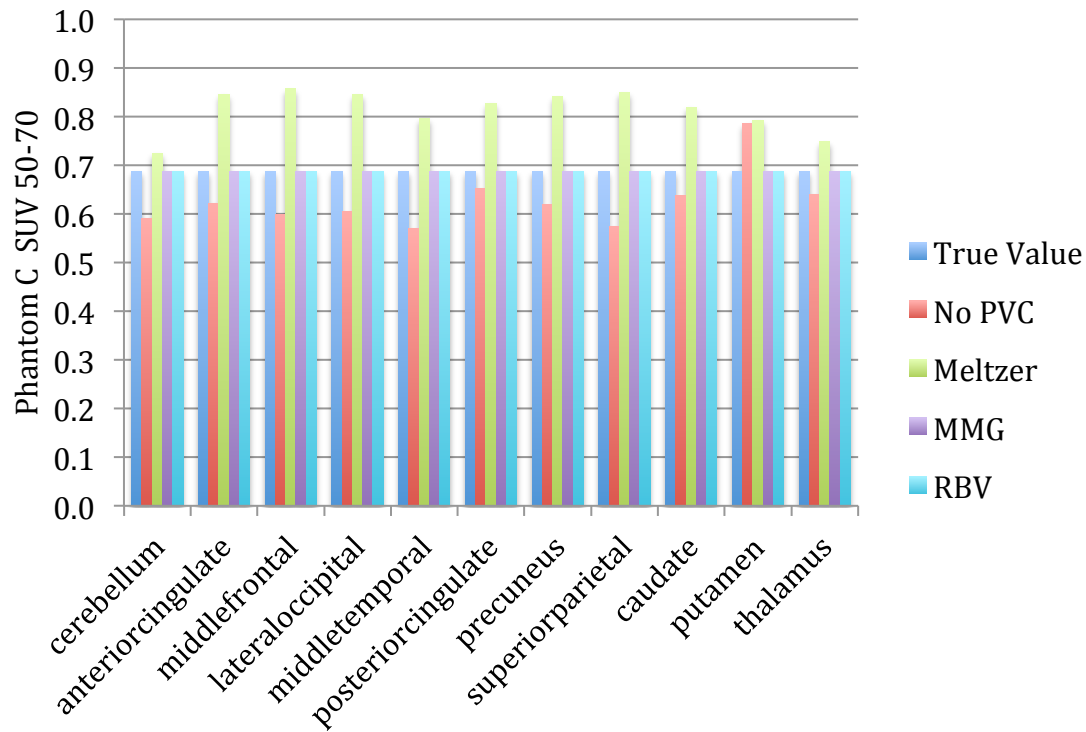


**Figure 14 Phantom C uncorrected and partial volume-corrected regional SUV 50-70 minute values.** Phantom C was assigned a constant SUV value for all GM voxels and a constant SUV value for all WM voxels such that GM SUV < WM SUV. Uncorrected SUV values underestimate true activity in all regions except the putamen, in which activity is overestimated. Meltzer-corrected SUV values overestimate true activity across all regions with RC values ranging from 1.09 in the thalamus to 1.25 in the middle frontal. The MMG- and RBV-correction methods fully recover activity in all cortical and subcortical GM regions.



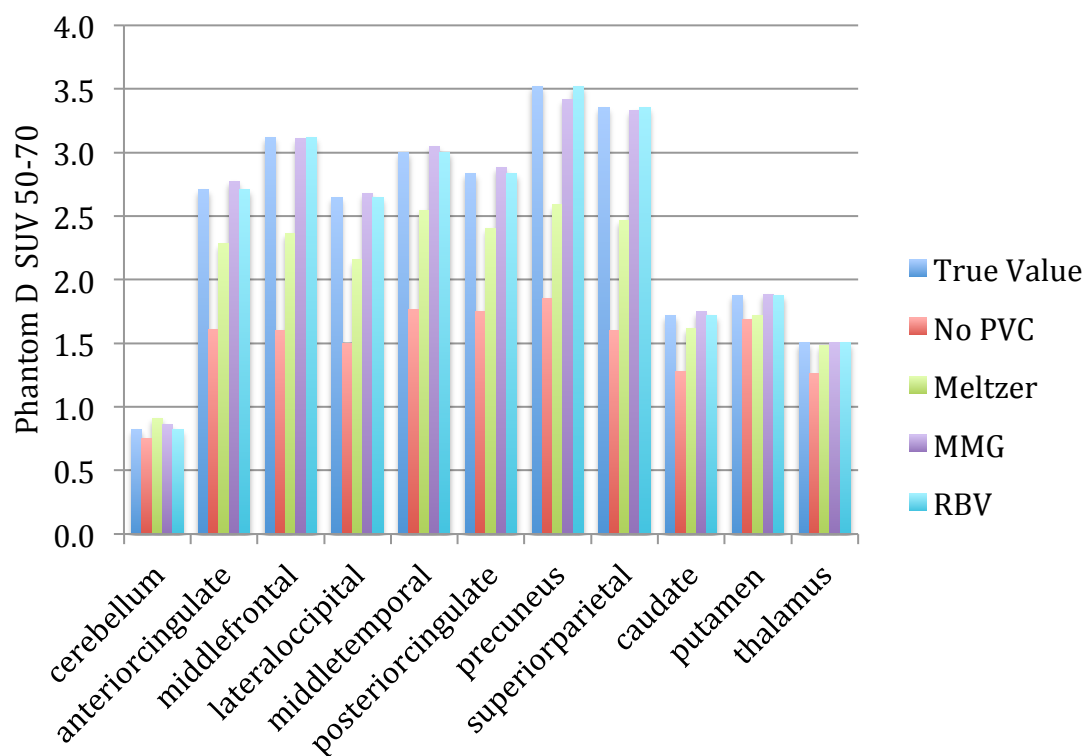


**Figure 15 Phantom D uncorrected and partial volume-corrected regional SUV 50-70 minute values.** Phantom D was assigned variable SUV values across GM regions such that GM SUV > WM SUV. Uncorrected and Meltzer-corrected SUV values underestimate true activity in all regions. MMG-corrected RC values ranged between 0.97 in the precuneus and 1.02 in the anterior cingulate. The RBV-correction method fully recovers activity in all cortical and subcortical GM regions.

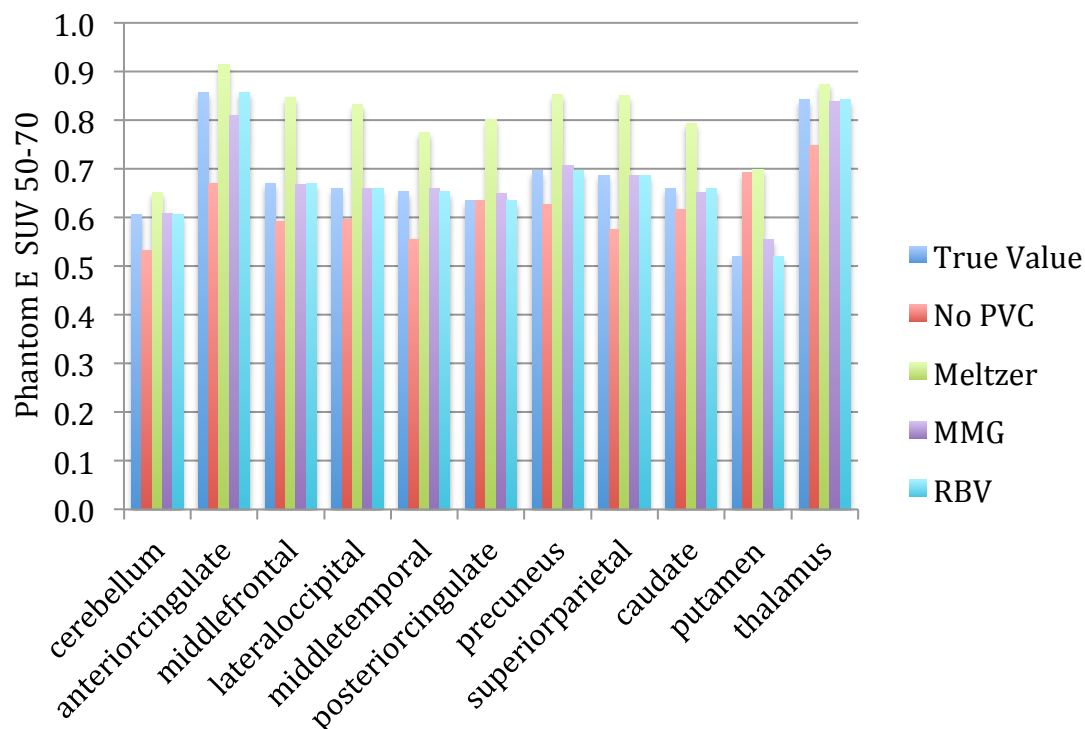


**Figure 16 Phantom E uncorrected and partial volume-corrected regional SUV 50-70 minute values.** Phantom E was assigned variable SUV values across GM regions such that GM SUV < WM SUV. Meltzer-corrected SUV values overestimate true activity in all regions with RC values ranging from 1.04 in the thalamus to 1.34 in the putamen. MMG-corrected RC values ranged between 0.94 in the anterior cingulate and 1.07 in the putamen. The RBV-correction method is the only PVC method to fully recover activity in all cortical and subcortical GM regions.

#### 2.3.4 Discussion

In this comparison of three PVC methods, five phantom SUV PET images were created to validate the implementation of the Meltzer, MMG, and RBV PVC methods. Phantom A represented the ideal case of constant radioactivity concentration across the entire brain for the Meltzer method, with partial volume effects (PVEs) only resulting from spill-out of radioactivity concentration signal to CSF space. Phantoms B and C represented ideal cases for the MMG PVC method, with PVEs resulting from spill-out of radioactivity signal to CSF space and differing GM and WM activity concentrations, but no PVEs resulting from within GM differences. Phantoms D and E represented the ideal cases for RBV with PVEs resulting from spill-out of signal to CSF space, differing GM and WM radioactivity concentrations, and variable GM activity concentration. Application of the Meltzer method resulted in exact recovery of regional SUV data in Phantom A, application of the MMG method resulted in exact recovery of regional SUV data in Phantoms B and C, and application of the RBV method resulted in exact recovery of regional SUV data in Phantoms D and E. These results successfully validate the implementation of each of the partial volume correction methods for this thesis.

The comparative evaluation of these PVC methods also demonstrated the strengths and weaknesses of the individual methods. With the exception of the ideal case of Phantom A, application of the Meltzer PVC method resulted in underestimated SUV values for high-PiB-binding phantoms B and D and overestimated SUV values for low-PiB-binding phantoms C and E. Both of these effects are due to the Meltzer method not accounting for PVEs or spill-over from

white matter. In the high-PiB-binding phantoms, WM activity is lower than GM activity. Therefore, GM signal spill-over to neighboring WM space results in lower uncorrected GM signal. As the Meltzer PVC does not recover GM signal spill-over to relatively low-signal WM space, activity in high-PiB-binding phantoms is underestimated. In the low-PiB-binding phantoms, WM activity is higher than GM activity. Therefore, neighboring WM signal spill-over increases uncorrected GM signal. Since Meltzer does not correct for spill-over between GM and WM regions, this spill-over is unaddressed and activity in low-PiB-binding phantoms is overestimated.

Application of the MMG method to Phantoms D and E resulted in average RC values across cortical and subcortical GM regions of  $1.01 \pm 0.02$  and  $1.00 \pm 0.03$ , respectively. These values are, of course, relatively close to an exact recovery coefficient of 1.0. This suggests that between-GM-region spill-over, which MMG does not correct, is a minor contributor to total partial volume error relative to GM-WM spill-over and spill-out into CSF spaces, which MMG does correct. Only the RBV PVC method, which does correct for spill-over between GM regions, resulted in exact RC values of 1.0 across all phantoms, as expected.

One limitation of this component of this thesis was that all simulated phantoms generated had homogeneous radioactivity concentrations within white matter. A previous study demonstrated that heterogeneity in white matter signal may influence the accuracy of the Müller-Gärtner method in cortical grey matter signal [11]. Heterogeneity in white matter signal may also result in increased variability in grey matter signal following application of the MMG PVC method. The

effect of white matter heterogeneity was not evaluated in this study and should continue to be explored in the future.

Another limitation was that, although standard deviation within the superior parietal region is presented in **Table 3** for each of the phantoms and PVC methods, variability in PiB PET images resulting from each of the PVC methods was not explicitly examined. However, the following chapter includes a more thorough characterization of variability in PiB PET images resulting from each of the partial volume correction methods using a noise magnification measurement [9, 76].

# Chapter 3

## PiB PET and Post-mortem Measure of Amyloid Load

### 3.1 Introduction

#### 3.1.1 The Partial Volume Effect in Amyloid Imaging

Partial volume effects may be of particular importance in neurodegenerative amyloid PET studies in elderly subjects. Cortical atrophy, with the expansion of CSF spaces and thinning of gyri, may result in the underestimation of tracer uptake in cortical grey matter. High non-specific white matter uptake can cross-contaminate cortical grey matter activity, potentially inflating the signal in healthy controls with little to no A $\beta$  plaque deposition or reducing the signal in AD patients with relatively high cortical GM signal. These PVEs can potentially obscure cross-sectional group differences and mask longitudinal changes in individuals.

Few amyloid PET studies have been carried out using PVC techniques. In a PiB PET study, Mikhno et al (2008) [77] demonstrated a higher significance in the separation of AD and healthy control subjects when performing voxel-based analysis with the MMG method, though the group separation was already highly significant without PVC. Drzezga et al (2008) [78] investigated a cohort of AD and semantic dementia patients using both FDG and PiB. Semantic dementia is characterized by a different pattern of atrophy than that of AD, and MMG was used to remove potentially different effects of atrophy between the two groups. PVC appeared to reduce the significance in the difference of PiB uptake between the two

groups, while increasing the significance of glucose metabolism. Rabinovici et al (2010) [79] applied the two-compartment Meltzer PVC method in FDG and PiB PET studies of healthy controls, early-onset AD and late-onset AD subjects. Early-onset AD patients tend to exhibit more severe atrophy than late-onset. As in the case of Mikhno et al (2008), the significance of separation between the AD groups and healthy controls increased with PVC.

In a relatively comprehensive study of PVEs in amyloid PET imaging, Thomas et al (2011) [11] evaluated the MG, MMG, and RBV partial volume correction methods on simulated phantom data and a clinical cohort. RBV-corrected data were shown to be more accurate than MG and MMG on phantom data when a perfect parcellation is available, as it corrects within tissue classes. In a clinical cohort of 70 subjects with  $^{18}\text{F}$ -flutemetamol PET data, Thomas et al (2011) demonstrated the MG and MMG methods may overestimate GM hippocampal activity in typical Alzheimer's disease  $^{18}\text{F}$ -Flutemetamol distributions as high activity from neighboring GM regions can spill into the low-activity hippocampus. Given the low concentration of  $\text{A}\beta$  plaques in the hippocampus in AD subjects, the authors suggested that PVC techniques that account for multiple regions are more appropriate for amyloid PET studies.

### **3.1.2 PiB PET and Postmortem Correlations**

Despite FDA approval of a number of A $\beta$  PET radiotracers to aid in the evaluation of different types of dementia, the definitive diagnosis of AD still requires autopsy confirmation based on the neuropathological hallmarks A $\beta$  plaques and neurofibrillary tangles. The minimum level of A $\beta$  pathology associated with detectable PiB retention has not been established, and the extent of agreement between A $\beta$ -binding radioligands and neuropathological assessment is an ongoing area of investigation [65, 66, 80-87]. However, much has been gained in the revision of diagnostic criteria for AD that incorporates the results of in vivo imaging studies [62, 63].

Ikonomic et al (2008, 2012) [65, 81] applied a modified form of the Meltzer PVC method to PiB PET data in studying the correspondence between PiB PET and postmortem measures of amyloid load, but PiB measures without PVC were not reported.

## **3.2 Materials and Methods**

The objective of this component of the thesis was to investigate the effect of several PVC techniques on the correspondence between PiB PET and postmortem measures of amyloid load.

### **3.2.1 Subjects**

Twelve subjects who had postmortem histological assessments of amyloid load and antemortem PiB PET and MR imaging scans form the basis of this study.



Two have been previously reported on [65, 81]. All subjects were recruited and scanned prior to this thesis work. Image data for these subjects were used in this thesis work with permission from Dr. William Klunk, Co-Director of the University of Pittsburgh Alzheimer Disease Research Center (ADRC). Clinical diagnoses at time of scanning included Probable AD, frontotemporal dementia (FTD), and Dementia with Lewy Bodies (DLB). MMSE scores at PiB PET scan ranged from 29 to 1. Ages at scan ranged from 54 to 85 years. Intervals from time-of-scan to death ranged from  $35.8 \pm 23.4$  months. Subject demographics are shown in **Table 5**.

**Table 5** Demographics of subjects with postmortem and antemortem measures of amyloid load.

Subject	Diagnosis	Gender	Age at scan (years)	MMSE at scan	PET-Autopsy Interval (months)	PiB PET Scan Duration
PiB-01	AD	Female	63	1	10.3	0-60 min
PiB-02	AD	Male	58	18	42.3	0-90 min
PiB-03	DLB	Male	77	10	17.2	0-90 min
PiB-04	AD	Male	54	19	30.4	0-90 min
PiB-05	AD	Male	79	2	32.3	0-90 min
PiB-06	AD	Male	74	21	10.5	0-90 min
PiB-07	AD	Female	66	21	34.6	0-90 min
PiB-08	FTD	Male	80	7	37.2	0-90 min
PiB-09	AD	Female	79	25	45.5	0-90 min
PiB-10	NC	Female	80	28	31.8	40-70 min
PiB-11	NC	Male	85	29	37.4	40-70 min
PiB-12	AD	Male	77	23	100.4	0-90 min

Diagnoses include probable Alzheimer's disease (AD), dementia with Lewy bodies (DLB), frontotemporal dementia (FTD), and normal cognition (NC). Cognitive diagnoses were determined through a battery of tests including the Mini Mental State Exam (MMSE).

### **3.2.2 MR and PiB PET Imaging**

All subjects underwent PiB PET and MR imaging prior to death. Subjects received a T1-weighted SPGR MR scan (1.5T, GE Signa) (n=11) or a magnetization prepared rapid gradient echo (MPRAGE) MR scan (3T, Siemens Tim Trio) (n=1) for anatomic region of interest definition and PVC tissue segmentation guidance. PET data were acquired as previously described [65, 81]. PiB PET data was collected using a Siemens/CTI ECAT HR+ scanner (3D imaging mode, 63 image planes, 15.2 cm FOV) following the injection of  $14.9 \pm 1.5$  mCi of high-specific activity PiB as slow bolus. PET emission data were acquired over 0-90 minutes (34 frames, n=9), 0-60 minutes (31 frames, n=1), or 40-70 minutes (6 frames, n=2) post-injection. PET data was corrected for scanner normalization, dead-time, attenuation, scatter, and radioactivity decay, and reconstructed using filtered back-projection. The final reconstructed image resolution was  $6.46 \times 6.09 \times 5.71$ mm FWHM.

### **3.2.3 Brain Autopsy and Dissection**

The brain autopsy and dissection process was performed by Dr. Milos Ikonovic of the University of Pittsburgh Department of Neurology and is described in full in Ikonovic et al (2008) [81] and Ikonovic et al (2012) [65]. Briefly, brain autopsies were performed according to the Consortium to Establish a Registry for Alzheimer's Disease (CERAD) guidelines [35] under a University of Pittsburgh ADRC protocol approved by the University of Pittsburgh Institutional Review Board. The left cerebral hemispheres were placed in 10% buffered formalin, and after 21 days fixation, sliced into 1-cm thick axial blocks. Brain

regions that were sampled included the frontal cortex (FRC), temporal lobe (LTC), occipital cortex (OCC), putamen (PUT), hippocampus (HIP), anterior cingulate (ACG), and precuneus (PRC).

To quantify regional plaque loads, 1 cm<sup>3</sup> tissue cubes were dissected from axial tissue blocks of the left hemisphere. Tissue cubes were cut in half along a plane parallel to their ventral face and each cube yielded two 1cm x 1cm x 0.5cm tissue blocks. One half was embedded in paraffin, and sectioned into sequential 6 µm-thick sections to examine the spatial relationship of plaques labeled with 6-CN-PiB [81, 88], a highly fluorescent derivative of PiB. 6-CN-PiB is known to almost exclusively label Aβ-containing structures including cored and diffuse plaques and vascular amyloid [80, 81].

#### **3.2.4 6-CN-PiB Histology**

6-CN-PiB histofluorescent labeling was also performed by Dr. Milos Ikonovic and is described in full in Ikonovic et al (2008) [81] and Ikonovic et al (2012) [65]. Briefly, tissue sections were incubated in 6-CN-PiB for 45 minutes, dipped three times in phosphate buffer (PB, 0.1 M), followed by a 1-min differentiation in a solution containing 132.9mM NaCl, 8.7mM K<sub>2</sub>HPO<sub>4</sub>, and 1.5mM KH<sub>2</sub>PO<sub>4</sub> (pH 7.4), and cover-slipped with Fluoromount (Electron Microscopy Services, Hatfield, PA). Plaque loads were quantified using NIH ImageJ (Rasband, W.S., ImageJ, US National Institutes of Health, Bethesda, MD, USA, <http://rsb.info.nih.gov/ij/>, 1997–2014) in three equally spaced sections. Sections from each brain region examined contained both WM and GM. Images used for

plaque load analysis were taken exclusively in the GM areas, avoiding the crest of gyri and the depths of sulci. Adjacent sections were processed using cresyl violet and used to determine the boundaries between white and grey matter. Low-magnification, high-resolution images of histofluorescence in GM areas were acquired using a motorized stage and the Virtual Slice module of StereoInvestigator (Microbrightfield, Inc., Williston, VT, USA). A 1000x750  $\mu\text{m}$  field of the greatest plaque of frequency was imaged in two sections chosen randomly from each of the tissue cubes. Plaque load was determined from the percent area (% Area) occupied by 6-CN-PiB positive plaques.

### **3.2.5 Region of Interest Matching**

Matching of the autopsy tissue cube sampling to the ROI sampling of the dynamic PET image data was based on a previously described method [65, 81] and performed by University of Pittsburgh PET Research Center staff member Carl Becker. ROI-labeled images of axial autopsy blocks guided ROI generation on the antemortem full-resolution axial MR image. Each subject's MR image was manually reoriented to match the orientation of the autopsy slice photograph using image transformation software developed at the University of Pittsburgh PET Center. ROIs were hand drawn on the reoriented MR to match those on the autopsy image using ROItool software. Adjustments to ROI placement on MR were necessary due to postmortem collapse of the ventricles and general brain deformation (**Figure 17**).

Each subject's dynamic PET image was then coregistered and resliced to the reoriented MR image using automated methods. Standardized uptake value 40-60

minute (SUV60) and 50-70 minute (SUV70) parametric images were generated from the coregistered PET by averaging activity over the appropriate time frames on a voxel basis, then multiplying by the subject's weight and dividing by injected dose using image algebra software developed at the University of Pittsburgh PET Center.

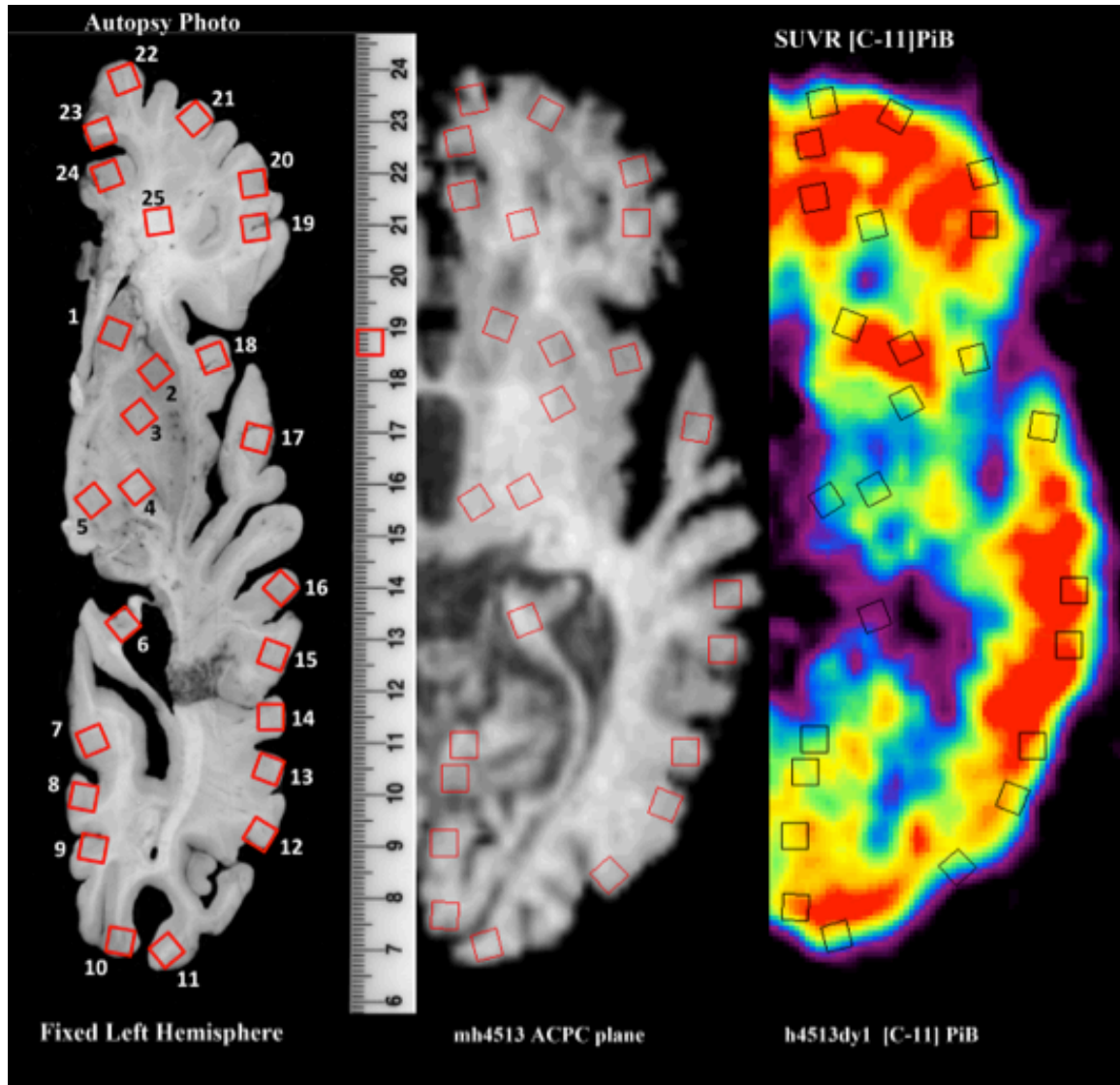


**Figure 17 Snapshot of ROI matching between post-mortem tissue and antemortem MR image for subject PiB-09.** From left-to-right, (A) is the post-mortem autopsy tissue with excised regions overlaid, (B) is the antemortem MR image with ROIs hand-drawn to match those in the autopsy photo, and (C) is the PiB SUVr image with hand-drawn ROIs overlaid.

### 3.2.6 Partial Volume Correction Application and Sampling

As part of this thesis work, each subject's reoriented MR image was parcellated using FreeSurfer software (Martinos Center for Biomedical Imaging, Harvard, MA, USA) [67, 68] as described in **Section 2.3.2.3**. Upon completion of each FreeSurfer stream, the segmentation and parcellation was visually inspected and manually edited using FreeSurfer tool "tkmedit" to ensure GM, WM, CSF, and within-tissue anatomical boundaries were properly followed. Eighty-four parcellation regions were converted to binary masks from the "aparc+aseg" FreeSurfer parcellation map using the "mri\_convert" tool within FreeSurfer and "fslmaths" utility within FSL. As described in **Section 2.3.2.3**, the 84 contiguous, non-overlapping binary masks spanned the entire brain and consisted of all available lateralized cortical and subcortical GM regions, a whole cerebral WM region, a whole cerebellar GM region, a cerebellar WM region, and the brainstem. The binary parcellation masks were combined to create whole GM, whole WM, and whole brain-tissue masks (**Figure 18**).

For each subject, voxel-level Meltzer-corrected PiB SUV images were generated from the subject's PiB SUV60 and SUV70 parametric images, and the whole-brain tissue mask, as described in **Section 2.2.1**. The whole-brain tissue mask was convolved by the PET scanner point spread function (6.46 x 6.09 x 5.72mm) using the "Smooth" function within SPM8. The SUV PET image was then divided by the smoothed tissue map using the "fslmaths" tool in FSL.

The GTM method was performed using all FreeSurfer parcellation maps and SUV parametric images in order to determine a partial volume-corrected subcortical

WM value, as described in **Section 2.2.2**. This value was then used in the calculation of voxel-level MMG-corrected SUV images from the SUV parametric images and GM and WM tissue masks, again using SPM8 and FSL tools.

The autopsy-based ROIs were incorporated into the contiguous, non-overlapping 84 binary masks. Any subregion generated by the intersection of an autopsy-based ROI and binary mask was subtracted from the binary mask and treated as a new, separate binary mask using “fslmaths”. This FreeSurfer- and autopsy-derived binary mask parcellation of the brain (**Figure 18**) was used to generate voxel-level RBV-corrected PiB SUV60 and SUV70 images, as described in **Section 2.2.3**.

The “No PVC”, Meltzer-corrected, MMG-corrected, and RBV-corrected SUV parametric images were all sampled using the FreeSurfer-derived GM cerebellum and FSL’s “fslstats” tool, and normalized to this value to generate corrected and uncorrected SUVR60 and SUVR70 parametric images. Each subject’s autopsy-based hand-drawn ROIs were also segmented into GM and WM portions using the FreeSurfer-derived GM and WM binary masks. This was done simply through the use of “fslmaths” image multiplication. The four SUVR parametric images for each subject (**Figure 19**) were then sampled using GM-only autopsy-based ROIs to mimic the histofluorescence plaque load analysis, which was assessed exclusively in the GM of each tissue cube. Sampling was performed through FSL’s “fslstats” tool to obtain regional mean and standard deviation SUVR values. An overview of the entire processing pipeline is shown in **Figure 20**.



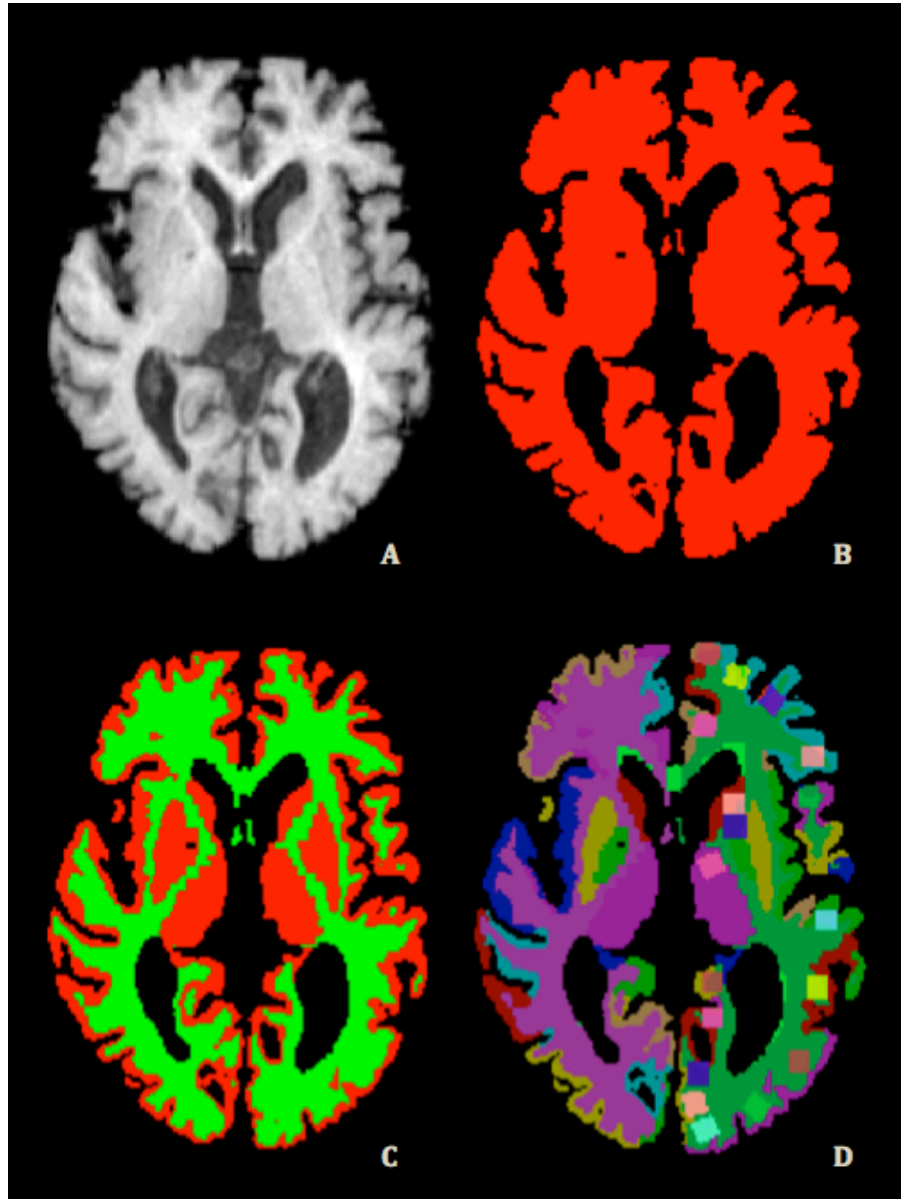


**Figure 18 MR image for subject PiB-02 with corresponding FreeSurfer segmentations and parcellations.** The antemortem MR image (A) was segmented into (B), a whole brain tissue binary mask that was used for the Meltzer-correction and (C), GM (red) and WM (green) binary masks for use in MMG-correction. (D) Hand-drawn autopsy-matched ROIs (squares) were inserted into the FreeSurfer cortical parcellation for use in RBV PC correction.

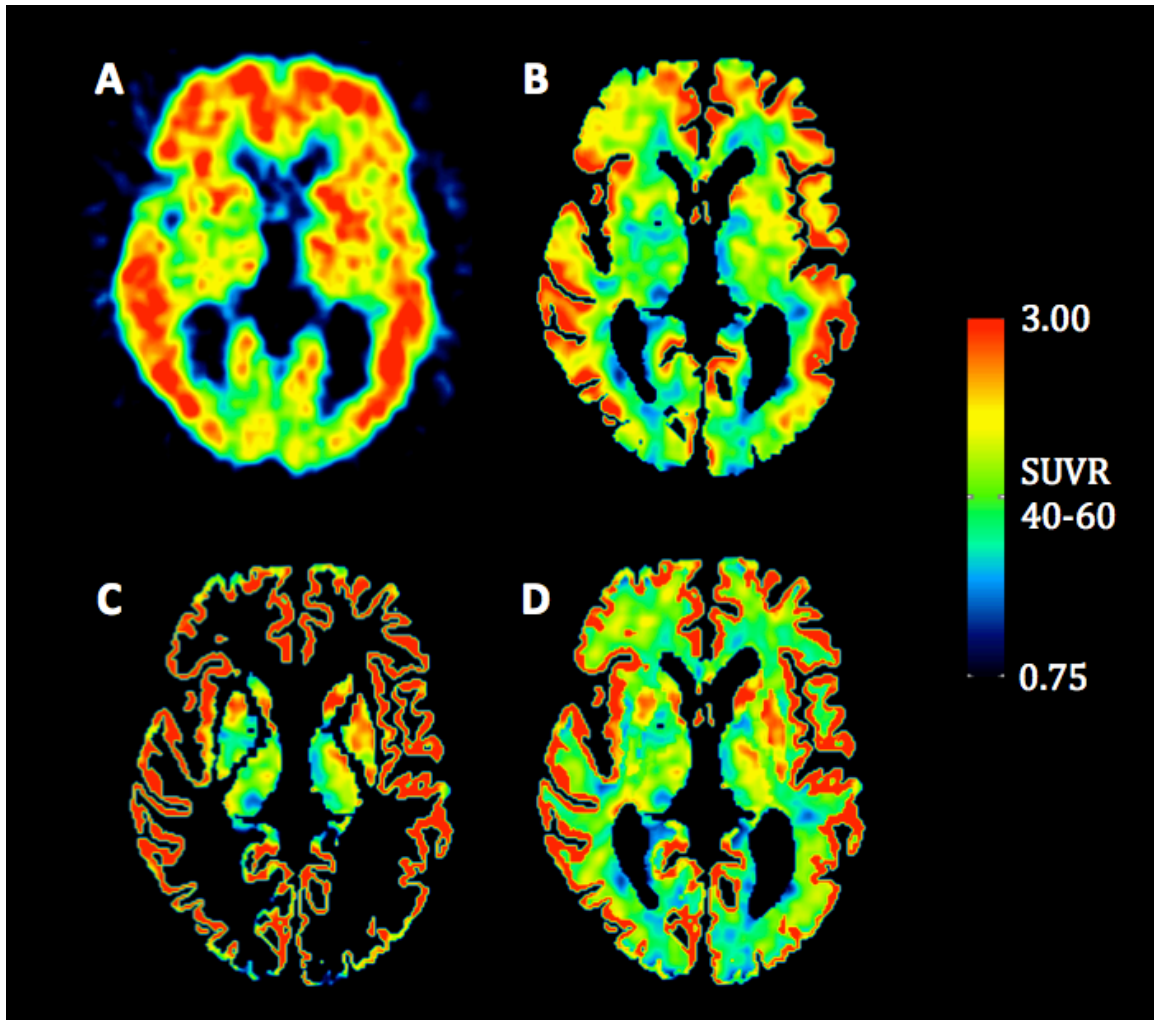


**Figure 19 Uncorrected and partial volume-corrected SUVR60 PiB PET images for subject PiB-02.** The Meltzer-corrected SUVR image (B) was masked with a whole brain-tissue binary map to remove relatively high activity voxels outside of the brain. The MMG-corrected SUVR image (C) was masked with a binary grey matter map to remove relatively high-activity voxels from CSF and WM spaces. Neither the uncorrected (A) nor the RBV-corrected (D) SUVR images was masked. As part of the RBV-correction method, voxels outside of parcellated regions are set to zero.

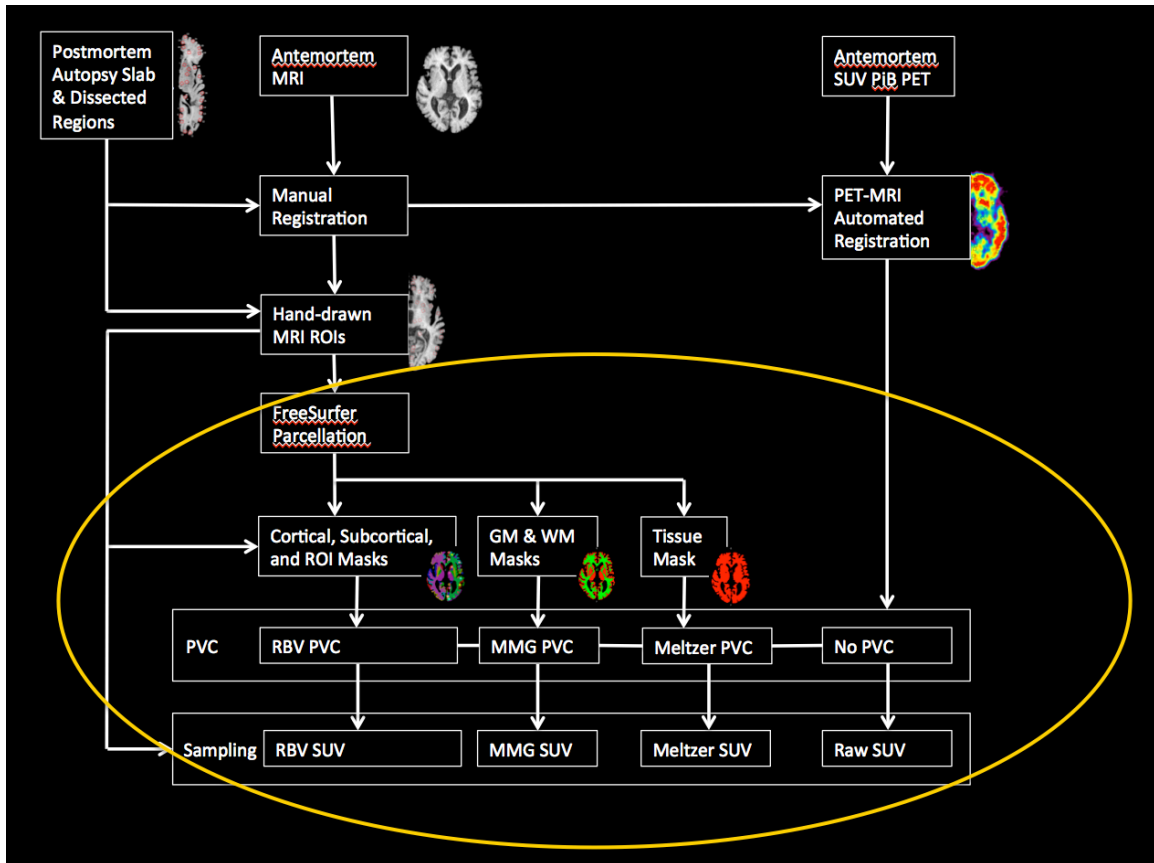


**Figure 20 Synopsis of workflow for autopsy-guided antemortem PiB PET partial volume correction and sampling.** Work that is part of this thesis is circled in yellow. Both manual and automated techniques were used to generate regions of interest for matching autopsy slab dissected regions and generating anatomical regions for partial volume correction. Three partial volume correction methods were applied to antemortem PET data.

### 3.2.7 Statistical Analysis and Correlations

The noise magnification factor (NMF), defined as the ratio of the coefficient of variation (CoV) after PVC to the coefficient of variation before PVC [9, 76], was used to quantify noise propagation in brain tissue regions for each PVC technique. A NMF of 1.0 signifies no change in noise within a region, a NMF greater than 1.0 signifies an increase in noise due to PVC, and a NMF less than 1.0 signifies a decrease in noise due to PVC.

While the NMF has traditionally been used to measure noise propagation resulting from PVC within brain tissue, it does not differentiate variability created by the PVC method itself and inherent variability within the PET image. The objective of all PET PVC techniques is to reverse the effects of the PET scanner point spread function, essentially unsmoothing the PET image. In doing so, some increase in voxel-level variability may occur as voxel or regional values become more distinct and less influenced by neighboring radioactivity concentrations. However, the PVC technique employed may further increase variability due to a specific operation performed, such as a subtraction of white matter-radioactivity concentration from the PET image that introduces negative voxel values.

In order to quantify variability resulting purely from the PVC method, CSF ROIs were hand drawn in ventricular CSF space to calculate CSF NMFs. CSF is considered a different compartment from both blood and brain tissue, separated from blood by the blood-CSF barrier or choroid plexus [89]. The choroid plexus is made up of epithelial cells and tight gap junctions that filter plasma from the blood to form cerebrospinal fluid. While the PiB radiotracer was designed to cross the

blood-brain barrier, it is not known to cross the blood-CSF barrier. As such, PiB PET radiotracer concentrations in ventricular CSF are assumed to be zero. Therefore, a CSF NMF greater than 1.0 should be a result of noise propagation due to the characteristics of the PVC method.

Ventricular CSF ROIs were hand-drawn for 11 of the 12 subjects (**Figure 21**). A CSF ROI was not drawn for subject PiB-04 as the subject's ventricles were too small to allow for a CSF ROI. CSF ROIs were drawn at approximately the same size as hand-drawn autopsy ROIs, 7.5 x 7.5 x 8 mm, and were used to sample all partial volume corrected images.

Regional correlation between antemortem SUVR and 6-CN-PiB % Area across subjects was evaluated using Pearson's correlation coefficient. Statistical significance was set at 0.05 (two-sided).

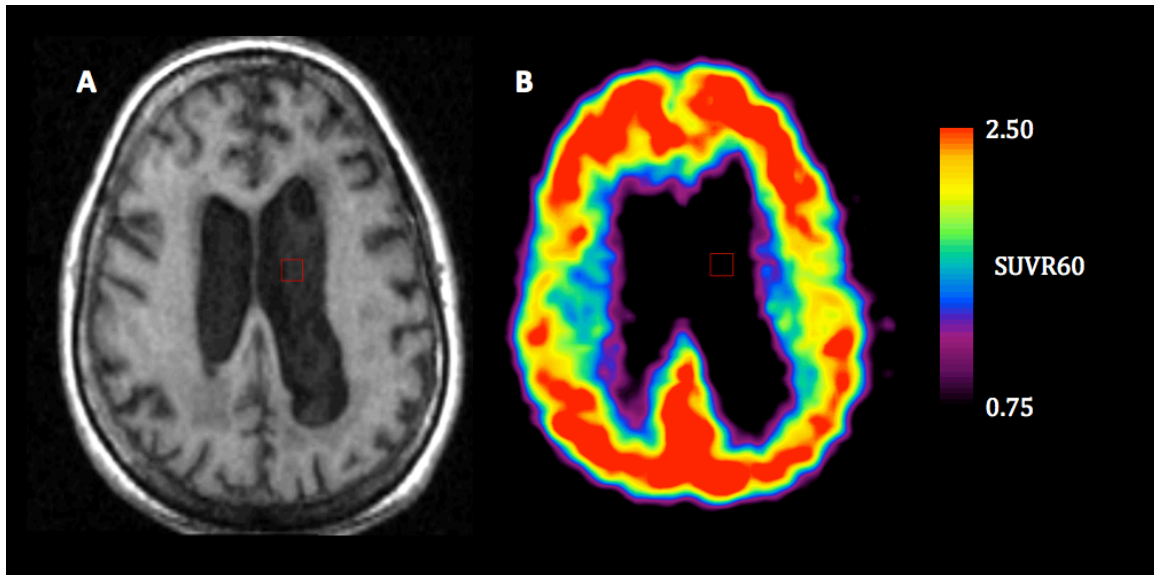


**Figure 21 A ventricular CSF region of interest overlaid on subject PiB-01 MR and SUVR PiB PET images.** The square region of interest was drawn on the MR image (A) and transferred to the coregistered SUVR60 PiB PET image (B). Noise magnification factors were calculated for 11 of the 12 subjects based on ventricular CSF ROIs in order to assess the noise propagation of each of the partial volume correction methods applied.

### 3.3 Results

#### 3.3.1 PiB PET Outcome Measures

**Figures 22 and 23** show mean SUVR60 and SUVR70 values, respectively, for the precuneus across subjects and PVC techniques. On average, the Meltzer PVC method increased precuneus SUVR values by 14.9% and 14.8% for SUVR60 and SUVR70, respectively. The MMG method increased SUVR values for 51.5% and 54.5% for SUVR60 and SUVR70, respectively. The RBV PVC method showed similar increases in SUVR measures of 52.2% and 54.1%. PVC increased measured SUVR in all subjects, with the exceptions of PiB-01 and PiB-09, which had reductions of 1.1% – 1.8% in SUVR60 and SUVR70 after correction with the Meltzer method, and PiB-10, which had reductions in SUVR ranging from 13.5% – 22.3% for both MMG and RBV methods. The largest increases in SUVR due to PVC occurred in PiB-05, with ~31%, ~93%, and ~97% increases in SUVR60 resulting from Meltzer-correction, MMG-correction, and RBV-correction.

SUVR60 and SUVR70 values were highly correlated across subjects in the precuneus (**Figure 24**). All PVC techniques resulted in highly significant correlation coefficients between the two outcome measures of 0.998 (Meltzer and MMG) to 0.999 (RBV).

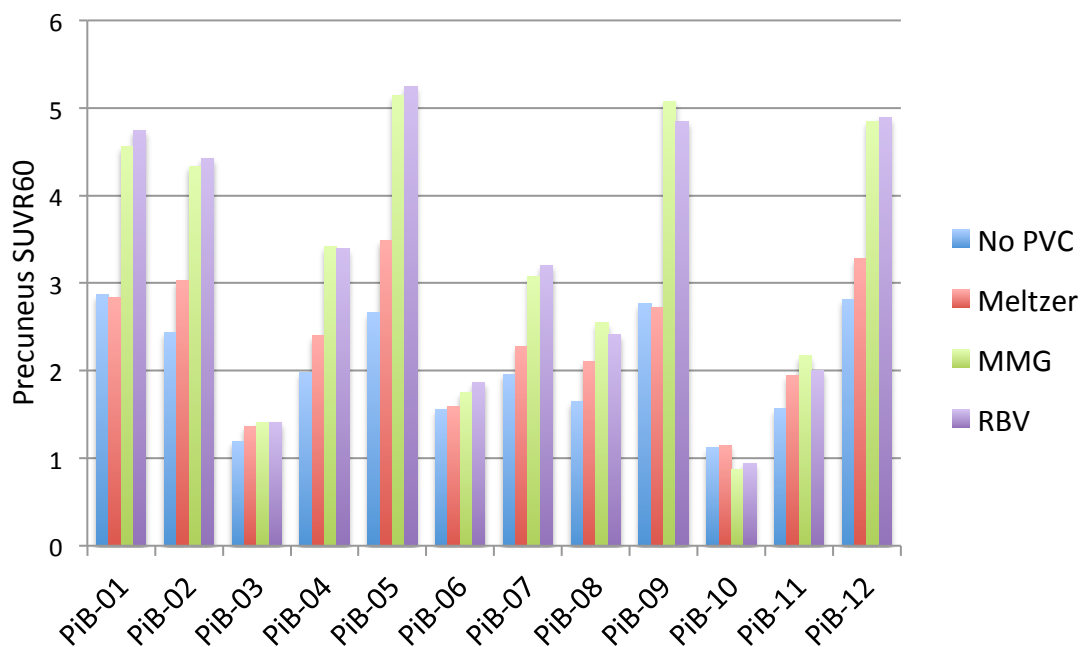


**Figure 22 Mean precuneus SUVR60 values across subjects and partial volume correction methods.** On average, the Meltzer PVC method increased precuneus SUVR values by 14.9%. The MMG and RBV methods increased SUVR values on average by 51.5% and 52.2%, respectively.



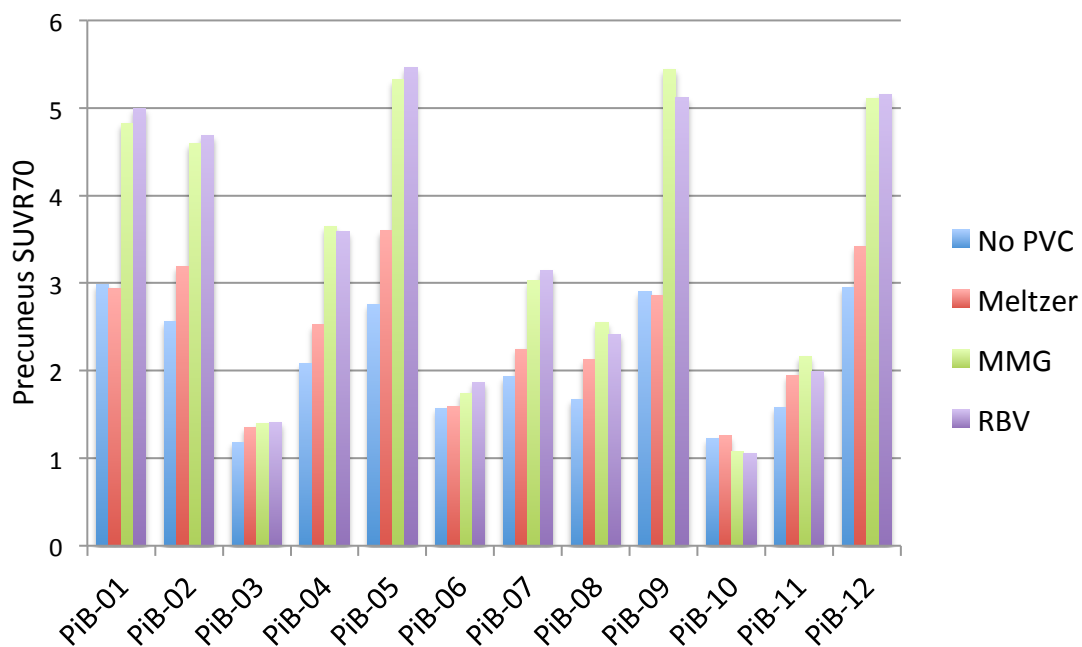


**Figure 23 Mean precuneus SUVR70 values across subjects and partial volume correction methods.** On average, the Meltzer PVC method increased precuneus SUVR values by 14.8%. The MMG and RBV methods increased SUVR values on average by 54.5% and 54.1%, respectively.

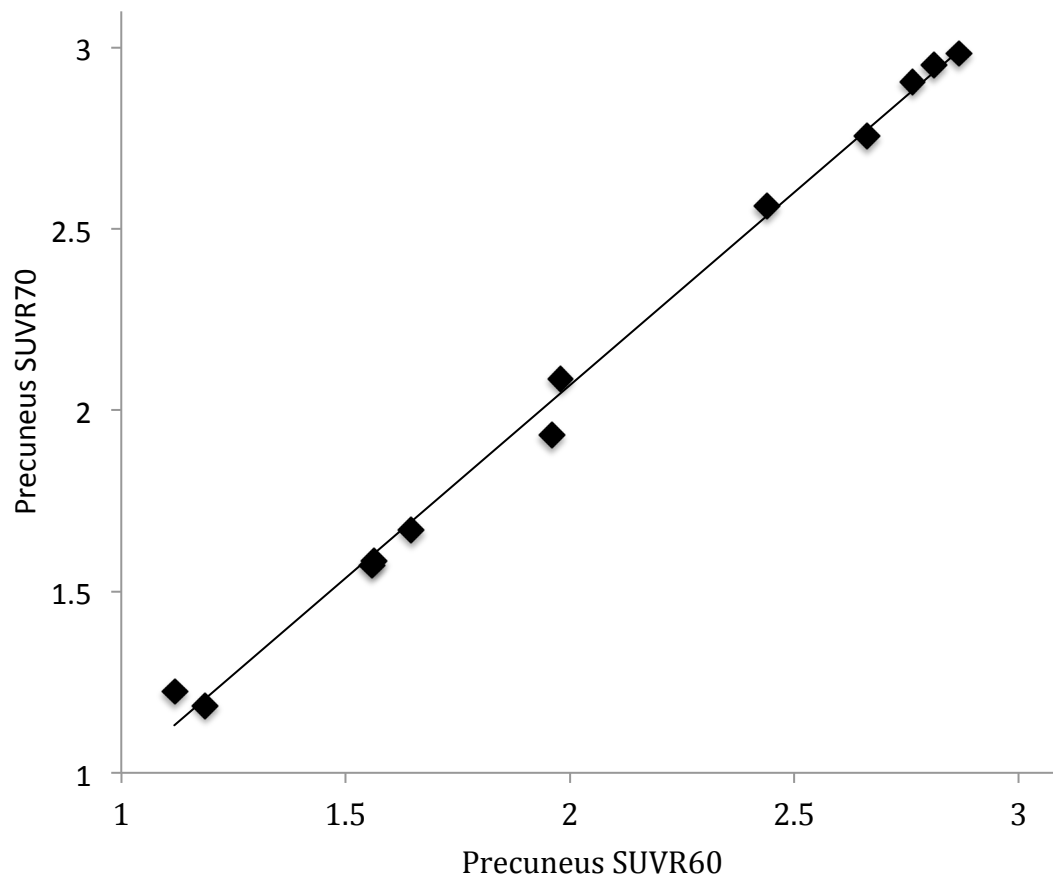


**Figure 24 Correlation between SUVR60 and SUVR70 in the precuneus across subjects.** The slope for the linear relationship is 1.064 with a highly significant Pearson's correlation coefficient of 0.998 ( $p < 0.001$ ).

### 3.3.2 Partial Volume Correction Noise Propagation

**Figures 25 and 26** show noise magnification factors (NMFs) for the precuneus across subjects based on SUVR60 and SUVR70 data, respectively. In 5 of the 12 cases (PiB-02, PiB-04, PiB-05, PiB-09, and PiB-12), the Meltzer correction method propagated noise more than either of the other two partial volume correction methods for SUVR60 data. These factors ranged from 1.41 (PiB-12) to 2.57 (PiB-05). In all other subjects (7 out of 12 cases), the MMG correction method had the highest noise magnification factor for SUVR60 data, ranging from 1.01 (PiB-07) to 2.29 (PiB-11). In no case was the RBV correction method the greatest propagator of noise. It in fact demonstrated NMFs less than 1.00 in five of the subjects for the SUVR60 data (PiB-03, PiB-07, PiB-09, PiB-10, and PiB-12). Across all subjects, the average NMFs for the SUVR60 data were 1.68, 1.53, and 1.28, for MMG, Meltzer, and RBV correction methods, respectively.

Similar relative noise magnification factors were seen for SUVR70 data. Average NMFs were 1.63, 1.37, and 1.19 for MMG, Meltzer, and RBV correction methods, respectively.

**Figure 27** shows NMFs for the ventricular CSF across subjects based on SUVR60 data. CSF NMFs for RBV-corrected data are not shown as RBV-correction results in zero voxels outside of the brain parcellation. For all subjects, the CSF ROI average and standard deviation RBV-corrected SUVR values were zero. For ten subjects (excluding subject PiB-09), application of both the Meltzer and MMG PVC methods propagated noise in ventricular CSF space, with Meltzer-correct CSF NMFs ranging from 1.01 to 2.43 and MMG-corrected CSF NMFs ranging from 2.00 to 7.02.

In all ten subjects, the MMG PVC method propagated noise to a greater extent than the Meltzer PVC method. In the case of subject PiB-09, application of the Meltzer and MMG PVC methods resulted in CSF NMFs of 0.99 and -3.09, respectively. The negative NMF was a result of a negative mean value in the CSF.

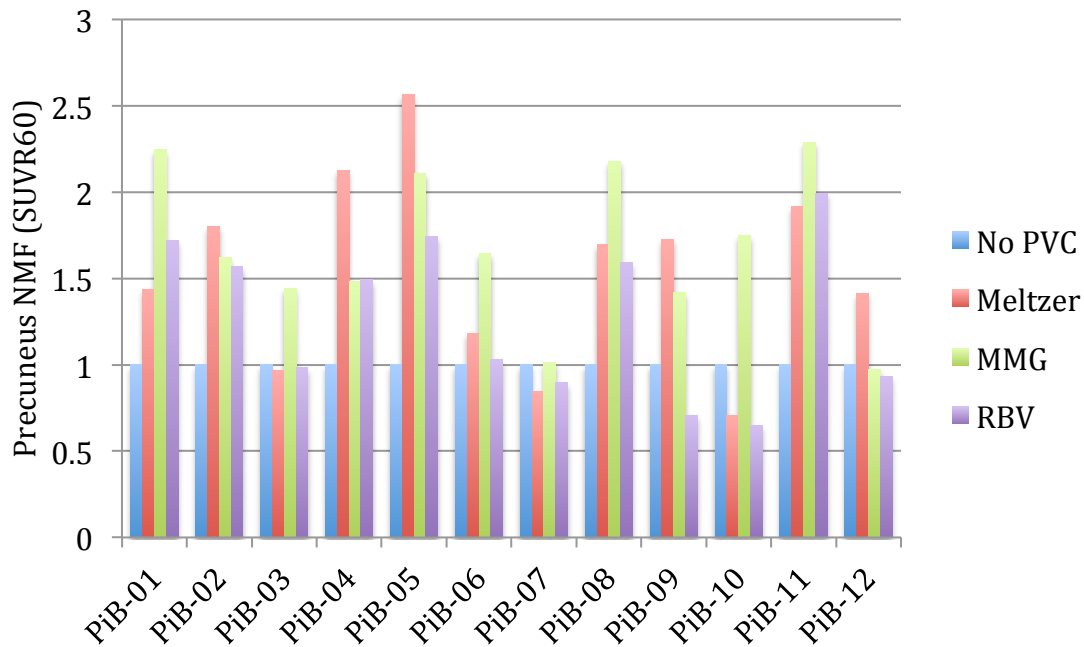


**Figure 25 Noise magnification factors for precuneus SUVR60 outcome measures across PVC techniques.** The largest NMFs were generated by the MMG method in 7 cases and by the Meltzer method in 5 cases.

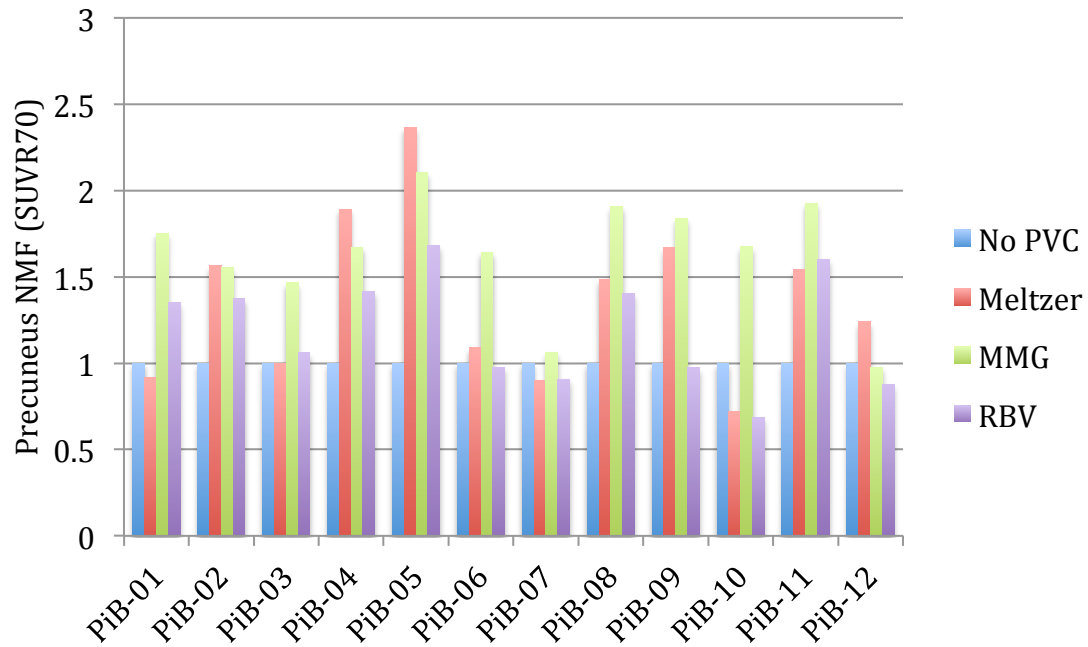


**Figure 26 Noise magnification factors for precuneus SUVR70 outcome measures across PVC techniques.** The largest NMFs were generated by the MMG method in 8 cases and by the Meltzer method in 4 cases.

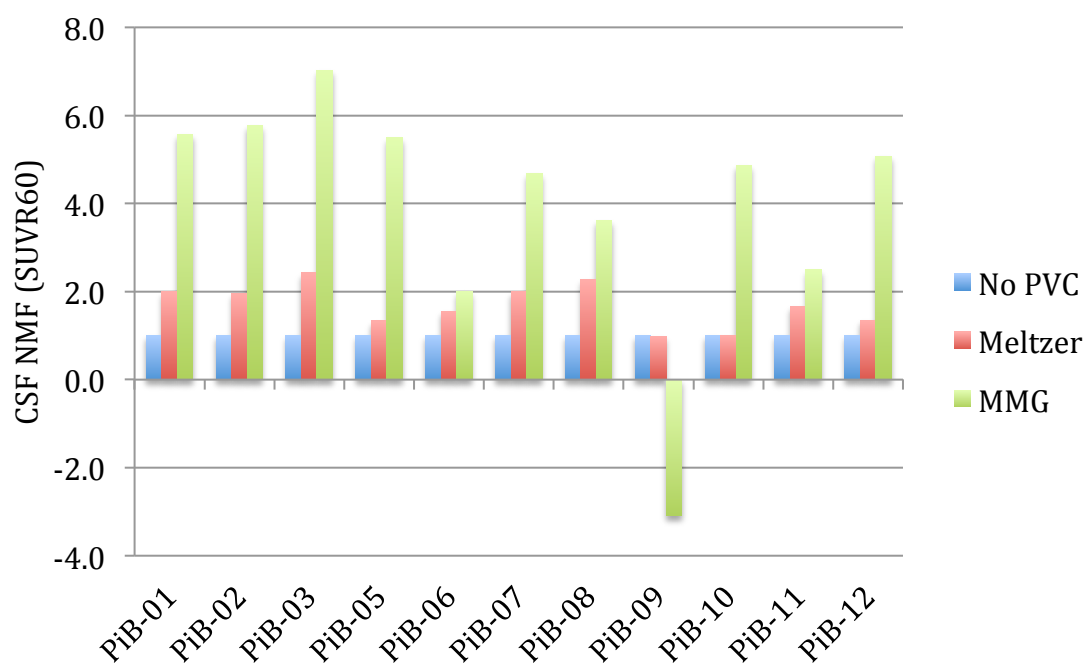


**Figure 27 Noise magnification factors for ventricular CSF SUVR60 measures across PVC techniques.** Subject PiB-04 was excluded from CSF NMF assessment as the ventricles in the subject were too small to fit a CSF region of interest. Across all subjects the magnitude of the CSF NMF was greater for MMG-corrected data than Meltzer-corrected data. In the single case of subject PiB-09, MMG-correction resulted in a negative CSF NMF of -3.09. CSF NMFs for RBV-corrected data are not shown as the PVC method results in zero voxels outside of the brain parcellation.

### 3.3.3 PiB PET-Postmortem Correlations

Pearson's correlation coefficients between 6-CN-PiB (% Area) and SUVR measures across subjects for the precuneus, frontal cortex, and occipital cortex regions are shown in **Table 6**. In both the precuneus and frontal cortex, all partial volume correction methods actually lowered the correlation between 6-CN-PiB and SUVR, though all correlations remain statistically significant at  $p < 0.05$ . Plots of partial volume-corrected and uncorrected SUVR60 and SUVR70 outcomes versus 6-CN-PiB in the precuneus are shown in **Figures 28** (SUVR60) and **29** (SUVR70). Frontal cortex correlations for SUVR60 and SUVR70 are shown in **Figures 30** and **31**, respectively. 6-CN-PiB measures for the precuneus ranged from 0.25% Area (PiB-03; diagnosed dementia with Lewy bodies) to 19.51% (PiB-23, diagnosed probable AD). 6-CN-PiB measures for the frontal cortex ranged from 0.01% (PiB-03) to 22.40% (PiB-23).

Despite strong linear correlations to 6-CN-PiB, precuneus SUVR outcome measures seem to plateau beyond a 6-CN-PiB % Area of ~10%, for all partial volume correction methods (**Figures 28** and **29**). Subjects affected are PiB-01, PiB-05, PiB-09, and PiB-12, all diagnosed with probable AD. A similar plateau is seen in frontal cortex outcome measures, but at an even lower % Area of ~5% (**Figures 30** and **31**).

In the occipital cortex, RBV-corrected outcomes had a higher correlation with 6-CN-PiB % Area than uncorrected outcome measures. However, 6-CN-PiB histofluorescence measured in the occipital cortex as much lower across subjects than that measured in the precuneus and frontal cortex. 6-CN-PiB % Area for the

occipital ranged from 0.02% Area (PiB-03) to 5.57% (PiB-23). Correlations to SUVR60 and SUVR70 across PVC methods for the occipital cortex are shown in **Figures 32 and 33**.

**Table 6** Pearson Correlations to 6-CN-PiB (% Area) across all subjects ( $n=12$ ) for all SUVR and PVC methods.

	Precuneus		Frontal Cortex		Occipital Cortex	
	SUVR60	SUVR70	SUVR60	SUVR70	SUVR60	SUVR70
No PVC	0.920	0.923	0.737	0.741	0.846	0.835
Meltzer	0.852	0.859	0.661	0.668	0.825	0.811
MMG	0.868	0.872	0.721	0.724	0.817	0.795
RBV	0.885	0.890	0.723	0.729	0.866	0.855

All correlations are statistically significant at  $p < 0.05$ .



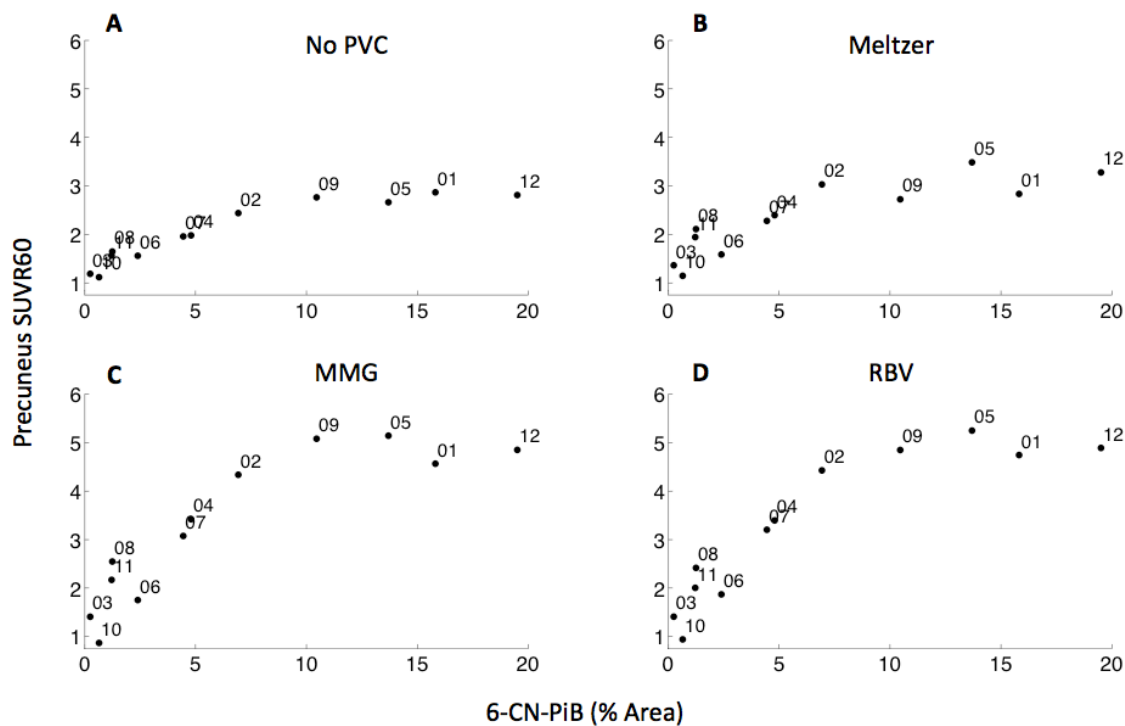


**Figure 28 Correlations between 6-CN-PiB % area and SUVR60 in the precuneus across subjects and partial volume correction methods.** Plots for uncorrected SUVR (A), Meltzer-corrected SUVR (B), MMG-corrected SUVR(C), and RBV-corrected SUVR (D) are shown. Subject PiB identifiers (**Table 7**) are overlaid onto each plot. Pearson's correlation is greatest for uncorrected SUVR (0.920) followed by RBV-corrected (0.885), MMG-corrected (0.868), and Meltzer-corrected (0.852). All correlations are statistically significant at  $p < 0.05$  despite the SUVR value seeming to plateau relative to 6-CN-PiB % Area at ~10%.

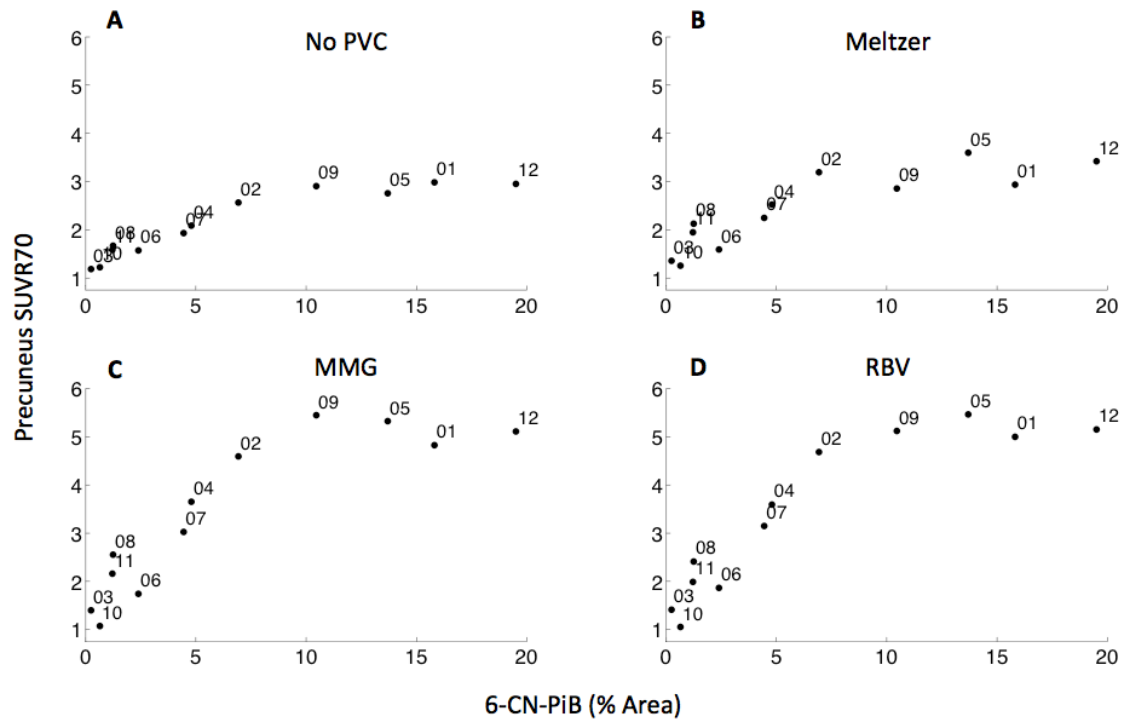


**Figure 29 Correlations between 6-CN-PiB % Area and SUVR70 in the precuneus across subjects and partial volume correction methods.** Plots for uncorrected SUVR (A), Meltzer-corrected SUVR (B), MMG-corrected SUVR(C), and RBV-corrected SUVR (D) are shown. Subject PiB identifiers are overlaid onto each plot. As in the case of SUVR60, Pearson's correlation is greatest for uncorrected SUVR (0.923) followed by RBV-corrected (0.890), MMG-corrected (0.872), and Meltzer-corrected (0.859). As in the case of SUVR60, SUVR70 data seems to plateau relative to 6-CN-PiB % Area at ~10%.

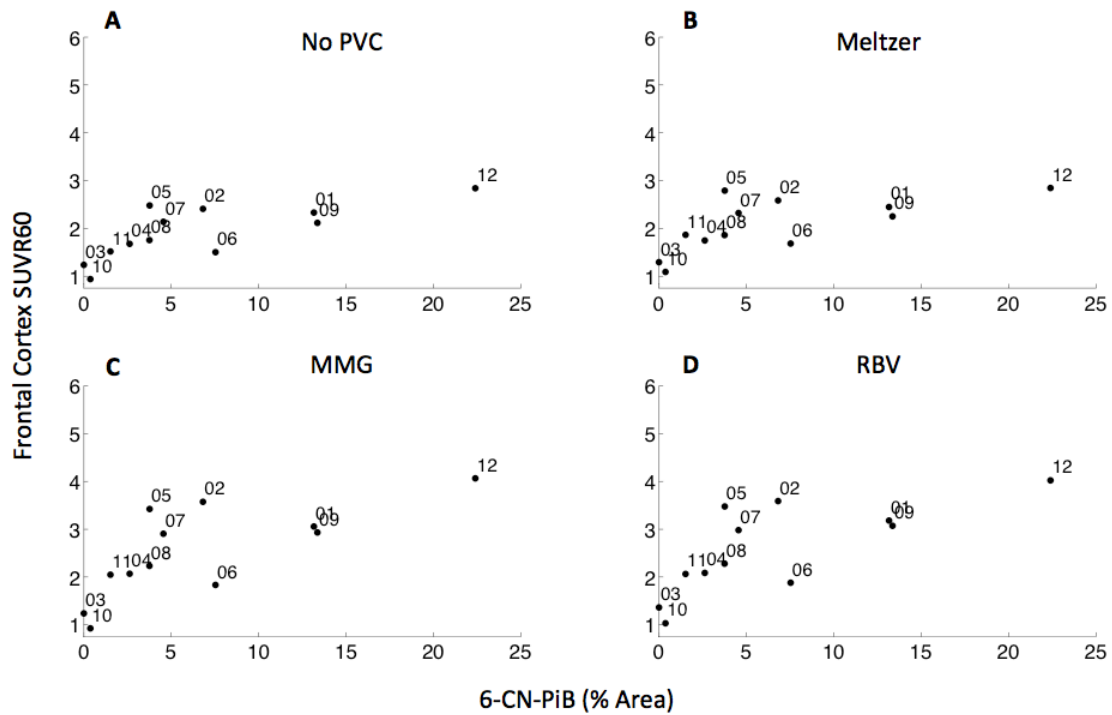


**Figure 30 Correlations between 6-CN-PiB % Area and SUVR60 in the frontal cortex across subjects and partial volume correction methods.** Plots for uncorrected SUVR (A), Meltzer-corrected SUVR (B), MMG-corrected SUVR(C), and RBV-corrected SUVR (D) are shown. Subject PiB identifiers (**Table 7**) are overlaid onto each plot. Similar to precuneus data, Pearson's correlation for the frontal cortex is greatest for uncorrected SUVR (0.737) followed by RBV-corrected (0.723), MMG-corrected (0.721), and Meltzer-corrected (0.661). However, all correlations are significant at  $p < 0.05$ . SUVR60 frontal cortex data seems to plateau at a 6-CN-PiB % Area of ~5%.

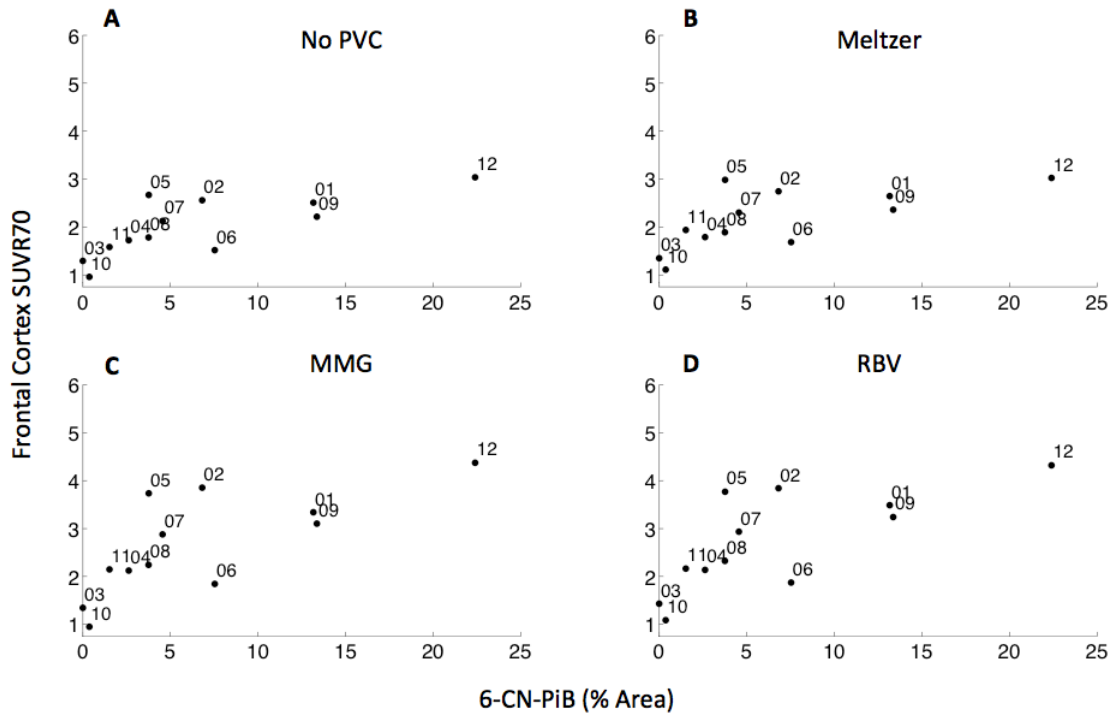


**Figure 31 Correlation between 6-CN-PiB % Area and SUVR70 in the frontal cortex across subjects and partial volume correction methods.** Plots for uncorrected SUVR (A), Meltzer-corrected SUVR (B), MMG-corrected SUVR(C), and RBV-corrected SUVR (D) are shown. As in the case of SUVR60, Pearson's correlation for SUVR70 in the frontal cortex is greatest for uncorrected SUVR (0.741) followed by RBV-corrected (0.729), MMG-corrected (0.724), and Meltzer-corrected (0.668).

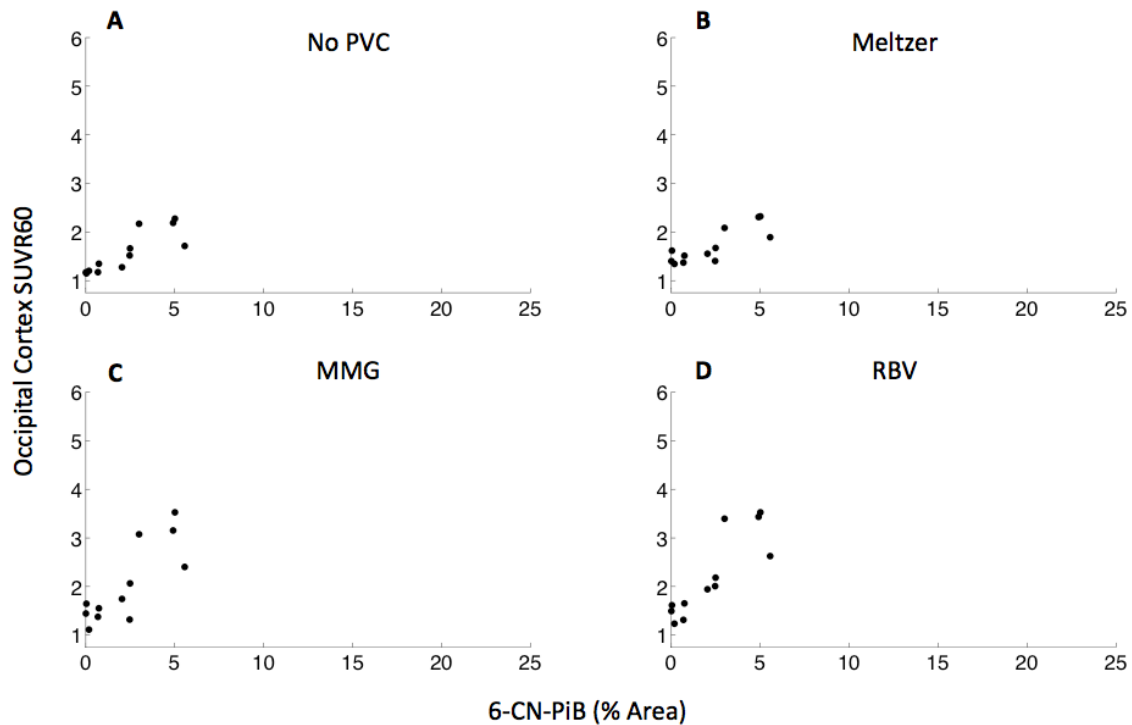


**Figure 32 Correlations between 6-CN-PiB % Area and SUVR60 in the occipital cortex across subjects and partial volume correction methods.** Plots for uncorrected SUVR (A), Meltzer-corrected SUVR (B), MMG-corrected SUVR(C), and RBV-corrected SUVR (D) are shown. Subject PiB identifiers are not overlaid onto the plots. A maximum 6-CN-PiB % Area of 5.57% is seen in PiB-23, relatively little compared to the precuneus and frontal cortex. PiB-16 has a 6-CN-PiB % Area of 5.02%, and PiB-05 has a % Area of 4.92. The maximum correlation to 6-CN-PiB % Area is seen in RBV-corrected data (0.866), followed by uncorrected SUVR60 (0.846), Meltzer-corrected (0.825), and MMG-corrected (0.817).

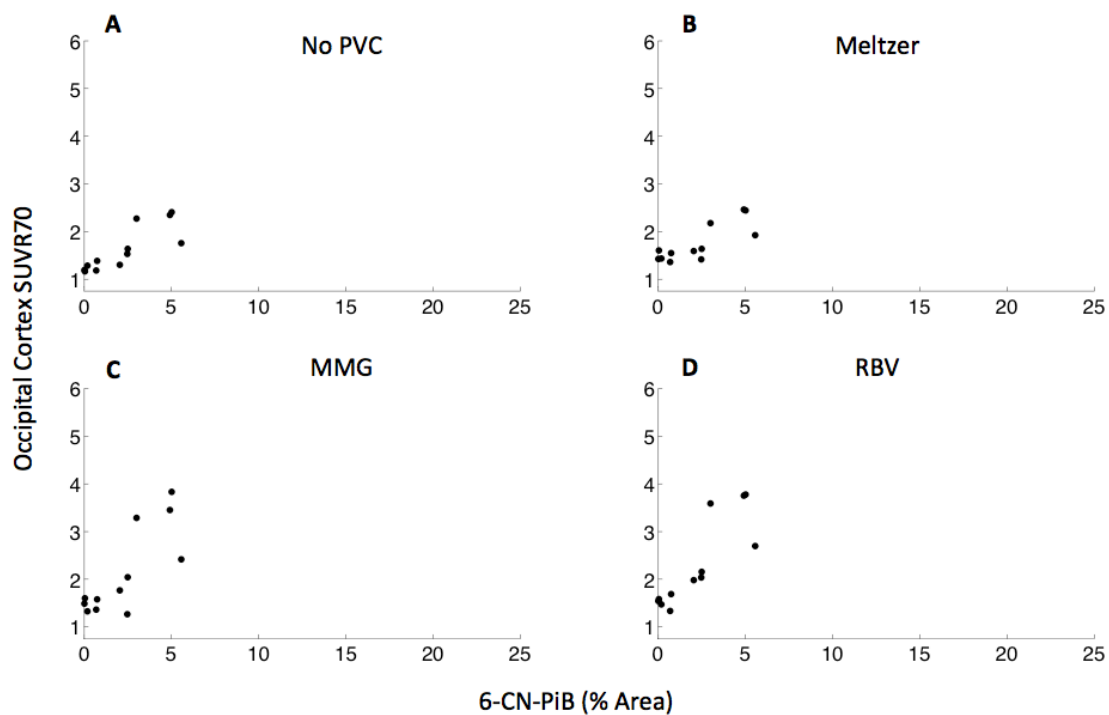


**Figure 33 Correlations between 6-CN-PiB % Area and SUVR70 in the occipital cortex across subjects.** Plots for uncorrected SUVR (A), Meltzer-corrected SUVR (B), MMG-corrected SUVR(C), and RBV-corrected SUVR (D) are shown. Subject PiB identifiers are not overlaid onto the plot. As in the case of SUVR60 occipital cortex outcomes, the maximum correlation to 6-CN-PiB % Area is seen in RBV-corrected SUVRs (0.855), followed by uncorrected SUVR60 (0.835), Meltzer-corrected (0.811), and MMG-corrected (0.795).

### **3.4 Discussion**

#### **3.4.1 Effect of Partial Volume Correction on PiB SUVR**

In this component of this thesis, the impact of three partial volume correction techniques on two PiB PET outcomes measures that are commonly used in clinical research was examined. The noise propagation performance of these partial volume correction techniques was also examined both in brain tissue regions and ventricular CSF. Lastly, the effect of these partial volume correction techniques on correlations between antemortem PET and post-mortem autopsy measures of amyloid load was considered.

The use of the Meltzer partial volume correction technique resulted in approximately 15% increases in precuneus SUVR values. This is in line with a previous study of late-onset AD subjects that found the Meltzer correction technique increased average PiB uptake by approximately 22% [79]. The use of both the MMG and RBV correction methods resulted in ~50% increases in precuneus SUVR values. Thomas et al (2011) [11], found similar increases, between 44% and 56%, in AD subjects after MMG- and RBV-correction.

While multiple studies of partial volume correction in amyloid imaging generally report increases in PiB retention after PVC [11, 77, 79, 90], three subjects in this study had reduced PiB SUVR values in the precuneus after partial volume correction. Application of the Meltzer method to PiB-01 and PiB-09 resulted in small decreases in precuneus SUVR60 and SUVR70, and in PiB-10, the use of both MMG and RBV correction methods resulted in relatively large reductions in precuneus SUVR60 and SUVR70. The reductions seen in PiB-01 and PiB-09 are due

to the Meltzer method having a larger impact on the cerebellar reference region than the precuneus. The Meltzer method increased cerebellar GM SUV from 0.93 to 1.15 in PiB-01 and 0.75 to 0.94 in PiB-09. These ~25% increases were greater than the ~22-23% increases in precuneus SUV, resulting in reduced Meltzer-corrected SUVR values. This is a similar phenomenon to that reported by Su et al (2015) [90], in which increased cerebellar cortex intensities from Meltzer correction method resulted in lower putamen  $BP_{ND}$  values. Both PiB-01 and PiB-09 were diagnosed with probable AD and substantial cerebellar atrophy is apparent in both antemortem MR images.

The reductions in precuneus SUVR values for PiB-10 after both MMG- and RBV-correction are likely due to PiB-10 being a normal control subject with low specific binding of PiB in grey matter. Non-specific activity from white matter is relatively higher and spills over into the precuneus grey matter space. Both the MMG and RBV methods correct for the partial volume effect from white matter, so activity assumed to originate from white matter is removed from grey matter voxels in the ROI, resulting in lower grey matter activity.

These cases highlight the fact that the impact of any partial volume correction technique is highly region and subject specific. MR image segmentation or parcellation, PET-to-MR image coregistration, and region of interest placement must all be performed consistently and cautiously when applying any partial volume correction technique. Even if performed ideally, noise magnification may confound potential findings.



### 3.4.2 PiB SUVR-Postmortem Correlations and Plateauing

A potentially confounding factor to evaluating the effect of PVC techniques on correlations between postmortem and antemortem measures of amyloid load, and perhaps the most interesting finding of this study, is the plateauing of antemortem measures of PiB retention. Indeed, a previous study, which was preliminary work for this thesis, found that application of the Meltzer PVC method to PiB SUVR data for 8 of the 12 subjects reported in this thesis work improved antemortem PiB SUVR and postmortem 6-CN-PiB % area correlations [91]. No plateauing of SUVR relative to 6-CN-PiB was observed. Another previous study of 6 subjects relating antemortem PiB SUVR to postmortem measures of amyloid load also observed no plateauing of PiB SUVR [66]. However, none of the 6 subjects in that study were diagnosed with Probable AD. In the current thesis work, both SUVR60 and SUVR70 seemed to plateau at a 6-CN-PiB % area measure of ~10% for the precuneus and ~5% for the frontal cortex, regardless of PVC technique.

To evaluate the effect of PVC techniques on antemortem-to-postmortem correlations of amyloid load independent of this plateauing phenomenon, Pearson correlations were calculated for the six subjects with the lowest levels of 6-CN-PiB % Area for both SUVR measures and all PVC techniques. Correlations were then calculated for the seven lowest-6-CN-PiB % area subjects, then eight lowest, nine lowest, and so on until all subjects were included. Pearson correlations based on precuneus measures for these lowest-6-CN-PiB subgroups are presented in **Table 7**. The correlation between uncorrected SUVR and 6-CN-PiB % area increased with the size of the subgroup until a peak Pearson correlation of 0.968 for SUVR60 and 0.975

for SUVR70 at a subgroup  $n$  of 9. The greatest 6-CN-PiB % area observed in this subgroup was 10.46%, equivalent to the observed plateauing of SUVR at a 6-CN-PiB measure of  $\sim 10\%$  in **Figures 28** and **29**. No PVC method improved the correlation between PiB SUVR and 6-CN-PiB % area for any group size, with the exception of the RBV method in the subgroup of  $n=10$ . Spearman's rank-order correlations were also assessed for lowest-6-CN-PiB % area subgroups, with similar results (**Table 8**). No PVC method improved Spearman's rho between PiB SUVR and 6-CN-PiB % area for the precuneus, with the exception of the MMG and RBV methods applied to SUVR60 data for the  $n=10$  subgroup.

While each PVC method tested substantially increased precuneus PiB SUVR values on average, each method also reduced the correlation of precuneus SUVR to 6-CN-PiB % area across all subjects and across lowest-6-CN-PiB % area subgroups. These reductions in correlation are likely due to the noise magnification of each PVC method. A previous study that applied the Müller-Gärtner method to longitudinal PiB PET data found that increased variance caused by the PVC method offset the benefits of increased accuracy [92]. Variability is of particular concern in longitudinal studies as measured increases in amyloid deposition are very small, and any increase in variability may mask actual changes in A $\beta$  load. In this study, a similar tradeoff between increased PiB retention and increased variability is seen.

**Table 7** Pearson correlation coefficients between precuneus PiB SUVR for all partial volume correction methods and 6-CN-PiB % area, according to lowest-6-CN-PiB % area subgroups of varying sizes.

<i>n</i> of Lowest-6-CN-PiB Subgroup	Greatest 6-CN-PiB % area in Subgroup	SUVR60				SUVR70			
		No PVC	Meltzer	MMG	RBV	No PVC	Meltzer	MMG	RBV
6	4.45	0.867	0.671	0.740	0.830	0.865	0.660	0.744	0.835
7	4.80	0.905	0.774	0.839	0.894	0.920	0.793	0.856	0.905
8	6.93	0.952	0.885	0.915	0.946	0.961	0.899	0.927	0.953
9	10.46	0.968	0.833	0.943	0.948	0.975	0.850	0.955	0.955
10	13.70	0.937	0.897	0.933	0.945	0.938	0.905	0.935	0.948
11	15.82	0.941	0.842	0.892	0.913	0.942	0.849	0.896	0.917
12	19.51	0.920	0.852	0.868	0.885	0.923	0.859	0.872	0.890

**Table 8** Spearman rank-order correlation coefficients between precuneus PiB SUVR for all partial volume correction methods and 6-CN-PiB % area, according to lowest-6-CN-PiB % area subgroups of varying sizes.

<i>n</i> of Lowest-6-CN-PiB Subgroup	Greatest 6-CN-PiB % area in Subgroup	SUVR60				SUVR70			
		No PVC	Meltzer	MMG	RBV	No PVC	Meltzer	MMG	RBV
6	4.45	0.771	0.771	0.771	0.771	0.829	0.771	0.771	0.771
7	4.80	0.857	0.857	0.857	0.857	0.893	0.857	0.857	0.857
8	6.93	0.905	0.900	0.905	0.905	0.929	0.900	0.905	0.905
9	10.46	0.933	0.902	0.926	0.933	0.949	0.902	0.915	0.933
10	13.70	0.939	0.928	0.946	0.948	0.952	0.928	0.936	0.948
11	15.82	0.954	0.910	0.921	0.928	0.962	0.910	0.913	0.928
12	19.51	0.958	0.923	0.916	0.937	0.965	0.923	0.909	0.937

### 3.4.3 Optimal Method for Partial Volume Correction

In relating the performance of each of the PVC methods in this study, the RBV method seems to be the optimal PVC method. Noise magnification factors within brain tissue regions were consistently lower for RBV-corrected SUVR data than MMG-corrected data, despite both methods resulting in similar increases of SUVR. Further, noise magnification factors in the ventricular CSF resulting from the MMG PVC method ranged from 1.5 to ~5 times greater in magnitude than those resulting from the Meltzer method. In one subject, the CSF NMF based on MMG corrected data was negative, due to a negative average SUVR60 voxel value in the CSF ROI. Both this negative NMF value and the relatively large NMF values across all subjects are partially a result of the subtraction step in the MMG method (**Section 2.2.2**). The voxel-level subtraction of white matter contribution can result in negative voxel values in the final partial volume-corrected PET image. This may lead to increased variation within a region of interest, due to voxels spanning both positive and negative values, and an overall negative outcome measure, as in the case of the CSF SUVR60 value for subject PiB-09.

Considering correlation to 6-CN-PiB % area, RBV-corrected SUVR values correlated more highly than both Meltzer-corrected and MMG-corrected SUVR data across the precuneus, frontal cortex, and occipital cortex regions. Thomas et al (2011) also found the RBV method to be superior to the MMG partial volume correction method, as MMG-correction overestimated amyloid deposition in the hippocampus, and concluded that PVC should be used as it may lead to improved diagnostic group discrimination and longitudinal tracking. However, in the current

study, while the RBV method outperformed the MMG and Meltzer partial volume correction methods, its application resulted in lower, though still significant, correlations between PiB SUVR and 6-CN-PiB % area.

#### **3.4.4 Conclusion**

The impact of partial volume correction is highly region- and subject-specific. The RBV PVC method is the best performing PVC method in correlating antemortem PiB SUVR to postmortem 6-CN-PiB % area, relative to the MMG and Meltzer PVC methods. However, no PVC method improved the correlation between PiB SUVR and 6-CN-PiB % area.

Perhaps the most interesting finding of this study is the plateauing of observed SUVR outcome measures relative to 6-CN-PiB % Area. This study does confirm that the plateauing is not a result of partial volume errors. More work needs to be done to investigate the relationship between PiB PET and postmortem measures of amyloid load.

# Chapter 4

## Performance of Analytic Methods in Measuring PiB PET Change

This chapter describes the assessment of performance of commonly used simplified reference-tissue quantification methods in measuring baseline-to-follow-up PiB PET change across clinical subgroups.

### 4.1 Introduction

#### 4.1.1 Comparison of Analytic Methods for PiB PET

A number of studies have compared the performance of analysis methods in measuring PiB PET specific binding on a cross-sectional basis. Price et al (2005) [93] tested multiple arterial input analysis methods on PiB PET data from 5 controls, 5 MCI, and 5 AD patients. The study found a two-tissue compartment four-parameter model best described both target tissue and reference tissue PiB kinetics relative to other compartmental models. The cerebellum was chosen as a reference region due to it being free of fibrillar A $\beta$  plaques in studies of AD. Interestingly, a two-tissue compartment four-parameter model described the cerebellum better than a one-tissue compartment two-parameter model. This suggests non-specific binding kinetics are detectable in tissue regions lacking amyloid plaques. Price et al (2005) also found the Logan graphical method with arterial input to perform well in quantifying PiB retention, demonstrating low bias and a strong correlation with the two-tissue compartment four-parameter model across diagnostic groups.

In an extension of Price et al (2005), Lopresti et al (2005) [94] tested multiple simplified reference tissue methods on PiB data from a cohort of 8 control, 10 MCI, and 6 AD patients. Relative to the Logan graphical method with arterial input, Logan with cerebellar reference from 35- to 90-minutes post-injection integration intervals, demonstrated a negative bias, underestimating arterial DVR in low-PiB-binding subjects and even more so in high-PiB-binding subjects. Reference Logan also had the smallest test-retest variability of all methods tested. SUVR measured 40-60 minutes after injection demonstrated a positive bias, overestimating arterial Logan DVR in both low-PiB-binding and high-PiB-binding subjects, but the SUVR measure also resulted in the highest effect sizes for separating control and AD subjects. The SRTM method produced the highest DVR variability in low-PiB-binding subjects and highest test-retest variability (time interval between test-retest scans ranged from 8-28 days) relative to all other methods tested. SRTM also resulted in the smallest effect size in separating control and AD subjects, suggesting SUVR is a superior method for differentiating diagnostic groups. Lopresti et al (2005) speculated the reference Logan method may be an ideal method for tracking small longitudinal changes due to its relatively small test-retest variability.

Yaqub et al (2008) [95] tested the performance of a number of parametric reference tissue methods (performed on a voxel basis rather than regional) on PiB PET data and found SUVR-1 ( $BP_{ND}$  equivalent; **Section 1.1.4.5**) 40-60 minutes after injection to be less biased (measured by linear regression slope) than reference Logan, SRTM, and SRTM2  $BP_{ND}$ , relative to a two-tissue compartment model

measure of  $BP_{ND}$ . However, SUVR 60-90 minutes after injection had a higher correlation. SRTM2  $BP_{ND}$  showed no improvement in correlation with the two-tissue compartment model measure of  $BP_{ND}$  over SRTM.

In order to determine an optimal time window for SUVR in PiB PET studies, McNamee et al (2009) [96] evaluated 5 20-minute post-injection increments (30-50, 40-60, 50-70, 60-80, and 70-90) and 3 30-minute post-injection increments (30-60, 40-70, 50-80, and 60-90) considering correlation to Logan DVR with arterial input and effective contrast between control and AD groups. SUVRs based on earlier time windows generally resulted in worse correlations with arterial Logan than later time windows, but lower biases. Earlier time window SUVRs also resulted in larger effect sizes than later time windows in contrasting AD patients and controls. McNamee et al (2009) found SUVR measures at 40-60 minutes and 50-70 minutes to be optimal in terms of balancing stability, accuracy, and diagnostic group effect size relative to all other windows. Ultimately, the 40-60 minute SUVR proved advantageous over 50-70 minutes in having lower bias and a larger group effect size, but 50-70 minutes was chosen as the optimal SUVR time window for PiB due to its greater stability for high-PiB-binding individuals.

Finally, Tolboom et al (2009) [97] assessed the test-retest variability (same-day test-retest studies) of PiB studies in controls and AD patients using several kinetic models and reference tissue methods SRTM, parametric SRTM2 (voxel-based), and SUVR. Of the reference tissue methods, SRTM had the highest test-retest variability, followed by SUVR, and parametric SRTM2 had the lowest test-retest variability. As a result, Tolboom et al (2009) [97] concluded parametric



SRTM2 is the optimal method for quantifying PiB PET data, particularly in longitudinal studies, as lower test-retest variability allows for better detection of small longitudinal changes.

#### **4.1.2 Assessment of PiB PET Change in Longitudinal Studies**

A number of reference-tissue analysis methods have been used in longitudinal A $\beta$  studies, including the SUVR method [59, 60, 92], the reference Logan graphical analysis method [90, 98], and the SRTM method [98]. However, little work has been done to characterize the performance of these analysis methods on the measurement of longitudinal changes in A $\beta$  PET imaging studies. In the only study of its kind prior to this work, van Berckel et al (2013) measured longitudinal reductions in late-frame SUVR values in AD subjects when little or no change was observed with SRTM2 and reference Logan analyses [98]. Simulations demonstrated that the decline in late-frame SUVR in the AD population could be due to decreases in the uptake rate of the tracer from blood into brain and not due to any change in actual specific binding. van Berckel et al (2013) also found longitudinal change measured by SUVR to be highly dependent on the time frame utilized, and concluded that SUVR should not be used for longitudinal PiB studies, particularly when small changes in specific binding can be expected.

Nevertheless, SUVR is by far the most widely used method in PiB PET as it minimizes the amount of time patients must spend in the scanner, is cost effective, and is computationally simple [99]. 50-70 minute SUVR is the method of choice for both PiB and  $^{18}\text{F}$ -Florbetapir PET data in the Alzheimer's Disease Neuroimaging

Initiative (ADNI), an ongoing longitudinal, multisite study for the development of clinical, imaging, genetic, and biochemical biomarkers for early detection of Alzheimer's disease [100, 101]. However, 60-90 minute SUVR was used to measure PiB PET change in a phase 2 clinical trial of bapineuzumab [102]. In phase 3 trials of bapineuzumab, the SUVR time-frame used to measure PiB PET data is not specified [103].

While compartmental modeling remains the “gold standard” for PiB PET quantification, opinions in the field of amyloid imaging vary on an optimal reference tissue method between SUVR, reference Logan, and SRTM. This has led to difficulty in comparing data across sites in both natural history and treatment studies. One effort to remedy the lack of methodological consensus has been the Centiloid standardization process [104]. The Centiloid process outlines a simple, elegant method for converting any outcome measure for any amyloid radiotracer to a standard Centiloid unit. However, the Centiloid methodology is a linear approach that was developed using 50-70 minute SUVR data, and thus, is based on the assumption that any other analytic method is linearly related to the 50-70 minute SUVR, which may not be true. More work still needs to be done in order to determine the optimal methodology for tracking longitudinal change in PiB PET studies.

## **4.2 Materials and Methods**

The objective of this aspect of the thesis was to evaluate the performance of commonly used reference tissue analysis methods in measuring longitudinal changes of amyloid burden in a unique population of elderly subjects with full dynamic 90-minute baseline and follow-up PiB scans. This study also considers the potential impact of reference region selection, relative tracer delivery between target and reference tissues, and the partial volume effect on measurements of longitudinal change.

### **4.2.1 Subjects**

A total of 48 subjects were recruited prior to this thesis work as part of multiple research studies at the University of Pittsburgh Alzheimer Disease Research Center (ADRC). Image data for all subjects were used in this thesis work with permission from Dr. William Klunk, Co-Director of the ADRC. Participants received an extensive neuropsychiatric evaluation that included a physical exam, neurologic exam, psychiatric interview and neuropsychological assessment, as previously described [93]. The diagnosis of Probable AD or mild cognitive impairment (MCI) was determined by a consensus conference attended by clinical staff, neurologists, psychiatrists, and neuropsychiatrists. Normal controls (NC) underwent full evaluation at the ADRC and scored normally on evaluations. The study participants included 29 subjects classified as NC, 12 with MCI diagnoses, and 7 with probable AD diagnoses. All subjects or their proxy provided informed

consent for both the ADRC and PET protocols. Data from some subject scans have been previously published [93, 94, 96, 105].

#### **4.2.2 MR and PiB PET Imaging**

All subjects underwent baseline and follow-up MR and PiB PET imaging prior to this thesis work within an interval of  $28.6 \pm 10.9$  months (range, 10 – 52 months). MR images were acquired on a 1.5T GE Signa scanner at baseline and follow-up at the University of Pittsburgh MR Research Center. The scan protocol included a T1-weighted volumetric spoiled gradient recalled (SPGR) sequence in the coronal plane (TE/TR = 5/25, flip angle =  $40^\circ$ , NEX = 1, slice thickness = 1.5 mm). MR images were used for co-registration to the PET image and ROI definition.

PiB PET data were acquired with a Siemens/CTI ECAT HR+ scanner in 3D imaging mode, yielding 63 parallel transaxial planes over a 15.2 cm axial FOV. Subjects were administered  $15.1 \pm 1.1$  mCi (10.2 – 16.5 mCi over 20 seconds) of PiB and scanned for 90 minutes (34 frames:  $4 \times 15$  sec,  $8 \times 30$  sec,  $9 \times 60$  sec,  $2 \times 180$  sec,  $8 \times 300$  sec,  $3 \times 600$  sec). Data was reconstructed with filtered back-projection reconstruction (Fourier rebinning/2D back-projection) and PET data correction included scanner normalization, dead-time, attenuation, scatter, and radioactive decay. The final reconstructed image resolution was  $6.46 \times 6.09 \times 5.71$  mm FWHM.

#### **4.2.3 PiB PET Motion Correction and Registration**

As part of this thesis work, PET images were visually inspected for inter-frame motion by generating a contour on a relatively high-signal, low-duration

early-scan frame (~7-8 min) delineating ventricles and CSF from brain tissue. These early-scan frames were typically more reflective of blood flow than later frames that are more reflective of specific binding. The contour was generated in a version of ROItool (CTI PET Systems, Knoxville, Tennessee, United States) modified by staff at the University of Pittsburgh PET Center prior to this thesis work. The contour was then viewed across all frames to assess any changes in subject position due to rotations or shifts in head placement. If frame-to-frame motion was observed, automated registration methods previously implemented at University of Pittsburgh PET Center [106, 107] were used to align frames as part of this thesis work.

Baseline MR-PET image registration was also performed using the same automated registration techniques, and follow-up MR and PET images were registered to baseline MR images.

#### **4.2.4 Region of Interest Generation**

Multiple cortical and subcortical regions of interest (ROIs) spanning the brain were subsequently hand-drawn on the co-registered MR images for sampling of the PET data using ROItool software. ROIs drawn include the anterior cingulate gyrus (ACG), anterior ventral striatum (AVS), frontal cortex (FRC), lateral temporal cortex (LTC), parietal lobe (PAR), precuneus (PRC), subcortical white matter (SWM), and cerebellar GM (CER). A global region (GBL) was generated by combining 5 cortical and 1 subcortical regions: ACG, FRC, LTC, PAR, PRC, and AVS. The ROI generation was performed by multiple staff members at the University of Pittsburgh PET Center using common anatomic criteria and ROI shapes to ensure high inter-

rater reliability [108]. Hand-drawn ROIs are shown on MR and PiB PET images in **Figure 34**. Regional time-activity curves were then generated by sampling the dynamic PiB PET data with hand-drawn ROIs using ROItool.

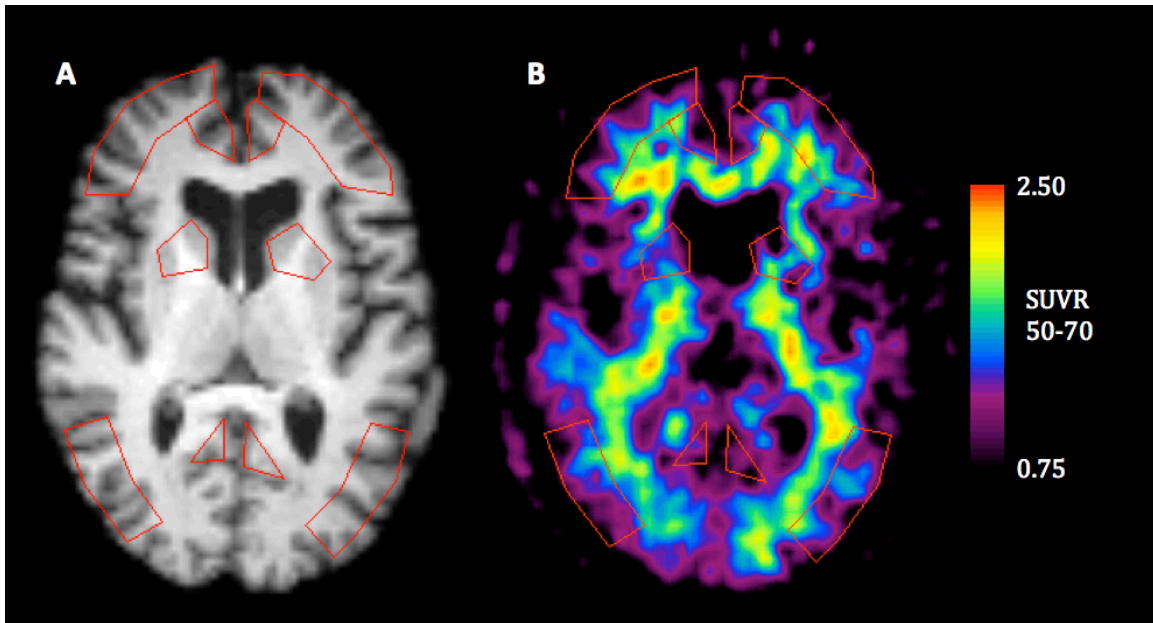


**Figure 34** Regions of interest hand-drawn in ROItool overlaid on a MR image and SUVR PiB PET image for a cognitively normal control subject. Regions of interest were drawn on the (A) MR image and then transferred to the (B) PET image after registration of the PET to MR image.

#### 4.2.5 Time-Activity Curve Smoothing

To lessen the influence of noise on outcome measures, particularly noise in the relatively low-activity CER ROI, time-activity curves were smoothed as part of this thesis work using the “smooth” function in the Matlab Curve Fitting Toolbox (Matlab and Curve Fitting Toolbox Release 2014a, The MathWorks, Inc., Natick, Massachusetts, United States). The robust local regression smoothing method, “rloess”, in which outliers were assigned lower weight and data outside six mean absolute deviations were assigned zero weight [109], with a neighborhood of nine points was utilized. To avoid influencing the peak measured activity, only data five minutes beyond the time of injection was smoothed. **Figure 35** shows a time-activity curve before and after smoothing.

#### 4.2.6 PiB PET Quantification

Smoothed time-activity data were analyzed using SRTM2, reference Logan, and SUVR approaches. The hand-drawn cerebellar GM ROI was used as the reference tissue in all methods.

SRTM2 was applied to the full 90-minute dynamic PET data. Regional time-activity data was first processed using SRTM in PMOD 3.510 software (PMOD Technologies Ltd., Zurich, Switzerland), generating  $R_1$ ,  $BP_{ND}$ , and  $k_2'$  regional values. Regional  $k_2'$  values were subsequently averaged over the six regions constituting the GBL region: ACG, AVS, FRC, LTC, PAR, and PRC.  $k_2'$  was constrained to this average value on an individual subject basis in the application of SRTM2, which was also performed in PMOD 3.510 software to generate regional and GBL SRTM2  $BP_{ND}$  and

$R_1$  values. An SRTM2 DVR outcome measure of PiB retention was calculated as  $DVR = BP_{ND} + 1$ . SRTM2  $R_1$  values were used to evaluate relative tracer delivery. It has been previously shown by Chen et al (2015) that SRTM2  $R_1$  is an accurate and robust measure of relative blood flow [110].

Reference Logan graphical analyses (no  $k_2'$  constraint) were applied to 35 to 90-min integration intervals using in-house software developed by staff at the University of Pittsburgh PET Center. The Logan DVR outcome measure was derived as the slope from linear regression of the Logan graphical variables using CER as the reference.

Regional SUV values were determined over three time intervals – 40-60 minutes (SUV60; 4 × 5-minute frames), 50-70 minutes (SUV70; 2 × 5-minute, 1 × 10-minute frames), and 60-90 minutes (SUV90; 3 × 10-minute frames) – by scaling averaged regional radioactivity concentrations over the time interval to injected radioactivity dose and body mass. Regional SUVR was calculated over the same 40-60 minute (SUVR60), 50-70 minute (SUVR70), and 60-90 minute (SUVR90) time intervals by dividing the region of interest SUV by the CER SUV over the same time interval.



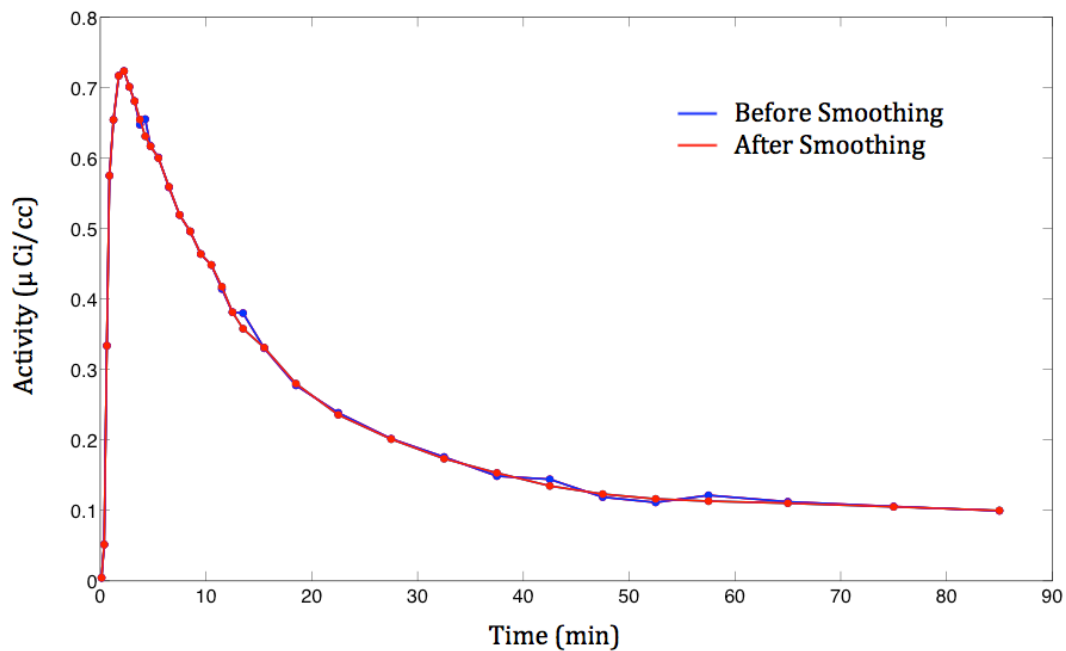


**Figure 35 Cerebellar reference region time-activity curve sampled from an Alzheimer's disease patient before smoothing and after smoothing.** Note slight increases in radioactivity during the washout phase at 45 minutes and 55 minutes are removed after smoothing.

#### 4.2.7 Statistical Analysis

The rate of change, or change per annum, in PiB retention was calculated for each individual as the difference normalized to years between scans: (follow-up value – baseline value)/(days between scans/365).

Subjects were classified as PiB-negative [PiB(-)] or PiB-positive [PiB(+)] based on GBL SUVR70 values determined at baseline and follow-up. A GBL SUVR70 cut-off value of 1.51 was determined using a sparse k-means clustering and resampling classification method applied to data acquired in 62 NC subjects [111].

The Mann-Whitney U Test was used to evaluate significant differences between group change and negative control (NC(-)) change. The Mann-Whitney U Test was also used to evaluate significant differences between group changes in the SRTM2  $R_1$ . The Wilcoxon signed rank test was used to evaluate significant differences between baseline and follow-up measures and change per annum measured by different PiB PET analysis approaches. To evaluate the influence of white matter and cerebellar GM on changes measured for the GBL ROI, correlations between GBL measures and SWM and CER measures were evaluated by Spearman's rho and Pearson correlation coefficient. Differences and correlations were deemed significant at  $p < 0.05$ .

Data are presented as mean  $\pm$  standard deviation unless otherwise noted, and standard deviation is used as the measure of variability in change-per-annum measures.

#### 4.2.8 Population Trajectory Modeling

To evaluate the potential influence of analytic method on natural history studies of AD, baseline-to-follow-up average measures (SUVR and DVR) were plotted against change-per-annum outcome measures ( $\Delta$ SUVR/year and  $\Delta$ DVR/year). A number of model curves were fit to this data in order to characterize the relationship between measured rate of change and measured amyloid load. Models included a two-parameter linear function

$$y = a(x) + b , \quad (39)$$

a two-parameter function with one exponent

$$y = a - e^{b(x)} , \quad (40)$$

a three-parameter quadratic function

$$y = a(x^2) + b(x) + c , \quad (41)$$

a three-parameter Gaussian function

$$y = ae^{\left(-\frac{(x-b)^2}{2c^2}\right)} , \quad (42)$$

and a four-parameter function with two exponents

$$y = ae^{b(x)} + ce^{d(x)} . \quad (43)$$

In each function,  $y$  is either  $\Delta$ SUVR/year or  $\Delta$ DVR/year, and  $x$  is SUVR or DVR.  $a$ ,  $b$ ,  $c$ , and  $d$  are each model-specific parameters. Parameter estimates were obtained using the “nlinfit” function in Matlab, which fits data using the Levenberg-Marquardt nonlinear least squares algorithm [112]. The performance of different models was evaluated using the corrected Akaike information criteria ( $AIC_c$ ) that, in the case of least-squares estimation, is based on the residual sum of squares ( $SSQ$ ), number of data points ( $n$ ) and fit parameters ( $K$ ) [113, 114]:

$$AIC_C = n \ln \left( \frac{SSQ}{n} \right) + 2K + \frac{2K(K+1)}{n-K-1} . \quad (42)$$

Lower  $AIC_C$  values indicate better fits.

### 4.3 Results

**Table 9** contains subject characteristics, including age, gender, mini-mental state exam (MMSE) score, and PiB status classification. Twenty-four percent of the NC subjects, 75% of the MCI subjects, and 100% of the AD subjects were classified as PiB(+) at baseline. An additional 17% of NC subjects were classified as converters or NC(-/+), being PiB(-) at baseline and PiB(+) at follow-up. The remaining subjects' PiB status remained the same between serial scans.

**Table 9** Demographics of subjects with baseline and follow-up PiB PET scans.

Diagnostic Group	<i>n</i>	Age at baseline (yrs)	Gender	MMSE at baseline	Follow-up Interval (mo)	PiB(+) at baseline, <i>n</i> (%)
NC	29	73 ± 9	13 M / 16 F	29 ± 1	32.5 ± 8.9	7 (24%)*
MCI	12	71 ± 7	6 M / 6 F	28 ± 1	23.9 ± 12.4	8 (75%)
AD	7	68 ± 9	5 M / 2 F	24 ± 4	20.5 ± 9.3	7 (100%)

MMSE = Mini-mental State Examination

\* Five NC subjects converted from PiB(-) at baseline to PiB(+) at follow-up, who were designated as converters NC(-/+).

#### 4.3.1 Assessment of Longitudinal Change

PET outcome measures for the GBL region at baseline and follow-up, and the corresponding annual change measures, are presented in **Table 10**. Boxplots of GBL region change per annum for different diagnostic and PiB status groups are presented in **Figure 36**.

**AD Group.** In the AD group, all outcome measures were relatively stable over time (average change for annum for SUVR60: 0.012; SUVR70: 0.024; Logan DVR: 0.009; and SRTM2 DVR: -0.001), with the exception of SUVR90, which measured a significant increase relative to NC(-) subjects of  $0.069 \pm 0.077$  (**Figure 36**).

**MCI(+) Group.** All three SUVR time intervals examined measured significant annual increases in MCI(+) subjects relative to NC(-) subjects with annualized increases of 0.068, 0.091, and 0.114 SUVR for SUVR60, SUVR70, and SUVR90, respectively (**Figure 36**). SUVR90 measured the highest average change and highest variability in change over time, as in the case of the AD subjects. SRTM2 DVR remained relatively stable longitudinally in MCI(+) subjects, as did Logan DVR, which measured the least change with lowest variability. Despite all three SUVR measures identifying significant increases in this MCI(+) group, only SUVR70 and SUVR90 show a significant change relative to SRTM2 DVR. SUVR60 shows no significant difference relative to SRTM2 DVR.

**NC(+) Group.** As mentioned above, about 10-30% of cognitively normal controls show evidence of significant amyloid deposition. In this study population 24% of cognitively normal controls were PiB(+) at baseline. Annualized changes in

NC(+) outcomes were relatively stable across all methods, with the SRTM2 DVR outcome yielding the lowest average change and variability in change per annum ( $0.004 \pm 0.028$ ). The SUVR90 outcome exhibited the highest change per annum ( $0.041 \pm 0.065$ ), whereas SUVR70 exhibited the highest variability in change per annum ( $0.029 \pm 0.072$ ).

**NC(-/+) Group.** As expected by the definition of the group, significant increases over time were measured by all outcome measures in the NC(-/+) group (SUVR60:  $0.098 \pm 0.036$ ; SUVR70:  $0.105 \pm 0.043$ ; SUVR90:  $0.080 \pm 0.063$ ; Logan DVR:  $0.051 \pm 0.020$ ; and SRTM2 DVR:  $0.071 \pm 0.054$  SUVR or DVR change per annum). Once again SUVR90 measured the highest variability in annual change (**Figure 36**).

**NC(-) Group.** SRTM2 DVR measured the largest increase over time with a larger variability in change than SUVR60, SUVR70, and Logan DVR (**Figure 36**). SRTM2 DVR similarly measured larger change and variability over time than those three measures in MCI(-) subjects. In both PiB(-) groups, Logan DVR measured the smallest change and variability.

**Table 10** Outcome measures and change per annum according to analytic method and group (based on smoothed time-activity curves).

		SUVR60	SUVR70	SUVR90	LoganDVR90	SRTM2DVR90
AD (n=7)	Baseline	2.44 ± 0.20	2.48 ± 0.25	2.41 ± 0.26	2.04 ± 0.13	2.10 ± 0.18
	Follow-up	2.46 ± 0.19	2.52 ± 0.25	2.50 ± 0.28	2.07 ± 0.11	2.11 ± 0.14
	Change/Annum	0.012 ± 0.055	0.024 ± 0.064	0.069 ± 0.077 *	0.009 ± 0.049	-0.001 ± 0.054
MCI(+) (n=8)	Baseline	2.20 ± 0.23	2.26 ± 0.26	2.24 ± 0.29	1.84 ± 0.17	1.91 ± 0.21
	Follow-up	2.32 ± 0.19	2.41 ± 0.21	2.42 ± 0.25	1.89 ± 0.13	1.98 ± 0.16
	Change/Annum	0.068 ± 0.124*	0.091 ± 0.128*	0.114 ± 0.161*	0.032 ± 0.077	0.043 ± 0.112
MCI(-) (n=4)	Baseline	1.23 ± 0.05	1.23 ± 0.06	1.27 ± 0.08	1.13 ± 0.02	1.11 ± 0.02
	Follow-up	1.24 ± 0.08	1.28 ± 0.08	1.27 ± 0.07	1.12 ± 0.05	1.11 ± 0.11
	Change/Annum	0.003 ± 0.056	0.009 ± 0.072	-0.030 ± 0.075	-0.005 ± 0.032	0.021 ± 0.082
NC(+) (n=7)	Baseline	1.78 ± 0.14	1.83 ± 0.16	1.80 ± 0.16	1.49 ± 0.12	1.57 ± 0.17
	Follow-up	1.86 ± 0.21	1.90 ± 0.23	1.89 ± 0.19	1.55 ± 0.14	1.59 ± 0.21
	Change/Annum	0.035 ± 0.063	0.029 ± 0.072	0.041 ± 0.065	0.024 ± 0.033	0.004 ± 0.028
NC(-/+) (n=5)	Baseline	1.46 ± 0.03	1.47 ± 0.03	1.48 ± 0.05	1.27 ± 0.06	1.29 ± 0.10
	Follow-up	1.67 ± 0.07	1.70 ± 0.09	1.66 ± 0.12	1.38 ± 0.06	1.44 ± 0.14
	Change/Annum	0.098 ± 0.036*	0.105 ± 0.043*	0.080 ± 0.063*	0.051 ± 0.020*	0.071 ± 0.054*
NC(-) (n=17)	Baseline	1.19 ± 0.12	1.21 ± 0.14	1.21 ± 0.14	1.10 ± 0.08	1.11 ± 0.11
	Follow-up	1.23 ± 0.14	1.23 ± 0.13	1.23 ± 0.13	1.12 ± 0.10	1.15 ± 0.13
	Change/Annum	0.012 ± 0.020	0.009 ± 0.023	0.009 ± 0.034	0.009 ± 0.014	0.017 ± 0.029

\* p < 0.05 significant difference between change in group and change in NC(-)

† p < 0.05 significant difference between outcome change and SRTM2 change

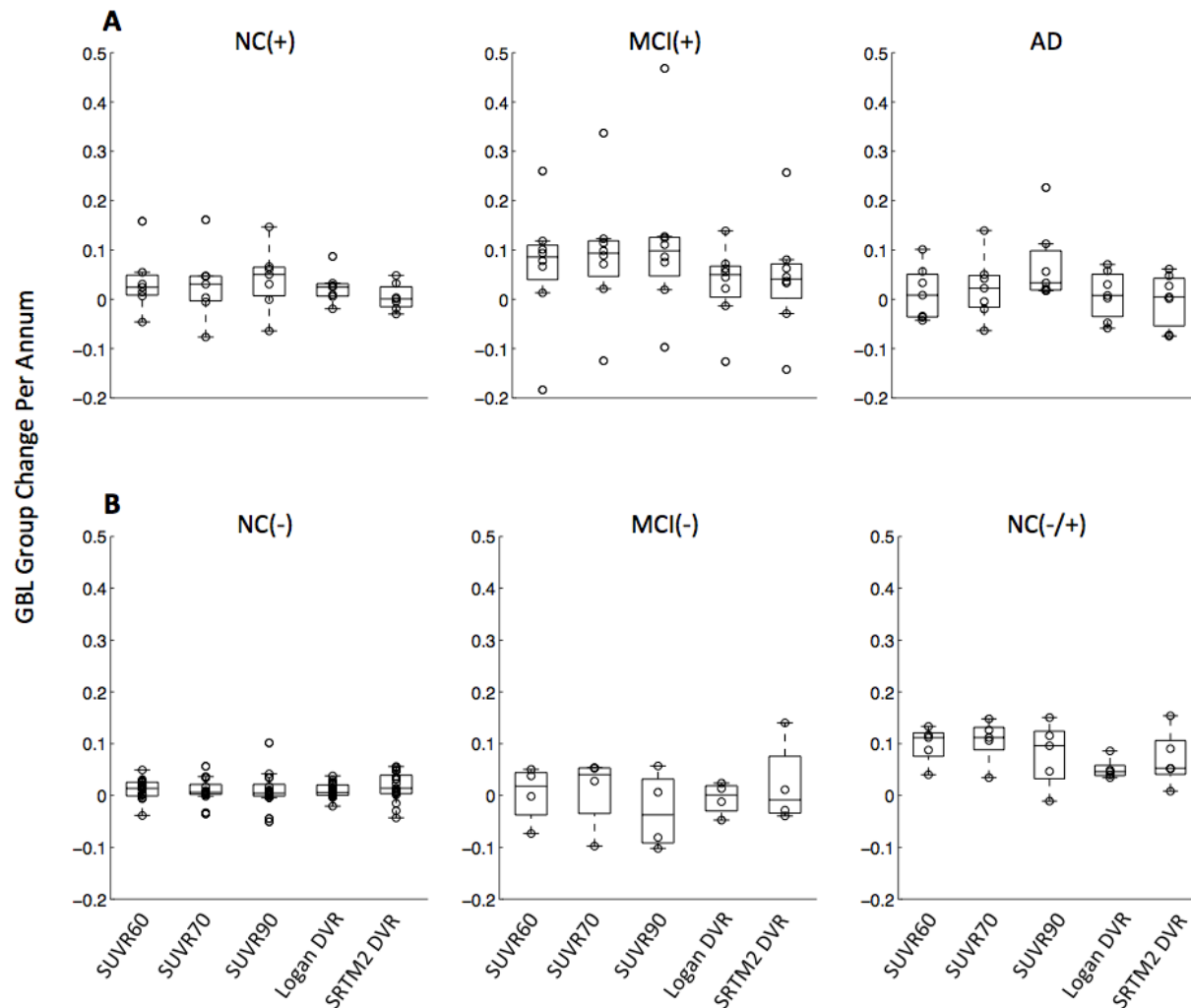


**Figure 36** Box-and-whisker plots of global region group change per annum according to SUVR60, SUVR70, SUVR90, Logan DVR, and SRTM2 DVR. Data for PiB-positive groups at baseline (A) include, from left to right, NC(+), MCI(+), and AD. Data for PiB-negative at baseline (B) include, from left to right, NC(-), MCI(-), and NC(-/+). Results are based on smoothed time-activity curves.



### 4.3.2 Relative Tracer Delivery

At baseline, SRTM2 yielded mean GBL  $R_1$  values of  $0.84 \pm 0.05$  for AD subjects,  $0.85 \pm 0.04$  for MCI(+),  $0.86 \pm 0.05$  for NC(+),  $0.88 \pm 0.06$  for NC(-/+), and  $0.86 \pm 0.05$  for NC(-) subjects (**Table 11**). At follow-up,  $R_1$  values were  $0.80 \pm 0.07$  for AD subjects,  $0.82 \pm 0.06$  for MCI(+),  $0.83 \pm 0.06$  for NC(+),  $0.88 \pm 0.07$  for NC(-/+), and  $0.88 \pm 0.05$  for NC(-) subjects. A significant difference in  $R_1$  (from baseline to follow-up) was only measured in the AD group. NC(-/+) and NC(-) were relatively stable from baseline to follow-up.

### 4.3.3 White Matter and Reference Region Influences

Annual change in the GBL outcomes were found to be significantly correlated with annual change in SWM across all SUVR measures in NC(-) subjects (n=17). Pearson correlation coefficient for NC(-) SUVR60, SUVR70, and SUVR90 were 0.690, 0.729, and 0.727, respectively. The relationship between change per annum in GBL SUVR70 and change per annum in SWM SUVR70 for NC(-) subjects is shown in **Figure 37**. Logan DVR showed no correlation between GBL change and SWM change measures. SRTM2 failed to model SWM time-activity curves with CER input for the majority of the study population, so no correlation could be assessed.

Change in the CER reference region SUV was generally not correlated with GBL change, with the exception of SUVR90 in NC(-/+) and MCI(-) groups, the two groups with lowest sample size and relatively low and negligible specific amyloid signal, respectively.

**Table 11** SRTM2 GBL  $R_I$  values and change per year.

AD	Baseline	$0.84 \pm 0.05$
	Follow-up	$0.80 \pm 0.07$
	% Diff/Year	$-0.030 \pm 0.040^*$
MCI(+)	Baseline	$0.85 \pm 0.04$
	Follow-up	$0.82 \pm 0.06$
	% Diff/Year	$-0.017 \pm 0.024$
NC(+)	Baseline	$0.86 \pm 0.05$
	Follow-up	$0.83 \pm 0.06$
	% Diff/Year	$-0.013 \pm 0.019$
NC(-/+)	Baseline	$0.88 \pm 0.06$
	Follow-up	$0.88 \pm 0.07$
	% Diff/Year	$0.000 \pm 0.012$
NC(-)	Baseline	$0.86 \pm 0.05$
	Follow-up	$0.88 \pm 0.05$
	% Diff/Year	$0.008 \pm 0.014$

\*  $p < 0.05$  significant difference between baseline and follow-up

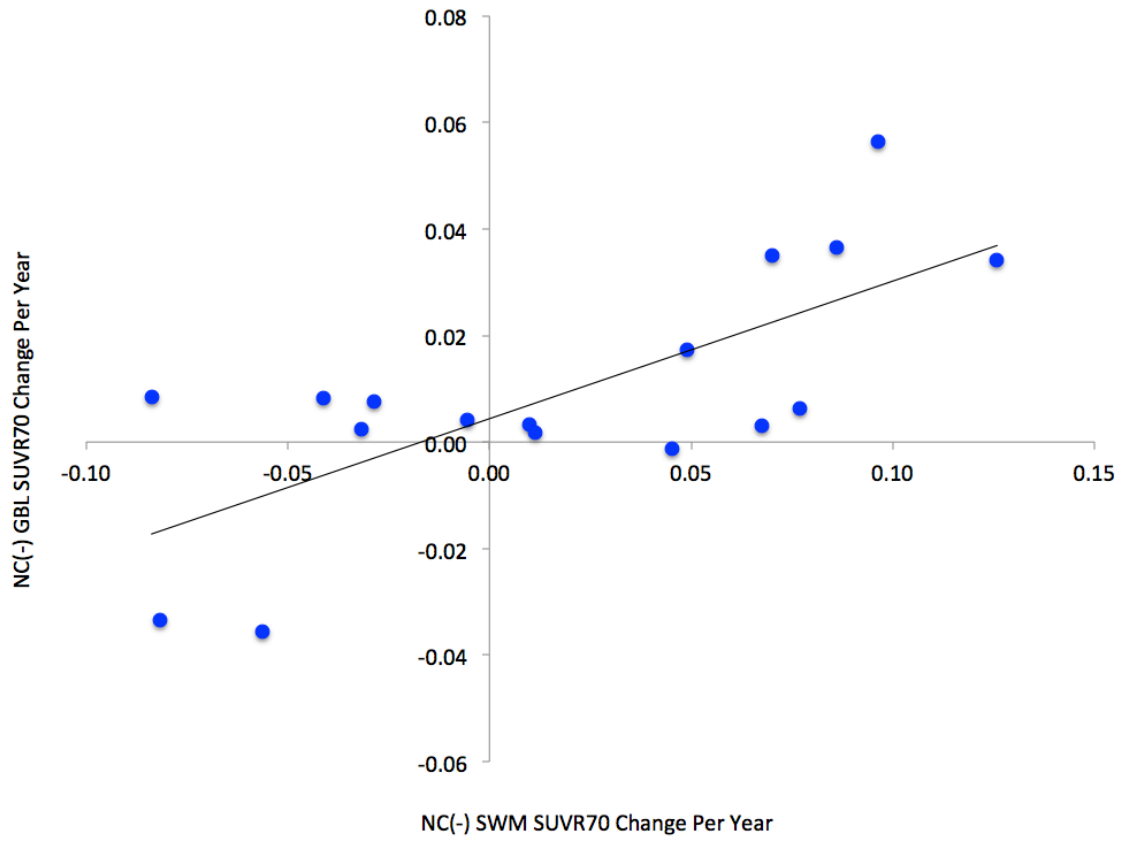


**Figure 37 Relationship between annual change in SWM and change in GBL SUVR70 for NC(-).** A significant correlation is observed with a Pearson correlation coefficient of 0.69 at  $p = 0.002$ , suggesting change in SWM over time influences change in GBL SUVR70 for NC(-) subjects. Results are based on smoothed time-activity curves.

#### 4.3.4 Population Trajectory Modeling

Plots of change per annum versus baseline-to-follow-up average for each outcome measure are shown in **Figure 38**. **Table 12** contains the AIC<sub>C</sub> values for each outcome measure and model fit with 2-parameter linear function, 2-parameter exponential function, and 3-parameter Gaussian function curve fits. SUVR60, SUVR70, and SRTM2 DVR annual change-to-average outcome measure relationships were all best described by the 2-parameter single-exponential model. Logan DVR, however, was best described by the 3-parameter Gaussian function, and SUVR90 was best described by the 2-parameter linear function.

**Table 12** AIC<sub>C</sub> values for model fits between change/annum and average outcome.

Function Fit	SUVR60	SUVR70	SUVR90	Logan DVR	SRTM2 DVR
Linear	-256.656	-248.048	-236.048	-301.984	-264.749
One Exponent	-258.338	-248.992	-235.089	-303.502	-265.235*
Quadratic	-257.048	-246.850	-233.858	-303.303*	-264.671
Gaussian	-257.313	-246.604	-233.800	-303.963	-264.325
Two Exponent	-254.550	-244.479	-231.464	-300.652	-262.268

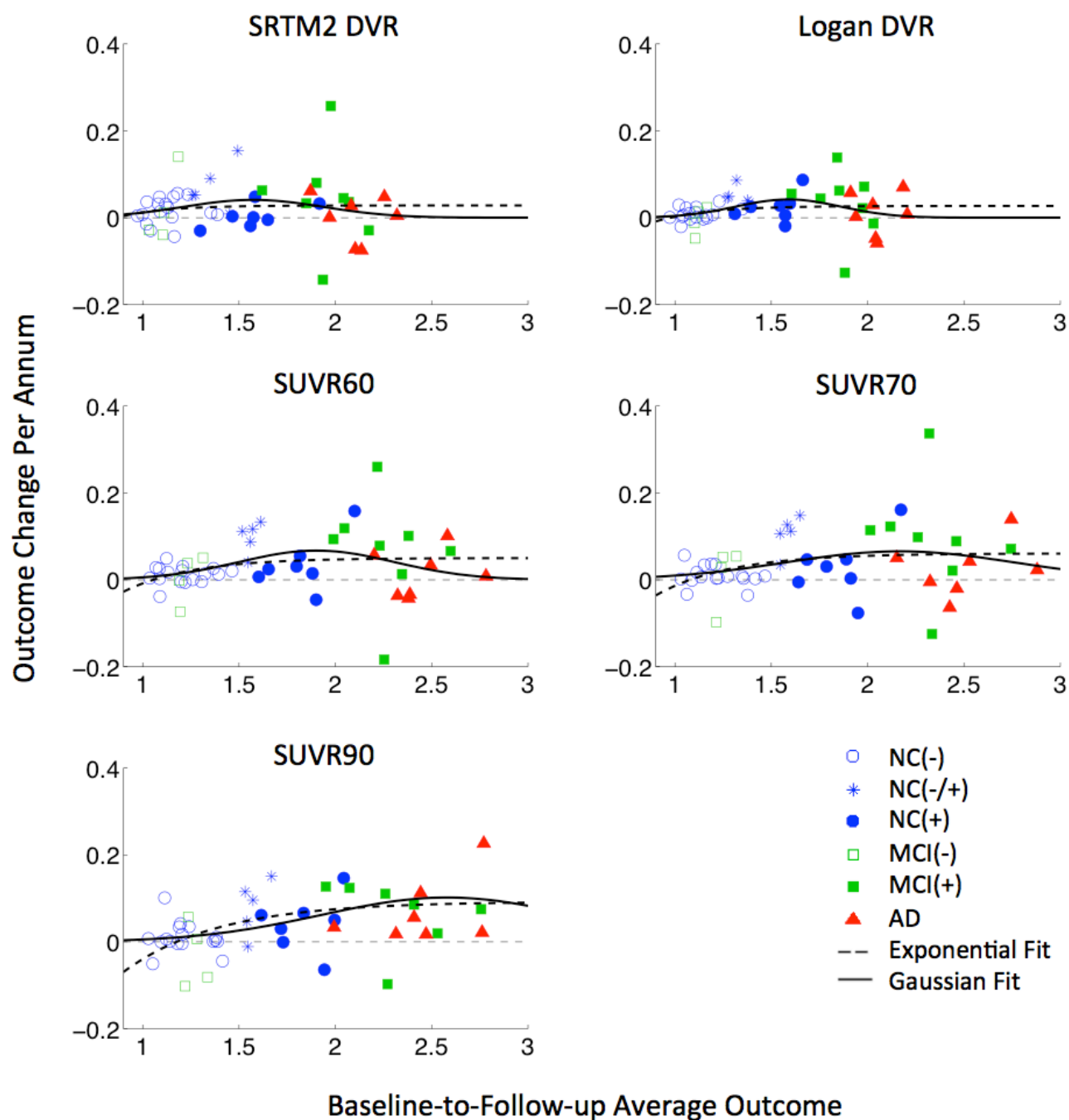


**Figure 38 Model fits for study population data across outcome measures.** SRTM2 DVR, SUVR60, and SUVR70 outcome measures were all best described by the 2-parameter single-exponential model. Logan DVR outcome measures were best fit by the Gaussian model, and SUVR90 data was best fit by a linear function.

## **4.4 Discussion**

This study directly compared longitudinal changes in PiB binding assessed by five different simplified analysis methods with cerebellar GM as reference: SUVR60, SUVR70, SUVR90, reference Logan DVR, and SRTM2 DVR. The SUVR methods resulted in significant differences between change per annum measures in MCI(+) and NC(-) groups, whereas Logan DVR and SRTM2 DVR do not. The SUVR70 and SUVR90 methods yielded change per annum measures significantly greater than change resulting from SRTM2 DVR in the MCI(+) group. In low-PiB-binding subjects (NC(-) and MCI(-)), the SRTM2 DVR method resulted in the highest change-per-annum variability, assessed by standard deviation, whereas Logan DVR results in the lowest change-per-annum variability.

This study also examined the longitudinal relationships between known areas of amyloid deposition and neighboring areas of non-specific binding in subcortical white matter, finding change-per-annum measures evaluated by SUVR methods in low-PiB-binding subjects may be susceptible to changes in non-specific binding in subcortical white matter.

### **4.4.1 Optimal Method for Tracking PiB Change**

The SRTM2 method resulted in mean change-per-annum measures that were not significantly different between the MCI(+) and NC(-) groups. This is likely due to the relatively high variability in change per annum resulting from the SRTM2 method in the NC(-) group. The SRTM2 method also resulted in the highest change-per-annum variability in the MCI(-) group. This is possibly due to bias in SRTM that

results from violation of its assumption of a 1-tissue compartment model that is not satisfied for PiB in CER and low-PiB-binding CER-like GBL data typical of the NC(-) group [25, 93]. Previous cross-sectional studies have shown SRTM and SRTM2 to be highly variable in low-PiB-binding subjects, relative to SUVR and Logan DVR measures [94, 115]. However, another study has shown SRTM2 DVR may more accurately represent actual changes in specific binding in high-PiB-binding subjects than changes resulting from SUVR methods because SRTM2 is less susceptible (than SUVR) to progressive changes in  $R_1$  [98]. As a result, change per annum measured by SRTM2 in the AD and MCI(+) groups (the two groups with the highest PiB binding and largest changes in  $R_1$ ) in this current study may better reflect changes in specific binding than the other analytic methods tested. However, in studies of low-PiB-binding subjects, accurately detecting small changes in specific binding when using SRTM2 may not be possible. As such, SRTM2 may not be ideal for early detection of amyloid deposition or in natural history studies.

The reference Logan method resulted in the lowest variability measures in change per annum across all diagnostic and PiB-status groups. This is consistent with a previous cross-sectional study that found the reference Logan DVR to exhibit lowest test-retest variability across control, MCI, and AD subjects when compared to SUVR and SRTM methods [94]. The authors of this previous study speculated that because of its low cross-sectional variability, Logan DVR with cerebellar reference may be the ideal method for detecting small interval changes in natural history and treatment studies. However, in the current longitudinal study, the Logan DVR method resulted in lower change per annum measures than those of any SUVR

method across all high-PiB-binding (AD, MCI(+), NC(+)) and converting (NC(-/+)) groups, and comparable change per annum measures to SUVR methods in the NC(-) group. The relatively small range of intergroup change per annum resulting from the Logan DVR method could potentially obscure differing rates of change between subjects with increasing PiB retention and subjects with stable or decreasing PiB retention over time. Indeed, in the current study, mean change per annum measured by Logan DVR was not significantly different between the MCI(+) and NC(-) groups. This suggests the Logan DVR method might not be ideal in a treatment trial, where change in radiotracer retention in a treatment group is compared to that in a control group.

The use of the SUVR90 method resulted in larger change-per-annum measures than any other analytic method in the AD group. The SUVR90 method also resulted in the largest variability in change per annum in the AD group. These relatively large change and variability measures likely are a result of the changes in  $R_1$  observed in the AD group. van Berckel et al (2013) demonstrated that change in SUVR90 is more influenced by changes in  $R_1$  than SUVR measures at earlier time frames, and a reduction in  $R_1$  between serial examinations, as seen in these AD subjects, may explain the relatively large change per annum measures resulting from the use of SUVR90. As such, the SUVR90 measure may result in apparent increases in PiB binding in AD subjects that are not reflective of progressive brain amyloidosis, but rather attributable to increases in the relative changes in blood flow between serial examinations. A result of relatively large change-per-annum measures in the AD population is that the relationship between SUVR90 change-per-



annum and average outcome measures was best fit by a linear function across the study population. This implies that amyloid deposition would continue to increase in late-AD subjects, which is counter to previous studies that have shown amyloid PET reaches a plateau as cognitive decline worsens [58-60].

Change measures resulting from the SUVR60 and SUVR70 methods share similar characteristics. In this population, neither method measures mean change per annum measures that are significantly greater than those resulting from the SRTM2 method in AD subjects, and both methods result in significantly greater mean change-per-annum measures in the MCI(+) group relative to the NC(-) group. However, the SUVR60 method results in lower change-per-annum variability, measured by standard deviation, than the SUVR70 method across all diagnostic and PiB-status groups. This may be due to superior counting statistics (less radioactive decay) during the SUVR60 time frame relative to later SUVR time frames and therefore measuring data with a higher signal-to-noise ratio [96].

The SUVR60 method also results in change-per-annum measures closer to SRTM2 DVR in high-PiB-binding subjects. Indeed, the SUVR70 method yielded a mean change per annum measure in the MCI(+) group that is statistically greater than SRTM2, whereas SUVR60 does not. This may be due to SUVR70's slightly increased vulnerability to changes in regional and global perfusion relative to SUVR60 [98], and is consistent with a previous cross-sectional study, which found that SUVR60 has smaller bias than SUVR70 when compared to Logan DVR with arterial input [96].

Each of the different analytic methods tested in this study has different strengths and weaknesses in measuring longitudinal changes. The SRTM2 method may be less susceptible to changes in perfusion than SUVR methods and therefore may more accurately represent actual changes in specific binding in high-PiB-binding subjects [98], but it also yields highly variable change per annum measures in low-PiB-binding subjects. The Logan DVR method yields change per annum measures with low variability across all groups but also yields a relatively small range of intergroup change per annum. All SUVR time frames are susceptible to changes in global and regional perfusion, but, consistent with van Berckel et al. (2013), SUVR60 seems to be the least susceptible relative to SUVR70 and SUVR90. The SUVR60 method yields change-per-annum measures comparable to those produced by SRTM2 DVR in high-PiB-binding subjects with decreasing  $R_1$  values. It also results in smaller change-per-annum variability than SRTM2 DVR in the NC(-) group, and yields statistically different change per annum means between MCI(+) and NC(-) groups. Of the five methods compared, SUVR60 represents the optimal analytic method for accurately measuring change per annum across all diagnostic and PiB-status groups when using cerebellar GM as a reference. It is, however, important to note that all methods detected significant change in the NC(-/+) group, suggesting that all methods can detect substantial change.

#### **4.4.2 Consideration of Reference Region**

Cerebellar GM has traditionally been used as the PiB reference region because similar levels of PiB retention were measured in the cerebellum of NC and

AD subjects in early proof-of-concept PiB PET studies, and cerebellar GM is known to have no or low levels of fibrillar amyloid [93]. In this work, the effect of other reference regions on longitudinal changes in PiB studies is not evaluated. However, findings suggest that cerebellar GM may not be an ideal reference for tracking longitudinal changes in PiB. Prior to smoothing the time-activity curves, differences in outcome measures were driven by noise in the CER time-activity curves rather than methodological characteristics. The interquartile ranges of change over time in AD subjects (those subjects with the greatest PiB retention and therefore least susceptible to noise) ranged from 0.095 for Logan DVR to 0.203 for SUVR90 (**Figure 39A**). After smoothing, the interquartile ranges were 0.086 for Logan DVR and 0.097 for SRTM2 DVR (**Figure 39B**), demonstrating a reduction in variability up to 61%. In longitudinal studies or treatment trials, where the detection of small changes is necessary, if time-activity curve smoothing is not performed, noise within the reference region at baseline and follow-up scans may obscure actual changes in specific binding, regardless of the analytic method.

This study also found that longitudinal changes in non-specific binding in SWM may drive the changes detected in cortical GM in NC(-), MCI(-), and MCI(+) subjects when using the SUVR method. This is likely due to the PVE of high-signal WM spill-over into relatively low-signal neocortical space. As a result, a low-PiB-binding subject could appear to be changing over time when no amyloid deposition has occurred due to changes in non-specific uptake in white matter.

A reference region that incorporates WM, with increased and more stable PiB non-specific uptake than cerebellar GM, may yield change measures less influenced

by noise in the reference region. The use of a WM reference region may also reduce the influence of changes in non-specific uptake in WM on measured cortical SUVR change measures and better represent actual changes in PiB specific binding. Indeed, several recent ADNI-based  $^{18}\text{F}$ -florbetapir studies have demonstrated that the use of a WM reference region in SUVR yields more stable longitudinal change measures [116-118].

However, more work needs to be done in evaluating the feasibility of different reference regions for different analytic methods used with PiB. Cerebral blood flow in WM is 2.0-2.4 times slower than cerebral blood flow in the neocortex [119]. Using WM as a reference in SRTM violates the method's key assumption that reference and target tissues have the same non-displaceable volume of distribution, which could lead to highly biased DVR values [25]. The same is true for the SUVR method. Increasingly different rates of clearance between the WM-reference and target tissues during an assumed transient equilibrium period could lead to highly biased SUVR values.

An alternative to using a WM reference region may be the application of a PVC technique that accounts for WM signal spill-over into neocortical regions. Application of the MMG- or RBV-correction technique [9, 11] would not alleviate the influence of noise in the reference region on measured longitudinal changes, but it may reduce the influence of changes in non-specific WM signal on longitudinal changes detected in cortical GM in  $\text{A}\beta$ -binding radioligand studies.

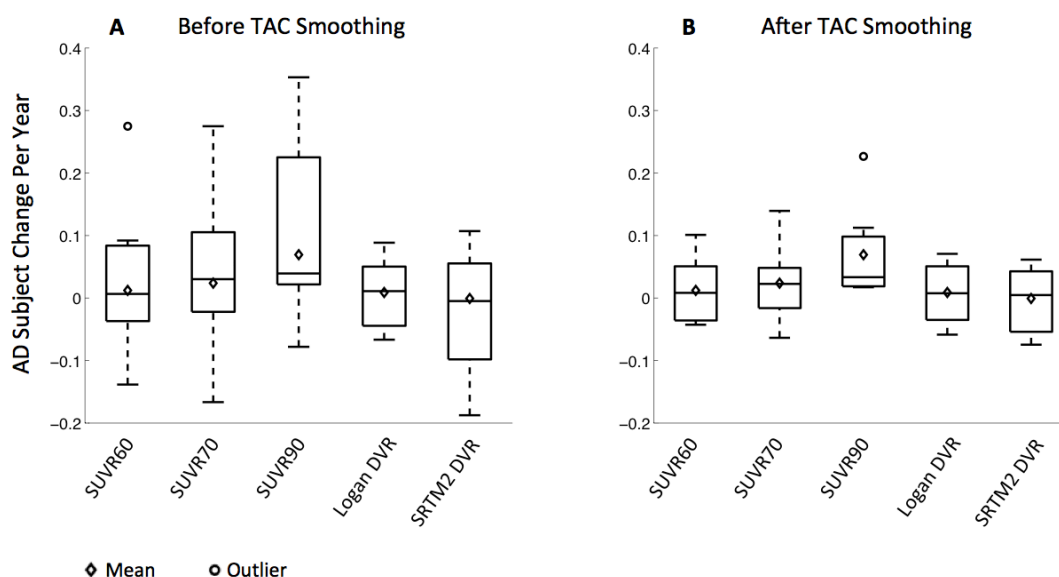


**Figure 39 Box-and-whisker plots of change per year of AD subjects across all outcome measures based on raw time-activity curves and smoothed time-activity curves.** Data based on raw time-activity curves are presented in (A) and data based on smoothed time-activity curves are presented in (B). The interquartile ranges (IQR) of SUVR60, SUVR70, SUVR90, Logan DVR, and SRTM2 DVR before time-activity curve smoothing are 0.121, 0.127, 0.203, 0.095, and 0.154, respectively. After smoothing they are 0.087, 0.064, 0.080, 0.086, and 0.097, respectively, representing decreases in variability of 28% for SUVR60, 49% for SUVR70, 61% for SUVR90, 9% for Logan DVR, and 37% for SRTM2 DVR.

#### 4.4.3 Study Limitations

One obvious limitation of this study is sample size, with the MCI(-) and NC(-/+) groups only consisting of 4 and 5 subjects, respectively. These sample sizes lack the statistical power to test hypotheses with parametric tests or within the ANOVA framework, and increase the effect of outliers. For example, the removal of one outlying non-accumulator from the MCI(+) group (apparent in **Figure 36**) increases the average change per annum in the MCI(+) group beyond that measured in the NC(-/+) group:  $0.104 \pm 0.076$  SUVR60,  $0.122 \pm 0.101$  SUVR70,  $0.144 \pm 0.150$  SUVR90,  $0.054 \pm 0.047$  Logan DVR, and  $0.069 \pm 0.090$  SRTM2 DVR.

Another limitation is the lack of ground truth. The 2-tissue, 4-parameter arterial input model and Logan with arterial input methods have been used as benchmarks in studies of PiB PET quantification, as the 2-tissue, 4-parameter method describes 90-min PiB data well, and the two methods strongly agree [93-96]. However, longitudinal arterial data is not available or practical for most subjects in this study. As such, relative performance of the simplified reference tissue methods was evaluated.

#### 4.4.4 Conclusion

If using cerebellar grey matter as reference, SUVR60 appears to be an optimal method for tracking longitudinal changes across diagnostic groups and PiB-statuses. However, cerebellar grey matter may not be an ideal reference region for longitudinal studies due to its poor signal-to-noise ratio. Reference regions that incorporate subcortical white matter and partial volume correction techniques that

address non-specific binding in subcortical white should continue to be explored to improve detection of changes in specific binding in PiB studies.

# Chapter 5

## Summary and Conclusions

The overall aim of this work was to identify optimal methodological techniques for quantifying PiB PET in both cross-sectional and longitudinal studies. The first component of this thesis work (Chapter 2) involved generating simulated PiB PET phantoms based on existing MR and PiB PET images to characterize and validate the implementation of three partial volume correction techniques: the Meltzer, the Müller-Gärtner, and the Region-Based Voxel-Wise methods. The second part of this thesis work (Chapter 3) examined the effect of these three partial volume correction techniques on correlations between region-matched antemortem PiB PET SUVR and postmortem measures of amyloid load in a unique cohort of 12 subjects. Characterizing the relationships between antemortem and postmortem measures of amyloid load is an ongoing area of investigation, and will improve understanding of the natural history of Alzheimer's disease and aid in the validation of preventative measures for the disease. Noise magnification properties for each of the partial volume correction techniques were also characterized using both brain tissue and ventricular CSF PiB PET SUVR data. Results indicated that the impact of partial volume correction is highly specific to region placement and subject anatomy. The Region-Based Voxel-Wise method outperformed both the Müller-Gärtner and Meltzer PVC methods in noise magnification and correlations with postmortem measures of amyloid load. However, no PVC method improved antemortem-to-postmortem correlations relative to uncorrected PiB PET SUVR



data. This was likely due to the noise propagation properties of each of the techniques.

Perhaps the most interesting finding in this study was the plateauing of PiB SUVR relative to postmortem measures of amyloid load. It was concluded that this plateauing was not a result of partial volume effects in the antemortem PiB PET data. Future directions for this component of the thesis work include continued investigation of this plateauing phenomenon. More antemortem and postmortem data should be collected, particularly in high-PiB-binding AD subjects, and other analytic methods should be applied to antemortem PiB PET data to determine if the plateauing is a result of the SUVR method. Alternative postmortem measures of amyloid load should also be explored.

The third component of this thesis work (Chapter 4) examined the relative performance of five simplified reference tissue methods in measuring baseline-to-follow-up change across multiple diagnostic groups. The SUVR60 method was found to be optimal in tracking longitudinal changes across all diagnostic groups. The SRTM2 method produced highly variable change measures in low-PiB-binding groups. The reference Logan method resulted in change measures that were not statistically different between the most stable and the fastest changing group. The SUVR90 method overestimated change in the AD group relative to all other measures. While the SUVR60 and SUVR70 methods resulted in relatively similar change measures, SUVR60 proved more stable in measuring change. However, a weakness of this study was the lack of ground truth. Future work should include examining the longitudinal performance of these methods against an unbiased

measure, such as arterial Logan. Simulated arterial and target tissue time-activity curves can be generated to actually quantify the bias of these reference tissue methods in measuring changes in PiB PET retention.

Results from this study also indicate that partial volume effects from non-specific binding in white matter may influence measured changes of amyloid load. While partial volume correction techniques did not improve the correlation between PiB PET and postmortem measures of amyloid load, the impact of the Region-Based Voxel-Wise method on longitudinal change measures should be explored.

## References

1. Normandin, M., R. Koeppe, and E. Morris, *Selection of weighting factors for quantification of PET radioligand binding using simplified reference tissue models with noisy input functions*. Physics in medicine and biology, 2012. **57**(3): p. 609.
2. Hoffman, E.J. and M.E. Phelps, *Positron emission tomography: principles and quantitation*. Positron emission tomography and autoradiography, 1986: p. 237-286.
3. Saha, G.B., *Performance Characteristics of PET Scanners*, in *Basics of PET Imaging*. 2010, Springer. p. 97-116.
4. Hoffman, E.J., S.-C. Huang, and M.E. Phelps, *Quantitation in positron emission computed tomography: 1. Effect of object size*. Journal of computer assisted tomography, 1979. **3**(3): p. 299-308.
5. Mazziotta, J.C., et al., *Quantitation in positron emission computed tomography: 5. Physical-anatomical effects*. Journal of computer assisted tomography, 1981. **5**(5): p. 734-743.
6. Meltzer, C.C., et al., *Correction of PET data for partial volume effects in human cerebral cortex by MR imaging*. Journal of computer assisted tomography, 1990. **14**(4): p. 561-570.
7. Meltzer, C.C., et al., *Comparative evaluation of MR-based partial-volume correction schemes for PET*. Journal of Nuclear Medicine, 1999. **40**(12): p. 2053-2065.
8. Muller-Gartner, H.W., et al., *Measurement of radiotracer concentration in brain gray matter using positron emission tomography: MRI-based correction for partial volume effects*. J Cereb Blood Flow Metab, 1992. **12**(4): p. 571-83.
9. Rousset, O.G., Y. Ma, and A.C. Evans, *Correction for partial volume effects in PET: principle and validation*. Journal of Nuclear Medicine, 1998. **39**(5): p. 904-911.
10. Rousset, O., et al., *Pixel-versus region-based partial volume correction in PET*. Quantitative Functional Imaging with Positron Emission Tomography., edited by RE Carson, Daube-Witherspoon, ME, Herscovitch, P Academic Press, San Diego, 1998: p. 67-75.
11. Thomas, B.A., et al., *The importance of appropriate partial volume correction for PET quantification in Alzheimer's disease*. European journal of nuclear medicine and molecular imaging, 2011. **38**(6): p. 1104-1119.
12. Yang, J., et al., *Investigation of partial volume correction methods for brain FDG PET studies*. Nuclear Science, IEEE Transactions on, 1996. **43**(6): p. 3322-3327.
13. Innis, R.B., et al., *Consensus nomenclature for in vivo imaging of reversibly binding radioligands*. Journal of Cerebral Blood Flow & Metabolism, 2007. **27**(9): p. 1533-1539.

14. Ballabh, P., A. Braun, and M. Nedergaard, *The blood–brain barrier: an overview: structure, regulation, and clinical implications*. Neurobiology of disease, 2004. **16**(1): p. 1-13.
15. Abbott, N.J., L. Rönnbäck, and E. Hansson, *Astrocyte–endothelial interactions at the blood–brain barrier*. Nature Reviews Neuroscience, 2006. **7**(1): p. 41-53.
16. Upadhyay, R.K., *Drug delivery systems, CNS protection, and the blood brain barrier*. BioMed research international, 2014. **2014**.
17. Mintun, M.A., et al., *A quantitative model for the in vivo assessment of drug binding sites with positron emission tomography*. Annals of neurology, 1984. **15**(3): p. 217-227.
18. Gunn, R.N., et al., *Quantitative imaging of protein targets in the human brain with PET*. Physics in Medicine and Biology, 2015. **60**(22): p. R363.
19. Levenberg, K., *A method for the solution of certain non–linear problems in least squares*. 1944.
20. Marquardt, D.W., *An algorithm for least-squares estimation of nonlinear parameters*. Journal of the Society for Industrial & Applied Mathematics, 1963. **11**(2): p. 431-441.
21. Koeppe, R., et al., *Compartmental analysis of [11C] flumazenil kinetics for the estimation of ligand transport rate and receptor distribution using positron emission tomography*. Journal of Cerebral Blood Flow & Metabolism, 1991. **11**(5): p. 735-744.
22. Lassen, N.A., *Neuroreceptor quantitation in vivo by the steady-state principle using constant infusion or bolus injection of radioactive tracers*. Journal of Cerebral Blood Flow & Metabolism, 1992. **12**(5): p. 709-716.
23. Lammertsma, A.A. and S.P. Hume, *Simplified Reference Tissue Model for PET Receptor Studies*. NeuroImage, 1996. **4**(3): p. 153-158.
24. Lammertsma, A., et al., *Comparison of methods for analysis of clinical [11C] raclopride studies*. Journal of Cerebral Blood Flow & Metabolism, 1996. **16**(1): p. 42-52.
25. Salinas, C.A., G.E. Searle, and R.N. Gunn, *The simplified reference tissue model: model assumption violations and their impact on binding potential*. J Cereb Blood Flow Metab, 2015. **35**(2): p. 304-11.
26. Wu, Y. and R.E. Carson, *Noise reduction in the simplified reference tissue model for neuroreceptor functional imaging*. J Cereb Blood Flow Metab, 2002. **22**(12): p. 1440-52.
27. Logan, J., et al., *Graphical analysis of reversible radioligand binding from time-activity measurements applied to [N-11C-methyl]-(-)-cocaine PET studies in human subjects*. J Cereb Blood Flow Metab, 1990. **10**(5): p. 740-747.
28. Logan, J., et al., *Distribution Volume Ratios Without Blood Sampling from Graphical Analysis of PET Data*. J Cereb Blood Flow Metab, 1996. **16**(5): p. 834-840.
29. Logan, J., *Graphical analysis of PET data applied to reversible and irreversible tracers*. Nuclear medicine and biology, 2000. **27**(7): p. 661-670.

30. Adler, L.P., et al., *Noninvasive grading of musculoskeletal tumors using PET*. Journal of nuclear medicine: official publication, Society of Nuclear Medicine, 1991. **32**(8): p. 1508-1512.
31. Carson, R.E., et al., *Comparison of bolus and infusion methods for receptor quantitation—Application to [F-18] cyclofoxy and positron emission tomography*. J Cereb Blood Flow Metab, 1993. **13**(1).
32. Farde, L., et al., *Kinetic Analysis of Central [11C] Raclopride Binding to D2-Dopamine Receptors Studied by PET—A Comparison to the Equilibrium Analysis*. Journal of Cerebral Blood Flow & Metabolism, 1989. **9**(5): p. 696-708.
33. Slifstein, M., *Revisiting an Old Issue: The Discrepancy Between Tissue Ratio-Derived Binding Parameters and Kinetic Modeling-Derived Parameters After a Bolus of the Serotonin Transporter Radioligand 123I-ADAM*. Journal of Nuclear Medicine, 2008. **49**(2): p. 176-178.
34. Förstl, H. and A. Kurz, *Clinical features of Alzheimer's disease*. European archives of psychiatry and clinical neuroscience, 1999. **249**(6): p. 288-290.
35. Mirra, S.S., et al., *The Consortium to Establish a Registry for Alzheimer's Disease (CERAD) Part II. Standardization of the neuropathologic assessment of Alzheimer's disease*. Neurology, 1991. **41**(4): p. 479-479.
36. Iwatsubo, T., et al., *Visualization of A $\beta$ 42 (43) and A $\beta$ 40 in senile plaques with end-specific A $\beta$  monoclonals: evidence that an initially deposited species is A $\beta$ 42 (43)*. Neuron, 1994. **13**(1): p. 45-53.
37. Goedert, M., *Tau protein and the neurofibrillary pathology of Alzheimer's disease*. Trends in neurosciences, 1993. **16**(11): p. 460-465.
38. Thal, D.R., et al., *Phases of A $\beta$ -deposition in the human brain and its relevance for the development of AD*. Neurology, 2002. **58**(12): p. 1791-1800.
39. Braak, H. and E. Braak, *Neuropathological stageing of Alzheimer-related changes*. Acta Neuropathol, 1991. **82**(4): p. 239-259.
40. Arnold, S.E., et al., *The topographical and neuroanatomical distribution of neurofibrillary tangles and neuritic plaques in the cerebral cortex of patients with Alzheimer's disease*. Cerebral Cortex, 1991. **1**(1): p. 103-116.
41. Price, J.L. and J.C. Morris, *Tangles and plaques in nondemented aging and "preclinical" Alzheimer's disease*. Annals of neurology, 1999. **45**(3): p. 358-368.
42. Joachim, C.L., H. Mori, and D.J. Selkoe, *Amyloid  $\beta$ -protein deposition in tissues other than brain in Alzheimer's disease*. 1989.
43. Jack Jr, C.R., et al., *Hypothetical model of dynamic biomarkers of the Alzheimer's pathological cascade*. Lancet neurology, 2010. **9**(1): p. 119.
44. Jack Jr, C.R., et al., *Tracking pathophysiological processes in Alzheimer's disease: an updated hypothetical model of dynamic biomarkers*. The Lancet Neurology, 2013. **12**(2): p. 207-216.
45. Morris, J.C. and J.L. Price, *Pathologic correlates of nondemented aging, mild cognitive impairment, and early-stage Alzheimer's disease*. J Mol Neurosci, 2001. **17**(2): p. 101-18.
46. Morris, J.C., et al., *Mild cognitive impairment represents early-stage Alzheimer disease*. Archives of neurology, 2001. **58**(3): p. 397-405.

47. Petersen, R.C., et al., *Practice parameter: early detection of dementia: mild cognitive impairment (an evidence-based review). Report of the Quality Standards Subcommittee of the American Academy of Neurology*. Neurology, 2001. **56**(9): p. 1133-42.
48. Larrieu, S., et al., *Incidence and outcome of mild cognitive impairment in a population-based prospective cohort*. Neurology, 2002. **59**(10): p. 1594-1599.
49. Yesavage, J.A., et al., *Modeling the prevalence and incidence of Alzheimer's disease and mild cognitive impairment*. Journal of psychiatric research, 2002. **36**(5): p. 281-286.
50. Ganguli, M., et al., *Mild cognitive impairment, amnestic type An epidemiologic study*. Neurology, 2004. **63**(1): p. 115-121.
51. Engler, H., et al., *First human study with a benzothiazole amyloid-imaging agent in Alzheimer's disease and control subjects*. Neurobiol Aging, 2002. **23**(suppl 1): p. S429.
52. Klunk, W.E., et al., *Imaging brain amyloid in Alzheimer's disease with Pittsburgh Compound - B*. Annals of neurology, 2004. **55**(3): p. 306-319.
53. Wong, D.F., et al., *In vivo imaging of amyloid deposition in Alzheimer disease using the radioligand 18F-AV-45 (flobetapir F 18)*. Journal of Nuclear Medicine, 2010. **51**(6): p. 913-920.
54. Vandenberghe, R., et al., *18F - flutemetamol amyloid imaging in Alzheimer disease and mild cognitive impairment: A phase 2 trial*. Annals of neurology, 2010. **68**(3): p. 319-329.
55. Sabri, O., et al., *Florbetaben PET imaging to detect amyloid beta plaques in Alzheimer disease: Phase 3 study*. Alzheimer's & Dementia, 2015.
56. Cselényi, Z., et al., *Clinical validation of 18F-AZD4694, an amyloid- $\beta$ -specific PET radioligand*. Journal of Nuclear Medicine, 2012. **53**(3): p. 415-424.
57. Förster, S., et al., *Regional expansion of hypometabolism in Alzheimer's disease follows amyloid deposition with temporal delay*. Biological psychiatry, 2012. **71**(9): p. 792-797.
58. Jack Jr, C.R., et al., *Shapes of the trajectories of 5 major biomarkers of Alzheimer disease*. Archives of neurology, 2012: p. archneurol. 2011.3405 v1.
59. Jack, C.R., Jr., et al., *Brain beta-amyloid load approaches a plateau*. Neurology, 2013. **80**(10): p. 890-6.
60. Villemagne, V.L., et al., *Amyloid  $\beta$  deposition, neurodegeneration, and cognitive decline in sporadic Alzheimer's disease: a prospective cohort study*. The Lancet Neurology, 2013. **12**(4): p. 357-367.
61. Chételat, G., et al., *Amyloid imaging in cognitively normal individuals, at-risk populations and preclinical Alzheimer's disease*. NeuroImage: Clinical, 2013. **2**: p. 356-365.
62. Johnson, K.A., et al., *Appropriate use criteria for amyloid PET: A report of the Amyloid Imaging Task Force, the Society of Nuclear Medicine and Molecular Imaging, and the Alzheimer's Association*. Journal of Nuclear Medicine, 2013. **54**(3): p. 476-490.

63. Johnson, K.A., et al., *Update on appropriate use criteria for amyloid PET imaging: dementia experts, mild cognitive impairment, and education*. Journal of Nuclear Medicine, 2013. **54**(7): p. 1011-1013.
64. Witte, M.M., et al., *Clinical use of amyloid-positron emission tomography neuroimaging: Practical and bioethical considerations*. Alzheimer's & Dementia: Diagnosis, Assessment & Disease Monitoring, 2015. **1**(3): p. 358-367.
65. Ikonomic, M.D., et al., *Early AD pathology in a [C-11] PiB-negative case: a PiB-amyloid imaging, biochemical, and immunohistochemical study*. Acta Neuropathol, 2012: p. 1-15.
66. Driscoll, I., et al., *Correspondence between in vivo (11)C-PiB-PET amyloid imaging and postmortem, region-matched assessment of plaques*. Acta Neuropathol, 2012. **124**(6): p. 823-31.
67. Fischl, B., et al., *Whole brain segmentation: automated labeling of neuroanatomical structures in the human brain*. Neuron, 2002. **33**(3): p. 341-355.
68. Fischl, B., et al., *Automatically parcellating the human cerebral cortex*. Cerebral Cortex, 2004. **14**(1): p. 11-22.
69. Ségonne, F., et al., *A hybrid approach to the skull stripping problem in MRI*. Neuroimage, 2004. **22**(3): p. 1060-1075.
70. Dale, A.M., B. Fischl, and M.I. Sereno, *Cortical surface-based analysis: I. Segmentation and surface reconstruction*. Neuroimage, 1999. **9**(2): p. 179-194.
71. Fischl, B., M.I. Sereno, and A.M. Dale, *Cortical surface-based analysis: II: inflation, flattening, and a surface-based coordinate system*. Neuroimage, 1999. **9**(2): p. 195-207.
72. Fischl, B., et al., *High-resolution intersubject averaging and a coordinate system for the cortical surface*. Human brain mapping, 1999. **8**(4): p. 272-284.
73. Jenkinson, M., et al., *Fsl*. Neuroimage, 2012. **62**(2): p. 782-790.
74. Flannery, B.P., et al., *Numerical recipes in C*. Press Syndicate of the University of Cambridge, New York, 1992. **24**.
75. Studholme, C., D.L. Hill, and D.J. Hawkes, *An overlap invariant entropy measure of 3D medical image alignment*. Pattern recognition, 1999. **32**(1): p. 71-86.
76. Rousset, O.G., et al., *Design and implementation of an automated partial volume correction in PET: application to dopamine receptor quantification in the normal human striatum*. Journal of Nuclear Medicine, 2008. **49**(7): p. 1097-1106.
77. Mikhno, A., et al., *Voxel-based analysis of 11C-PIB scans for diagnosing Alzheimer's disease*. Journal of Nuclear Medicine, 2008. **49**(8): p. 1262-1269.
78. Drzezga, A., et al., *Imaging of amyloid plaques and cerebral glucose metabolism in semantic dementia and Alzheimer's disease*. Neuroimage, 2008. **39**(2): p. 619.
79. Rabinovici, G.D., et al., *Increased metabolic vulnerability in early-onset Alzheimer's disease is not related to amyloid burden*. Brain, 2010. **133**(2): p. 512-528.

80. Bacskai, B.J., et al., *Molecular imaging with Pittsburgh Compound B confirmed at autopsy: a case report*. Archives of neurology, 2007. **64**(3): p. 431.
81. Ikonomic, M.D., et al., *Post-mortem correlates of in vivo PiB-PET amyloid imaging in a typical case of Alzheimer's disease*. Brain, 2008. **131**(6): p. 1630-1645.
82. Cairns, N.J., et al., *Absence of Pittsburgh Compound B Detection of Cerebral Amyloid {beta} in a Patient With Clinical, Cognitive, and Cerebrospinal Fluid Markers of Alzheimer Disease: A Case Report*. Archives of neurology, 2009. **66**(12): p. 1557.
83. Villemagne, V.L., et al., *11C-PiB PET studies in typical sporadic Creutzfeldt-Jakob disease*. Journal of Neurology, Neurosurgery & Psychiatry, 2009. **80**(9): p. 998-1001.
84. Burack, M.A., et al., *In vivo amyloid imaging in autopsy-confirmed Parkinson disease with dementia*. Neurology, 2010. **74**(1): p. 77-84.
85. Kadir, A., et al., *Positron emission tomography imaging and clinical progression in relation to molecular pathology in the first Pittsburgh Compound B positron emission tomography patient with Alzheimer's disease*. Brain, 2011. **134**(1): p. 301-317.
86. Sojkova, J., et al., *In Vivo Fibrillar beta-Amyloid Detected Using C-11 PiB Positron Emission Tomography and Neuropathologic Assessment in Older Adults*. Archives of Neurology, 2011. **68**(2): p. 232-240.
87. Kantarci, K., et al., *< i> Ante mortem</i> amyloid imaging and  $\beta$ -amyloid pathology in a case with dementia with Lewy bodies*. Neurobiology of Aging, 2012. **33**(5): p. 878-885.
88. Mathis, C.A., et al., *Synthesis and evaluation of 11C-labeled 6-substituted 2-arylbenzothiazoles as amyloid imaging agents*. Journal of medicinal chemistry, 2003. **46**(13): p. 2740-2754.
89. Nau, R., F. Sörgel, and H. Eiffert, *Penetration of drugs through the blood-cerebrospinal fluid/blood-brain barrier for treatment of central nervous system infections*. Clinical microbiology reviews, 2010. **23**(4): p. 858-883.
90. Su, Y., et al., *Partial volume correction in quantitative amyloid imaging*. NeuroImage, 2015. **107**(0): p. 55-64.
91. Price, J., et al. *Regional correspondance between [11C]PiB PET and post-mortem measures of amyloid load: consideration of partial volume averaging*. in *Human Amyloid Imaging*. 2013. Miami, FL.
92. Villemagne, V.L., et al., *Longitudinal assessment of A $\beta$  and cognition in aging and Alzheimer disease*. Annals of Neurology, 2011. **69**(1): p. 181-192.
93. Price, J.C., et al., *Kinetic modeling of amyloid binding in humans using PET imaging and Pittsburgh Compound-B*. Journal of Cerebral Blood Flow & Metabolism, 2005. **25**(11): p. 1528-1547.
94. Lopresti, B.J., et al., *Simplified quantification of Pittsburgh Compound B amyloid imaging PET studies: a comparative analysis*. J Nucl Med, 2005. **46**(12): p. 1959-72.
95. Yaquib, M., et al., *Simplified parametric methods for [11C]PIB studies*. NeuroImage, 2008. **42**(1): p. 76-86.



96. McNamee, R.L., et al., *Consideration of optimal time window for Pittsburgh compound B PET summed uptake measurements*. Journal of Nuclear Medicine, 2009. **50**(3): p. 348-355.
97. Tolboom, N., et al., *Test-retest variability of quantitative [11C] PIB studies in Alzheimer's disease*. European journal of nuclear medicine and molecular imaging, 2009. **36**(10): p. 1629-1638.
98. van Berckel, B.N., et al., *Longitudinal amyloid imaging using 11C-PiB: methodologic considerations*. J Nucl Med, 2013. **54**(9): p. 1570-6.
99. Schmidt, M.E., et al., *The influence of biological and technical factors on quantitative analysis of amyloid PET: Points to consider and recommendations for controlling variability in longitudinal data*. Alzheimer's & Dementia, 2015. **11**(9): p. 1050-1068.
100. Jagust, W.J., et al., *The Alzheimer's Disease Neuroimaging Initiative positron emission tomography core*. Alzheimer's & Dementia, 2010. **6**(3): p. 221-229.
101. Jagust, W.J., et al., *The Alzheimer's Disease Neuroimaging Initiative 2 PET Core: 2015*. Alzheimer's & Dementia, 2015. **11**(7): p. 757-771.
102. Rinne, J.O., et al., *11 C-PiB PET assessment of change in fibrillar amyloid- $\beta$  load in patients with Alzheimer's disease treated with bapineuzumab: a phase 2, double-blind, placebo-controlled, ascending-dose study*. The Lancet Neurology, 2010. **9**(4): p. 363-372.
103. Salloway, S., et al., *Two phase 3 trials of bapineuzumab in mild-to-moderate Alzheimer's disease*. New England Journal of Medicine, 2014. **370**(4): p. 322-333.
104. Klunk, W.E., et al., *The Centiloid Project: Standardizing quantitative amyloid plaque estimation by PET*. Alzheimer's & Dementia, 2015. **11**(1): p. 1-15. e4.
105. Aizenstein, H.J., et al., *Frequent Amyloid Deposition Without Significant Cognitive Impairment Among the Elderly*. Archives of Neurology, 2008. **65**(11): p. 1509-1517.
106. Minoshima, S., et al., *An automated method for rotational correction and centering of three-dimensional functional brain images*. J Nucl Med, 1992. **33**(8): p. 1579-1585.
107. Woods, R.P., J.C. Mazziotta, and S.R. Cherry, *MRI-PET registration with automated algorithm*. Journal of computer assisted tomography, 1993. **17**(4): p. 536-546.
108. Rosario, B.L., et al., *Inter-rater reliability of manual and automated region-of-interest delineation for PiB PET*. Neuroimage, 2011. **55**(3): p. 933-941.
109. Cleveland, W.S., *Robust locally weighted regression and smoothing scatterplots*. Journal of the American statistical association, 1979. **74**(368): p. 829-836.
110. Chen, Y.J., et al., *Relative 11C-PiB Delivery as a Proxy of Relative CBF: Quantitative Evaluation Using Single-Session 15O-Water and 11C-PiB PET*. Journal of Nuclear Medicine, 2015. **56**(8): p. 1199-1205.
111. Cohen, A.D., et al., *Classification of amyloid-positivity in controls: Comparison of visual read and quantitative approaches*. NeuroImage, 2013. **71**(0): p. 207-215.
112. Seber, G. and C. Wild, *Nonlinear regression*. 2003. Wiley, New York.

113. Akaike, H., *A new look at the statistical model identification*. Automatic Control, IEEE Transactions on, 1974. **19**(6): p. 716-723.
114. Burnham, K.P. and D.R. Anderson, *Model selection and multimodel inference: a practical information-theoretic approach*. 2002: Springer Science & Business Media.
115. Tolboom, N., et al., *Detection of Alzheimer pathology in vivo using both 11C-PiB and 18F-FDDNP PET*. J Nucl Med, 2009. **50**(2): p. 191-7.
116. Brendel, M., et al., *Improved longitudinal [18 F]-AV45 amyloid PET by white matter reference and VOI-based partial volume effect correction*. Neuroimage, 2015. **108**: p. 450-459.
117. Landau, S.M., et al., *Measurement of Longitudinal  $\beta$ -Amyloid Change with 18F-Florbetapir PET and Standardized Uptake Value Ratios*. Journal of Nuclear Medicine, 2015. **56**(4): p. 567-574.
118. Chen, K., et al., *Improved Power for Characterizing Longitudinal Amyloid- $\beta$  PET Changes and Evaluating Amyloid-Modifying Treatments with a Cerebral White Matter Reference Region*. Journal of Nuclear Medicine, 2015. **56**(4): p. 560-566.
119. Fodero-Tavoletti, M.T., et al., *Characterization of PiB binding to white matter in Alzheimer disease and other dementias*. Journal of Nuclear Medicine, 2009. **50**(2): p. 198-204.